RICE UNIVERSITY

Experimental Results and Three-Dimensional Simulations of Instabilities in a Rotating Lid-Driven Cylinder

by

Zhao Chad Kong

A THESIS SUBMITTED
IN PARTIAL FULFILLMENT OF THE
REQUIREMENTS FOR THE DEGREE

Masters of Science

APPROVED, THESIS COMMITTEE

Brent C. Houchens, Chair
Assistant Professor of Mechanical Engineering

Marcia K. O'Malley
Associate Professor of Mechanical Engineering

Mark P. Embree
Professor of Computational and Applied Mathematics

HOUSTON, TEXAS
August 2011

Abstract

Experimental Results and Three-Dimensional Simulations of Instabilities in a Rotating Lid-Driven Cylinder

by

Zhao Chad Kong

An experimental setup for a rotating lid-driven cylinder problem is designed and constructed in the context of modeling bulk semiconductor crystal growth techniques. Details concerning construction of the experimental setup are included in the interest of reproducibility. Ultrasonic Doppler Velocimetry (UDV) is tested as a viable visualization technique for the lid-driven cylinder and experimental measurements of the flow field are compared to numerical simulations. The aspect ratio of the cylinder and the Reynolds number are the governing parameters for the problem. Experimental and computation results are presented for aspect ratio of 2.5 and Reynolds numbers up to 3000. Accurate UDV measurements of the steady, axisymmetric base flow are demonstrated for both water and a 20% glycerin-water mixture as the working fluid. The expected periodic, axisymmetric instability at Reynolds number of 3000 was unobserved by the UDV. However, related instabilities were observed at lower Reynolds numbers. Associated strengths and weaknesses of UDV for flow measurement are discussed.

Acknowledgments

I am forever grateful to my research advisor and thesis committee chair Dr. Brent C. Houchens. Over the past few years he has been a professor, a mentor, and an invaluable friend to me. His knowledge and passion for science is tempered by a willingness to teach and untiring dedication to his students; the perfect combination of strength and flexibility. I could not have asked for a better advisor.

I am also grateful to Dr. Marcia K. O'Malley and Dr. Mark P. Embree for taking the time of out their busy schedules to serve on my thesis committee. Your advice and feedback is greatly appreciated.

This work was supported by the Air Force Office of Scientific Research (AFOSR) and would also not have been possible without the Oshman Engineering Design Kitchen. I would like to thank the School of Engineering for providing such a wonderful space for me to work and build my experimental setup. Special thanks go to Joseph Gesenhues for training me in the machine shop over the past few years.

Kenny Davis, Jacky Huang, and Andres Goza have been wonderful people to share an office with. Thank you for sharing your knowledge, advice, and lunch hours with me. I've always learned something new in our discussions together.

I would also like to express my most sincere gratitude all of the faculty and staff that make up the Department of Mechanical Engineering and Material Science. Under your guidance these past few years, I have grown both as a student and as an individual. Thank you for being so willing to share your knowledge and expertise

with me. I would not be the person I am today without your commitment to teaching.

I would also like to acknowledge several professors outside of my department. Dr. James Brown from the Economics Department, Dr. James McLurkin from the Computer Science Department, and Dr. Embree from the Computational and Applied Mathematics Department have greatly enriched my academic experience here at Rice.

I would like to thank Rachel Jackson, Edward Biegert, Nathan Martin, and Duncan Eddy for their assistance and companionship during the long hours of running experiments.

Finally, I want to thank my family and friends for supporting me throughout this process: my parents, Lixin Mao and Weize Kong, for always giving me the freedom and opportunity to pursue my goals in life; Diane Chen for feeding me and being tolerant of my work schedule; and all of my friends for being there when I needed them.

Contents

List of Figures

List of Tables

Chapter 1

Introduction and Motivation

The main goal of this thesis is to study the rotating lid-driven cylinder problem experimentally and to determine whether an Ultrasonic Doppler Velocimeter can be effectively used to visualize the flow dynamics of this problem. Although many experiments have already been performed on the rotating lid-driven cylinder problem, most visualization techniques require a transparent liquid medium. In an effort to investigate the flow dynamics for a rotating lid problem with opaque fluids such as liquid metals, the Ultrasonic Doppler Velocimeter is tested as a viable visualization tool. In addition to an experimental setup, test cases run on an existing open-source spectral element computational fluid dynamics code are also presented. This thesis is motivated by the need to measure flow fields in the melt of bulk semiconductor processing techniques, with an emphasis on the traveling heater and float-zone crystal growth methods for producing semiconducting ternary alloys with controlled composition and microstructure.

1.1. Motivation to Improve Crystal Growth Techniques

The long term motivation for this thesis stems from difficulties that experimentalists have experienced with certain crystal growth techniques and their use in growing large, single-crystals of alloyed semiconducting materials, where segregation of the constituents is an issue. These techniques include the traveling heater method, radiatively heated float-zone technique, and RF heated float-zone technique. The creation of single-crystal semiconductors is very important for the optoelectronics and sensing industries, and advances in these techniques have significant scientific and practical implications. The ability to grow single-crystal, ternary alloys of very specific compositions will result in semiconducting materials with tunable bandgaps that can be customized for a number of applications. However, challenges such as compositional segregation and flow control associated with the traveling heater and float-zone crystal growth techniques have prevented bulk production of high quality ternary alloy crystals. A breakthrough in these techniques can result in ultra high-speed electronics, efficient solar cells, and room temperature photoconductive radiation detectors becoming common place in industrial and commercial markets

In float-zone crystal growth techniques, a polycrystalline feed rod is drawn through a heater (either focused radiation or RF heating), where a small region of the material is melted and re-solidifies as a single crystal as it exits (Figure 1.1). The molten region of the material within the heater is suspended against the force of gravity by surface tension and does not require a container. This reduces both

the impurities introduced into the material and stresses experienced in the cooling process, resulting in a higher-quality crystal. This is qualitatively similar to the needle-eye float-zone technique. However, the needle-eye technique has a very different geometry, with electromagnetic body forces aiding to support the free surface, and thus is not discussed here.

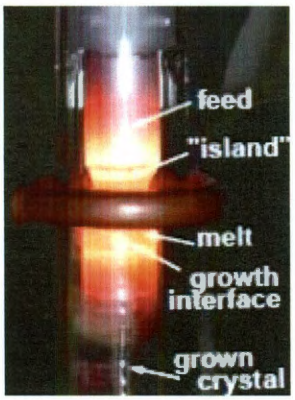

Figure 1.1 – Float-zone crystal growth by RF heating, photo reproduced from (Dold 2004)

For the float-zone techniques of interest, the melt region can be idealized as a cylinder of molten material bounded by two no-slip top and bottom boundaries and a free-surface on the "wall" of the cylinder (Figure 1.2). The top and bottom boundaries are isothermal at the solidification temperature of the material, and there is a heat-flux applied perpendicularly to the axis of the cylinder. In general, flow within the melt region is driven by thermocapillary forces resulting from temperature gradients on the free surface of the melt region. The flow is steady and axisymmetric for small temperature gradients. However, for large temperature gradients, the base flow becomes unstable and can transition to a time-dependent, three-dimensional flow (Chun and Wuest 1982).

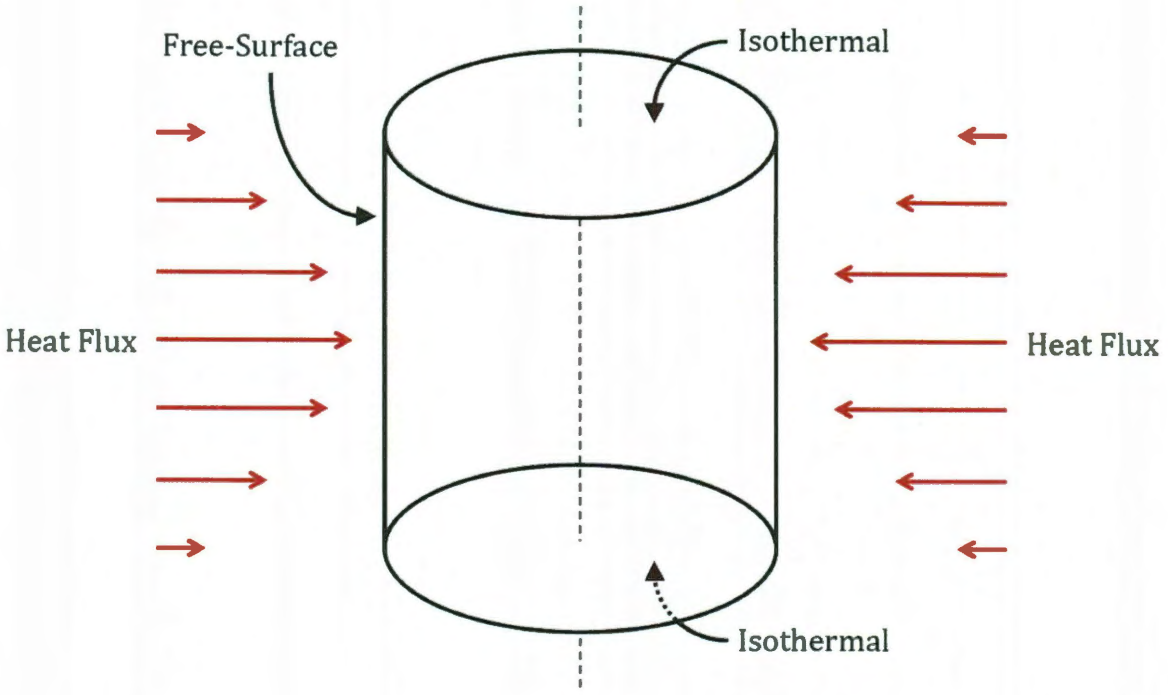

Figure 1.2 – Idealized model of melt region for float-zone technique

The traveling heater method (THM) is a related crystal growth technique with a very similar geometry. In the traveling heater method, a feed rod of polycrystalline material is encased in a cylindrical ampoule, often quartz. A heater that is generally much shorter than the length of the ampoule is then moved very slowly along the length of the charge. As this occurs, the region of the material contained within the heater is melted and re-solidified as it exits. The melt region within the ampoule can be idealized as in Figure 1.2, except the flow is now completely contained and there are no-slip boundaries on all surfaces. The traveling heater method combined with a melt solvent has been able to achieve polycrystalline ternary alloys with nearly uniform compositions even without external flow control (Houchens et al. 2010), but at very slow growth rates (1.2

mm/day). The key to rapid growth of single crystal ternary alloys via solvent based traveling heater methods is to impart external flow control of the melt region.

While a quiescent flow within the melt region is desirable for single constituent, compound forming or low-concentration doped crystal growth applications, the ideal flow for the solvent based traveling heater method for ternary alloy semiconductors is more complex. Since the composition of the crystal being solidified is different from that of the melt, the growth rate is limited by the amount of time required for the solute to diffuse from the melt front to the solidification front. A periodic, fully three-dimensional flow with a strong recirculation can mix the melt region and carry the solute to the solidification front, thus increasing the growth rate. However, it can also be the case that multiple types of periodic or time-dependant flows, activated at specific times or under specific conditions, are necessary to both increase growth rate and produce single-crystal ternary alloys. The challenge faced by experimentalists becomes two-fold. First external flow control techniques need to be characterized and refined so that one can controllably transition from one flow field to another by exciting or damping specific instabilities. Second, it is necessary to have both experimental and numerical models to determine the types of flows necessary to produce the desired properties in the final crystal.

In order to control the flow dynamics within the melt region as described above, experimentalists and modelers have tried a number of different techniques, such as rotating the feed/re-solidification rod or applying a traveling magnetic field

to induce electromagnetic body forces. However, despite advances in both computational and experimental techniques, the control of the flow dynamics within the melt zone still presents a significant problem to crystal growers. One of the main problems is the difficulty in actually determining the flow dynamics within the melt region. There are three complicating factors to determining in real-time the flow field within a melt region during the crystal growth process. The first is the small size of the melt region. The diameter of the melt region is usually only on the order of a few centimeters and the small size limits the types of visualization techniques that are feasible. Next, the melt region of interest is usually inside a heater that is operating at hundreds of degrees Celsius. Not only is the region of interest physically inaccessible since it is inside a heating element, but the extreme temperature further complicates any attempts to visual the flow with measurement devices. Lastly, the molten material for most practical crystals is optically opaque. This greatly limits the choices for visualization techniques, since most traditional techniques such as dye injection, photographic techniques, or laser based techniques require an optically transparent fluid.

Given the difficulties in real-time flow visualization of the melt region in these crystal growth processes, experimentalists can benefit greatly from a large scale experimental mock-up of the melt region. This experimental setup could then be used as a test bed for new techniques to control the flow within the melt region or to validate numerical models. The goal of this thesis is to demonstrate such a scaled experimental setup and investigate the use of Ultrasonic Doppler Velocimetry

for non-contact flow measurement of a fluid that is not required to be optically transparent.

There are two main challenges in creating the large scale experimental setup described above. The first is finding a visualization technique for fluid flows that will work for opaque, electrically conducting fluids. The Ultrasonic Doppler Velocimeter (UDV) presents itself as an ideal solution to this problem since it can obtain measurements in optically opaque fluids and has already been successfully used with liquid gallium, which has a melting point of 30°C (Brito et al. 2001). The second challenge is creating an experimental setup large enough to enable the use of visualization techniques such as the UDV. This thesis focuses on developing a mock-up of the traveling heater method, which has boundary conditions that are easy to reproduce in a large scale model. The rotating lid-driven cylinder configuration is used as an idealized model of the melt region for crystal growth experiments. Results from the analysis are directly applicable to traveling heater methods and the velocimetry techniques are applicable to float-zone and other bulk crystal growth methods.

This thesis documents the creation of an experimental setup for the rotating lid-driven cylinder problem and determines whether the UDV can be used to successfully determine the flow dynamics. The rotating lid-driven cylinder is used as a model of the melt region for the traveling heater crystal growth method. In the remainder of the chapter, background information on the rotating lid-driven cylinder problem and the Ultrasonic Doppler Velocimeter is presented.

1.2. Rotating Lid-Driven Cylinder Problem

The fundamental fluid flow within a closed cylindrical container with a rotating lid was first investigated by (Vogel 1968). A sketch of the problem is shown in Figure 1.3 below.

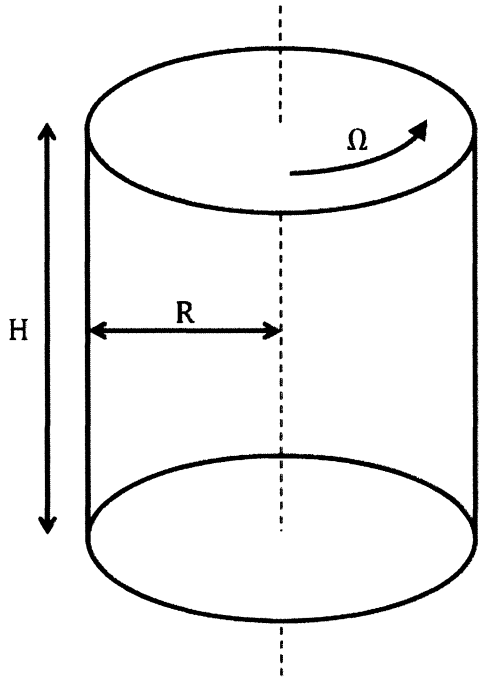

Figure 1.3 – Sketch of rotating lid-driven cylinder problem.

A viscous, incompressible fluid completely fills a closed cylinder with radius R and height H. There are no-slip boundaries on all surfaces of the cylinder. The sidewalls and bottom of the cylinder are stationary but the top of the cylinder rotates at a constant angular velocity Ω and provides the driving force for the flow. The flow is governed by two parameters: the aspect ratio, γ, and the Reynolds number, Re, as defined in (1.1) and (1.2), where ν is the kinematic viscosity of the fluid.

$$\gamma = \frac{H}{R} \tag{1.1}$$

$$Re = \frac{\Omega R^2}{\nu} \tag{1.2}$$

This problem is similar to Von Kármán's swirling flow (Kármán 1921) over an infinite disk, in the sense that a viscous pump is formed. As the top of the cylinder rotates, fluid particles near the disk begin to swirl due to viscous effects and are accelerated centrifugally and thrown outward toward the walls of the cylinder. Then, due to incompressibility and conservation of mass, fluid particles in the core of the cylinder are pulled upward along the cylinder axis to replace those traveling out toward the walls. The fluid particles traveling outward encounter the walls of the cylinder, turn downward, still swirling with azimuthal velocity, and eventually circle back into the core of the cylinder.

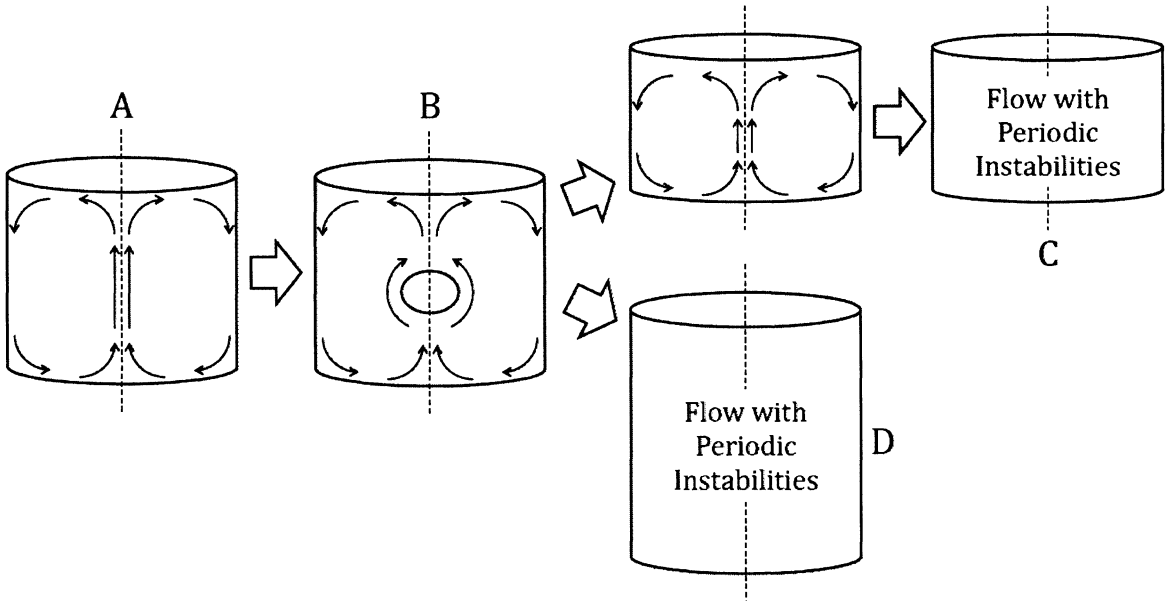

Figure 1.4 – Diagram of general flow dynamics of rotating lid-driven cylinder

The general flow dynamics in a meridional plane and certain flow features of note are described below and diagramed in Figure 1.4. At low Reynolds numbers, the flow forms a concentrated vortex and is steady and axisymmetric (Figure 1.4 – A). However, there is a critical Reynolds number, usually in the range of 1000 to 3500 (depending on aspect ratio), at which region(s) of stagnation and recirculation, sometimes referred to as vortex breakdown bubbles (Figure 1.4 – B), will form at the center of the cylinder vortex (Escudier 1984). Despite these vortex breakdown bubbles, the flow remains steady. However, there is some controversy as to whether the breakdown bubbles are axisymmetric (Spohn et al. 1998; Sørensen et al. 2006). In addition to this vortex breakdown phenomenon, there is also another critical Reynolds number at which the steady, axisymmetric base-flow becomes unstable and a time-periodic instability sets in. At low aspect ratios, the vortex breakdown bubble disappears prior to the occurrence of the periodic instability (Figure 1.4 – C). However at larger aspect ratios, the periodic instability sets in while the vortex breakdown bubbles are still present (Figure 1.4 – D). This periodic flow can be axisymmetric and pulsing or three-dimensional travelling waves, developing patterns in the azimuthal direction corresponding to a variety of mode numbers depending on aspect ratio and Reynolds number (Gelfgat et al. 2001; Sørensen et al. 2006). These periodic instabilities occur with Reynolds numbers on the order of 2500 to 5000. Beyond this, the flow becomes time-dependant and fully three-dimensional. Studies of these periodic instabilities both experimentally and computationally have usually been performed for aspect ratios ranging from 1.0 to 3.5. It is these periodic instabilities that are of interest to us because they can be

used to directly control the flow dynamics within the melt region in the traveling heater crystal growth technique.

The rotating lid-driven cylinder problem has been studied extensively in literature both experimentally and numerically. Most of the early experiments were done in the context of studying the vortex breakdown structure, since the configuration was able to create a vortex in a compact and closed domain. The early observations of location and critical Reynolds numbers of vortex breakdown by Vogel (1968) and Ronnenberg (1977) were confirmed in the landmark paper by Escudier (1984) using dye injection visualization. Escuider also identified the boundary where the steady axisymmetric flow became unstable. More recently Sørensen et al. (2006) performed a detailed laser Doppler velocimetry study of the three-dimensional periodic instabilities for a dense distribution of aspect ratios ranging from 1.0 to 3.5. Sørensen was able to observe both axisymmetric and non-axisymmetric instabilities, and the results can again be used for comparison.

There has also been a wide range of numerical studies performed on this problem. These range from semi-analytical techniques, such as linear stability analysis, to axisymmetric models to direct three-dimensional simulations. The linear stability analysis performed in Gelfgat et al. (2001) identified the critical Reynolds numbers and natural frequencies of the periodic instabilities of interest to us. Gelfgat's results have been supported by both numerical and experimental work currently in the literature and will be used for comparison in this thesis. It should also be mentioned that there are various variations of the basic rotating lid-driven

cylinder configuration, such as iso-rotation or counter-rotation of both top and bottom boundaries on the cylinder. For this thesis, only the "classical" configuration with one rotating lid will be considered. However, future work may include the addition of rotating or axial magnetic fields in order to study how the stability of the system is affected in an effort to apply these techniques to control the melt region in crystal growth experiments.

1.3. Ultrasonic Doppler Velocimetry

The original part of this research comes with the use of Ultrasonic Doppler Velocimetry to measure the flow field for the rotating lid-driven cylinder experimental setup. Both steady "base" flows and identification of the periodic instabilities that transition from the steady axisymmetric base state are of interest. Several experimental studies of the rotating lid-driven cylinder are available in the literature. However, most used visualization techniques requiring a transparent flow media. Dye injection with argon laser illumination was used to produce pictures of vortex breakdowns in Escudier (1984). In another experiment by Sphon et al. (1998), electrolytic precipitation and a particle tracking technique were used, again requiring optically transparent fluids. Most recently Sørensen et al. (2006) utilized particle image velocimetry and laser doppler anemometry in his study to achieve both high spatial resolution and temporal accuracy. Other experimental works of note include Roesner (1990), Stevens et al. (1999), and Sotiropoulos et al. (2002), all of which employed similar visualization techniques.

The Ultrasonic Doppler Velocimeter (UDV) is a device based on emission of ultrasonic pulses that is able to accomplish real-time, non-invasive velocity measurements in a variety of flow media. Because the UDV uses acoustic pulses to accomplish its measurements, an optically transparent medium is not necessary. This makes UDV an ideal choice for working with liquid metals and molten semiconductors. Since the experimental setup designed in this thesis is intended to be used for experiments with liquid metals and axial or rotating magnetic fields, accomplishing accurate measurements with the UDV on this experimental setup (rotating lid-driven cylinder) is a major goal of the thesis.

In the simplest UDV configuration, a single probe is used as both emitter and receiver. The UDV emits several ultrasonic (4-8 MHz) bursts at regular intervals along a line and listens for the echoes that bounce back from particles (either natural or seeded) within the fluid. By comparing the differences between the echoes of two successive bursts, the UDV is able to calculate in real-time the velocity of the flow. One limitation of the single probe configuration is that only velocity projections along the line of the probe are resolved (Figure 1.5). The dotted line in Figure 1.5 shows the direction in which the ultrasonic bursts are propagated and the graph shows the type of data that is produced from the UDV. Sections 2.6 and 3.1.1 address in more detail the specific UDV in this experimental setup.

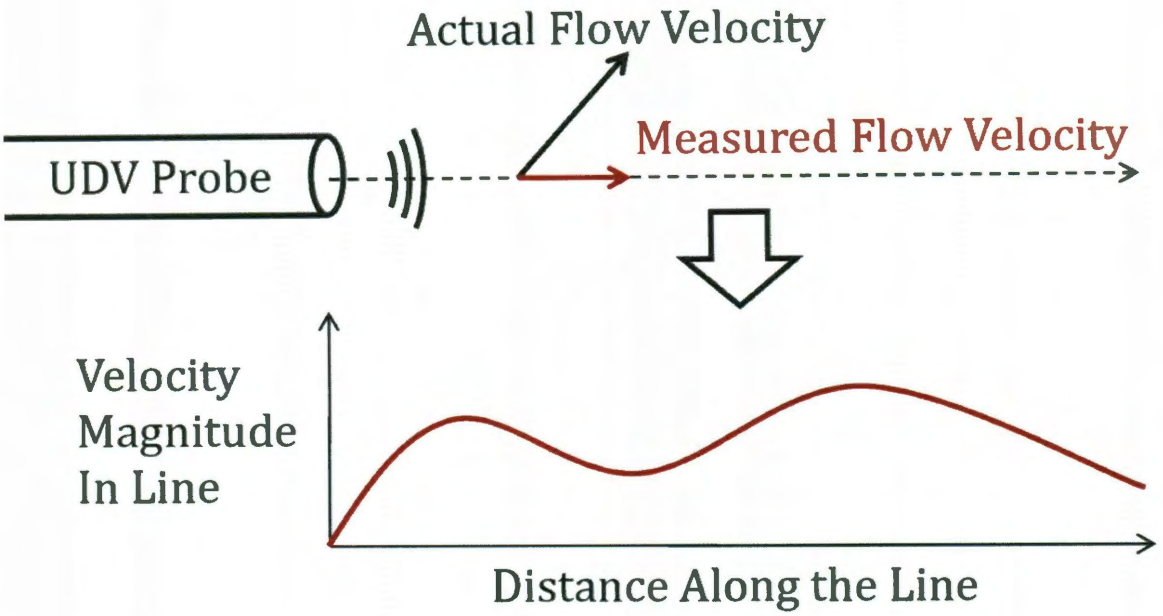

Figure 1.5 – Schematic of Single Probe Configuration

The ultrasonic Doppler velocimetry technique was first demonstrated in 1991 by (Takeda 1991). The technique was originally developed to measure blood flow in the human body, but was never used for its intended purpose. Instead, as problems arose in the human body application, the technique was adapted to accomplish flow measurements in liquid metals and was later found to be useful in flow visualization in a wide variety of fluids. An early survey of the technique can be found in (Takeda 1999). Despite some of its limitations, the UDV has already proven to be effective in measuring flows with similar geometric configurations as the rotating lid-driven cylinder studied in this thesis (Brito et al. 2001; GRANTS et al. 2008). However, challenges with using the UDV for flows with very low velocities

and related challenges encountered with effective bead suspension are addressed in this thesis.

In the remainder of this thesis, construction of the experimental system is detailed in Chapter 2. Chapter 3 describes the experimental and numerical methods used. Chapter 4 will present the experiments and results. Conclusions and future work will be discussed in Chapter 5.

Chapter 2

Experimental System

This chapter presents the design and construction of the experimental assembly, the motor control system, and the Ultrasonic Doppler Velicometer. It begins with details on the construction of the fluid container, UDV probe mounts, and motor/lid assembly. This includes any special insights gained in the construction of each component and any recommendations for future changes. The goal is to provide enough information to enable replication of the assembly. The motor assembly and motor control system are then discussed. Next, the Ultrasonic Doppler Velocimeter used in this work is described. Finally, challenges encountered with the different working fluids used in the experiments are presented.

The entire experimental system is shown in Figure 2.1, with major sub-systems highlighted. The construction of the experimental assembly (A) is presented in 2.1 to 2.3. Selection of the motor assembly and the cRIO motor

controller (B) is discussed in 2.4 and 2.5. The Ultrasonic Doppler Velocimeter (C) will be discussed in 2.6. Finally, the working fluid is addressed in 2.7.

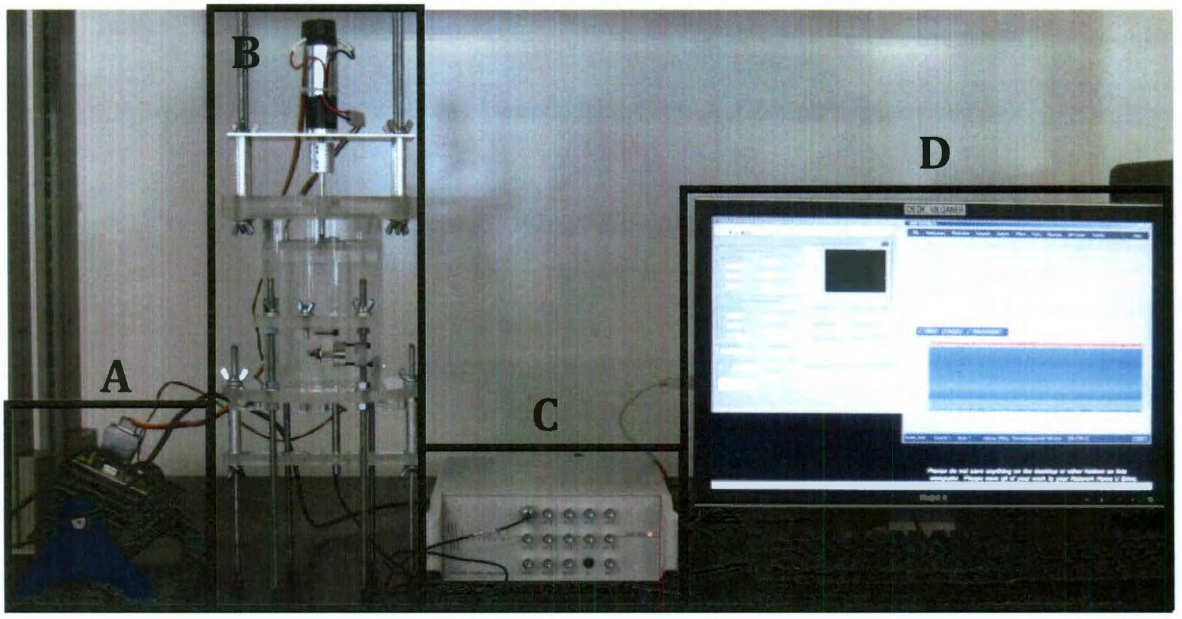

Figure 2.1 – Experimental system with major sub-systems highlighted. (A) cRIO motor controller, (B) expermental assembly, (C) DOP3010 Ultrasonic Doppler Velocimeter, (D) P.C. running DOP3010 software and cRIO interface

A list of all parts, assemblies, and hardware can be found in Appendix A. Appendix A also includes technical drawings of parts, exploded views of assemblies, and assembly instructions. The main body of this section will be devoted to the construction or design of certain components that would not be immediately obvious to a reader trying to reproduce or repair the experimental system. Since some components do not have a descriptive name, they are referred to by their part number in the writing. Figures presented here are labeled with part numbers whenever possible or appropriate.

Most of the components constructed for the experimental system, including the fluid container, the probe mounts, and the rotating lid, are constructed from acrylic. Acrylic was chosen as the container material for its optical transparency and ease of machining. The optical transparency of the acrylic allows for easy troubleshooting and visual inspection of the inside of the cylinder during construction and experiments. The acrylic also has a naturally smooth surface and is easily polished. This eliminates the issue of surface roughness as a significant variable in the experiments. Sheet acrylic is also easily cut into a variety of shapes using a laser cutter and many components can be "roughed out" on the laser cutter before being finished on a mill or lathe. This drastically reduces the amount of machining time and effort necessary. Acrylic is also relatively strong while remaining easy to machine, drill, and tap. Finally, acrylic bonding compound can also be used to weld two pieces of acrylic together with little loss in strength. This provides substantial flexibility when designing an experimental setup.

One drawback of using acrylic as the container material is its inability to handle high temperatures and be used with most liquid metals. Acrylic melts at approximately 160°C, well below the necessary working temperatures of most liquid metals in crystal growth experiments. For the purposes of this thesis, only water and a glycerin-water solution were used as working fluids, thus this material limitation was not an issue. The current setup can also be used without major modification with low melting point metals such as gallium (30°C), mercury (-39°C), or a variety of low melting point metal alloys.

2.1. Fluid Container

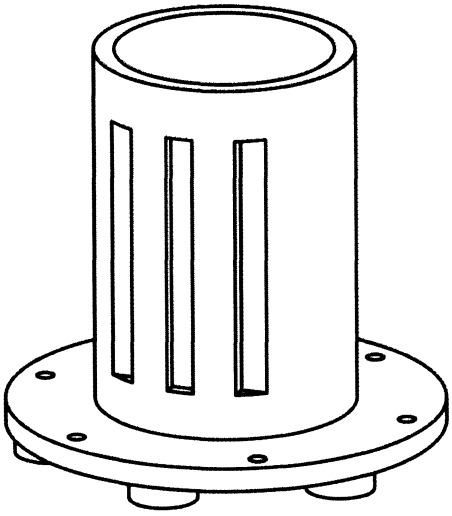

Figure 2.2 – Rendering of fluid container (part 1) without accessories

Figure 2.2 shows a three-dimensional rendering of the fluid container (part 1) with no accessories attached. Although it is technically a single part, the construction involves bonding an acrylic tube to a circular acrylic plate and the construction may not be entirely straightforward. In the discussion of part construction and assembly, English units will be used, since the nominal dimension of stock material and machine tools available to the research group are in English units. The walls of the cylinder are formed from an acrylic tube with an outer diameter of 4.75 inches and an inner diameter of 4 inches. A section of the tube was cut approximately half an inch longer than the desired length and both ends were squared off on the lathe. A series of grooves or bevels were then cut into the sides of the tube. The cuts were accomplished by clamping the cylinder onto the bed of a mill using finger clamps. Small moon shaped scraps of acrylic were used as clamping surfaces. An appropriately sized end-mill was positioned at various

offsets from the center and brought down to specific depths to make the cuts. These bevels aid in the mounting of the UDV probe to the sides of the cylindrical container by providing a flat contact surface. Detailed dimensions for the bevels can be found in the drawings in Appendix A.

The bottom of the fluid container was made from 0.5 in thick acrylic sheet material. A disk 8 inches in diameter was cut out of a stock sheet of 0.5 inch acrylic on a laser cutter (SuperSpeed-660 Universal Laser Systems Inc.). A large circular chuck was then used to grab the disk of acrylic on the outside and a center drill was used to create a small center hole on one side of the acrylic sheet. Special care was taken to ensure that the hole did not penetrate more than half way through the disk, as the other side will come in contact with the fluid. The center hole was used to pressure drive the disk of acrylic so that the outer edge can be turned down until it is smooth and concentric with the center hole. This step was necessary since the laser cutter produces a rough edge and was not able to make a perfect circle. The 6 through holes in the shape of a hexagon were then drilled on the mill using the center hole as a reference point (finger clamps are used to secure the disk). The trench on the bottom of the fluid container was also milled at this time. Note that once this trench is milled, the center hole is lost and the only reference point becomes the outer edge of the disk. The piece was grabbed on the outer edge with a large circular chuck on a lathe in preparation of cutting a circular trench that will mate the acrylic tube to the disk. A 0.125 inch trench with inner and outer diameters matching the acrylic tube were cut in the bottom. An initial cut to the final depth was made with a trench cutting tool approximately in the center of the

trench. This provides two edges on which measurements were taken with digital calipers. Since the acrylic tube will not be perfectly circular or concentric, the inner diameter of the trench was cut to match the smallest inner diameter of the acrylic tube. Then the outer diameter of the trench was slowly enlarged with the trenching tool until the tube was able to sit inside.

Once the trench was cut, the two pieces were ready to be bonded together. The acrylic cement (Weld-on #4) that was used works by chemically melting the two surfaces that are in contact and then evaporating, and allows the two surfaces to become one. This mechanism is more akin to welding than conventional gluing, and is sometimes referred to as "solvent welding." It was important that the two surfaces to be bonded were smooth and flush with each other. Since all work was done on either a mill or lathe with sharp cutting tools, this was not an issue. The acrylic tube was set into the trench on the sheet acrylic and aligned with the bevels by eye to the configuration shown in the drawings (alignment will not be perfect). Once everything was aligned, the acrylic bonding cement was applied with a needle applicator bottle. The cement is water thin and will be naturally drawn into the bonding surface by capillary action. A perfect bond should look clear with cement filling the entire bond region between the two pieces with no air bubbles present. A final visual inspection of the alignment was performed and any gaps in the bonding surface were filled by applying more cement in those areas. The two pieces set within 3 minutes and reached full strength in 24 hours.

Finally six, small circular disks, 1.5 inch in diameter, were cut on the laser cutter from the same 0.5 inch acrylic sheet stock. They were visually positioned in the shape of a hexagon on the bottom of the container and cemented in place. They act as feet for the fluid container.

2.2. UDV Probe Mounts

The array of six holes around the bottom of the fluid container allows 5/16 inch threaded rods (part 23 or 24) to be attached. These threaded rods act as stable mounting posts for the probe mounts and are very versatile. In the configuration used for this thesis, the entire fluid container is supported on stilts using long 5/16 inch threaded rods (part 24) as seen in Figure 2.3. The portion of the threaded rod extending below the fluid container allows the attachment of a probe mount (part 8) that secured probes to the bottom of the container, parallel to the axis of the cylinder. The threaded rods that extend above the fluid container support a probe mount (part 19) that mounted probes to the side of the container, parallel to the radius of the container.

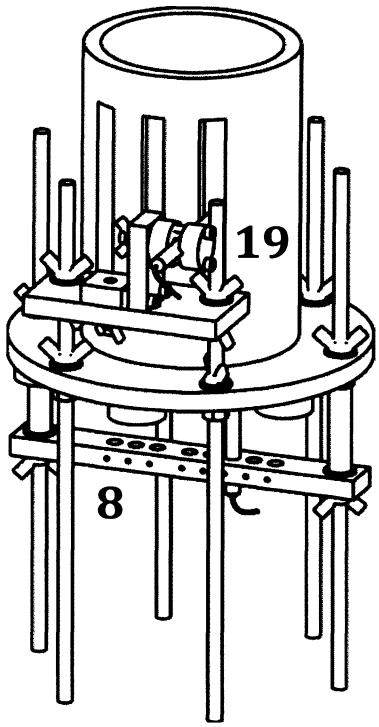

Figure 2.3 – Fluid container with bottom probe mount (8) and side probe mount (19)

The bottom probe mount (part 8) is a bar of acrylic that can mount 5 mm UDV probes perpendicular to the bottom of the fluid container. Construction of this piece was fairly standard; the hole concentric with the center of the cylinder was drilled first and used as a reference. Spaced at regular intervals along the bar are a series of holes that match the outer diameter of the 5 mm UDV probes. There are corresponding tapped holes for a set-screw to hold the probe in place. The probe can be positioned along the center axis of the cylinder or at regular intervals offset in the radial direction. One of the disadvantages of this design is that multiple bars would have to be machined if different sized probes are used. However, since the bars were relatively easy to machine, a more complex mechanical design that could

handle probes of different sizes was not justified. A related feature is the trench that was cut into the bottom of the fluid container (part 1). This trench decreases the amount of acrylic that the ultrasonic pulses must travel through before reaching the fluid and helps reduce scattering and attenuation of the ultrasonic pulse as it passes through the acrylic.

The design of the probe mount (part 19) for the sides of the cylinder is more complex. It has five degrees of freedom and is designed to hold probes of a variety of sizes ranging from 0.1 – 0.5 inch in diameter (Figure 2.4). Components were made from 0.5 inch acrylic sheet stock with embedded metal hardware and held together with 1/4-20 wing-nuts or #6-32 Allen head screws.

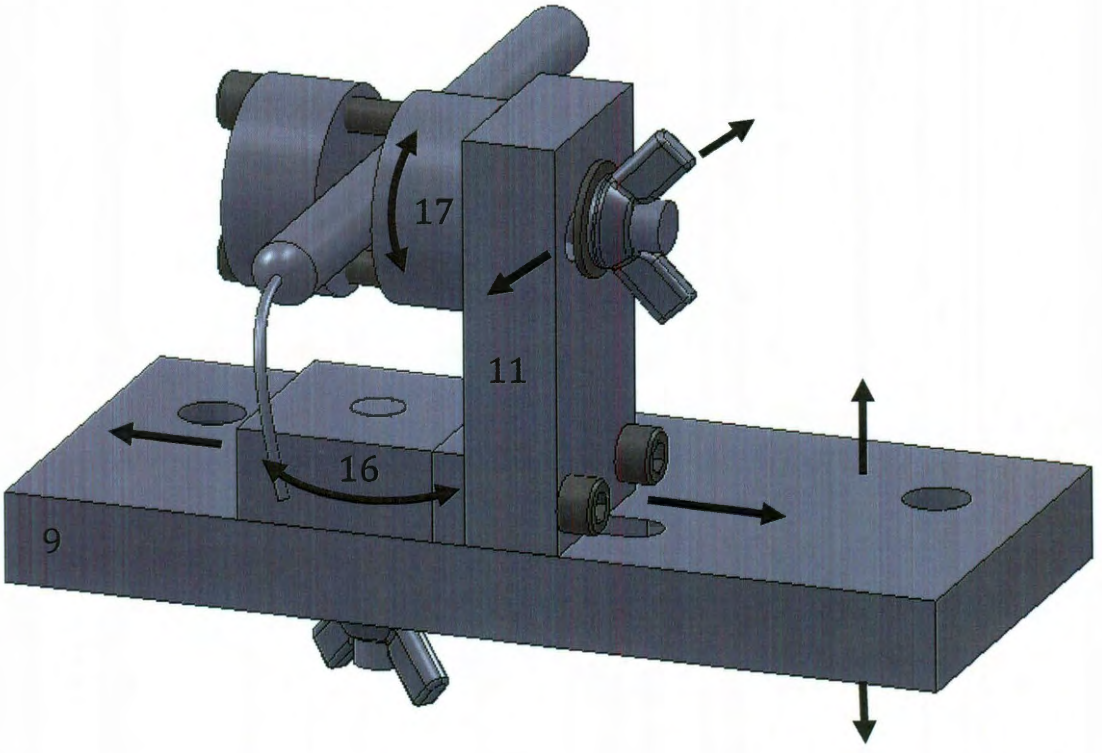

Figure 2.4 – Five degree of freedom probe mount (part 19) for side of fluid container

The platform for the probe mount (part 9) is able to translate up and down along the mounting posts, giving it one translational degree of freedom along the axis of the fluid container. There are also two sliding/rotating joints (between parts 9 and 16 and between parts 11 and 17) that consist of a 1/4-20 shaft that fits inside a 0.25 inch wide track. The shaft is able to both translate and rotate within the track and is secured via a wing-nut. The two sliding/rotating joints provide four additional degrees of freedom and bring the total up to five. Since the UDV probe has one axis of symmetry, one of its spatial degrees of freedom is indeterminate and the five degree-of-freedom probe mount controls all spatial degrees-of-freedom of the probe. In most cases, the probe needs to be mounted perpendicular to one of the flat, side bevels machined into the side of the cylindrical container. Since the probe mount can fully control the UDV probe in space, exact alignment between the bevels and the mounting posts during the process of bonding the cylinder to the base of the fluid container was not necessary.

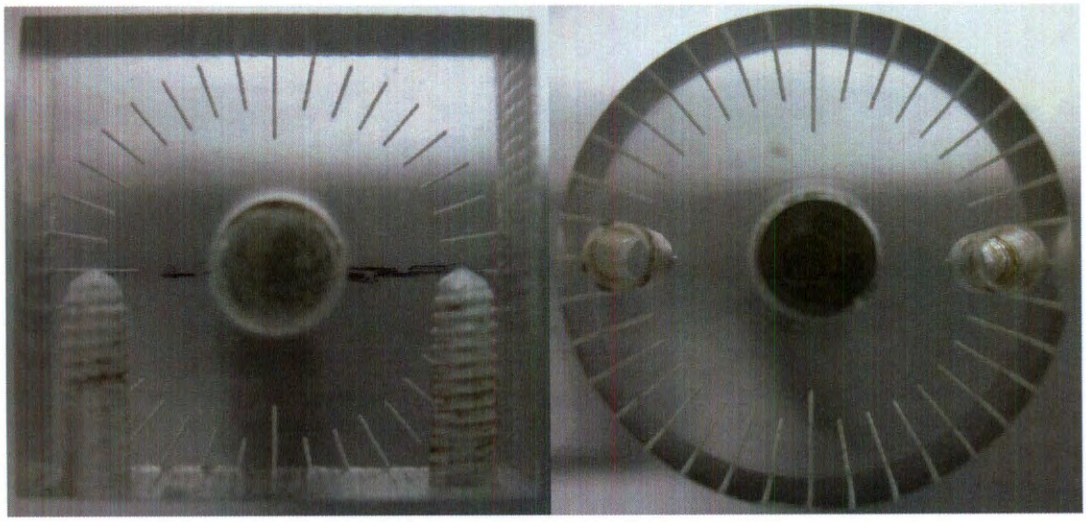

Figure 2.5 – Parts 16 (left) and 17 (right) with alignment marks

There are a few important construction techniques and design features concerning parts 16 and 17 (Figure 2.5). Both parts consist of a small acrylic piece (parts 10 and 12) with an embedded 0.25 inch screw (part 15). Parts 10 and 12 were first roughed out on the laser cutter and alignment marks for an angle dial were etched into the acrylic in the cutting process. These alignment marks can be seen in Figure 2.5 but are not depicted in the drawings in Appendix A. They are spaced every 10 degrees around the hole for the embedded shaft and can be used to set the probe at known angles relative to the platform of the probe mount. Once parts 10 and 12 were roughed out on the laser cutter, the rest of the work was finished on a lathe or mill. One problem was getting proper alignment relative to the etched angle marks when drilling the 0.25 inch hole for the embedded screws. These holes must be perpendicular to the surface of the piece, have a very specific diameter so that the embedded screw can be glued, and be concentric with the angle marks made by the laser cutter. Since the beam of the laser cutter bends and deflects a significant amount as it passes through the 0.5 inch acrylic sheet stock, it was impossible to cut this hole with the laser cutter. Instead, a small pilot hole was made with the laser cutter to mark the center of the angle dial. This pilot hole was then used as a reference point for the hole to be finished on a mill or lathe using a 0.25 inch drill and reamer.

Once the acrylic pieces were finished (parts 10 and 12), the 0.25 inch embedded screws (part 15) were attached. The embedded screw was made by cutting a length of 0.25 inch precision-ground, mild-steel shaft to the proper length and manually threading one end of the shaft. This half threaded steel shaft was then

super-glued (Loctite® 495) into the corresponding hole on the acrylic pieces. Special care was taken when gluing part 17, since any protrusion of the steel shaft or glue will interfere with the UDV probe (see drawing for details).

One issue that was discovered during experiments concerning parts 16 and 17 was that the superglue bond was prone to failure and the 0.25 inch rod would occasionally slip out of the acrylic piece and needed to be re-glued. A more efficient design would use 1/4-20 threaded rods in place of the half-threaded 0.25 inch steel rod and a tapped 1/4-20 hole rather than a straight 0.25 inch through-hole on the acrylic pieces. The 1/4-20 threaded rod could be screwed into the acrylic and secured using thread-lock compound. The resulting piece would be much stronger and easier to make, since 1/4-20 threaded rods can be purchased directly and cut to length rather than manually threading one end of a 0.25 inch steel rod.

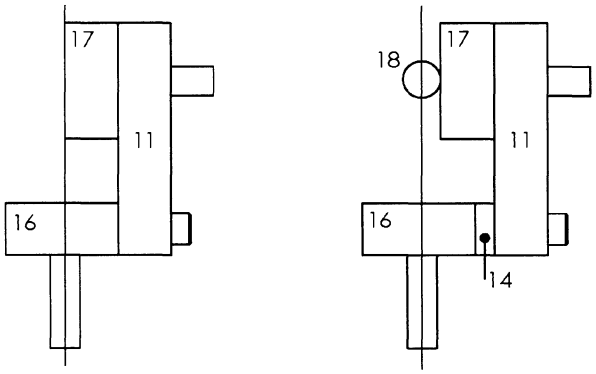

Figure 2.6 – Side probe mount without spacer (left), with spacer (right)

Another subtle design feature of the probe mount was the inclusion of a spacer (part 14), which was sized based on the radius of the UDV probe being used.

The base of the probe holder (part 16) is dimensioned such that, without the spacer included, the surface of the probe clamp (part 17) is coincident with the center line of the embedded screw on which the base rotates (Figure 2.6). By including a spacer that is the same thickness as the radius of the probe, the probe clamp is offset enough such that the centerline of the embedded screw coincides with the center of the probe. This greatly simplifies the kinematics when trying to use the angular alignment marks to position the probe, and allows the holder to be used with probes of different sizes without re-calculating the kinematics. Although the alignment marks were not extensively used in this thesis for positioning the probes, this feature may be useful in the future.

2.3. Motor/Lid Assembly

The motor/lid assembly (part 35) encompasses the rotating lid of the cylindrical container and the motor assembly. It rests on the fluid container, completely enclosing the fluid, and the motor rotates an acrylic disk that acts as the lid to the cylinder. A detailed exploded view of the assembly can be found in Appendix A and is referenced in the section below.

The fluid container top plate (part 2) is a large acrylic disk similar to the base of the fluid container and acts as the main structural support of the motor/lid assembly. It has an array of holes on the outside that allow for mounting posts. The motor (part 7) is mounted to a thin aluminum plate (part 3) which is attached to part 2 via standoffs and mounting posts. The shaft of the motor is concentric with a

bearing mounted in the center of part 2. An acrylic disk (part 6) with an outer diameter slightly smaller than the inner diameter of the fluid container hangs below part 2 and acts as the rotating lid of the cylinder. The shaft on which this acrylic disk is mounted extends through the bearing on part 2 and is clamped to the output shaft of the motor via a shaft coupler (part 21). The output shaft of the motor and the bearing embedded into part 2 act as the two points of support for the rotating disk (part 6).

Construction of the shaft coupler (part 21), the aluminum motor support plate (part 3), and standoffs (part 25) was fairly straightforward from the drawings provided in Appendix A. The top plate (part 2) was constructed in a similar fashion as the base of the fluid container described in Section 2.1. For the top plate, two disks were cut out on the laser cutter from 0.5 inch acrylic sheet stock and bonded together using acrylic bonding cement before further work was done. The piece was then clamped into the lathe and a center drill was used to create a center drill hole. This was then used to pressure drive the disk so that the outer edge was made smooth and concentric. The series of holes in the center of the disk were then made on the lathe by gripping the outer edge of the disk with a large circular chuck. A trough was also cut to match the top of the fluid container so that the motor/lid assembly does not slide around once it is placed on the fluid container. One small difference here is that a second groove was cut within the trough. This groove holds a 4.25 inch rubber o-ring (part 22) which provides some vibration isolation between the motor and the fluid container (shown in exploded view of part 37 in Appendix A).

Great care was taken in the construction of the rotating disk (part 6) that acts as the lid of the fluid container. Since it comes in contact with the fluid and must rotate relative to the walls of the cylinder, the accuracy with which it is constructed directly affects how well the boundary conditions of the problem are replicated. Any eccentricity between the shaft and the disk would cause the disk to wobble laterally as it rotates. Of even greater concern is the angle that the shaft makes with the disk. If the shaft of part 6 is not mounted perfectly perpendicular to the bottom surface of the disk (Figure 2.7), rotation of the disk would introduce velocity perturbations to the flow that are parallel to the axis of the cylinder. These perturbations may trigger instabilities that would normally be unobservable.

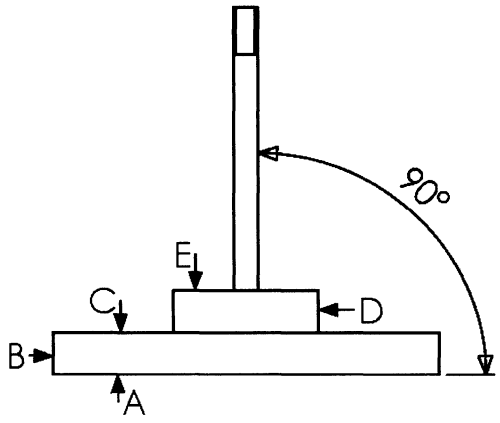

Figure 2.7 – Rotating disk (part 6) with critical angle marked and important surfaces lettered

To begin construction of part 6, the spinning acrylic disk (part 4) was constructed first. Two disks were cut from 0.5 inch acrylic sheet stock. The larger disk was made to approximately 0.25 inches larger than the desired diameter. The

diameter of the smaller disk is not significant and was arbitrarily chosen to be 1.5 inches. During the laser cutting process, the centers of both disks were engraved with a small circle (only marks the surface of the acrylic and does not actually make a hole in the center of the disks). Usually there is a protective film that covers the stock acrylic material. This film was removed from both sides of the smaller disk, but to protect the surface that comes in contact with the fluid, the protective film was only removed on the engraved side of the larger disk. The two disks were then aligned concentrically by lining up the engraved center marks. The alignment of the centers does not need to be exact but any error should be kept less than 0.25 inches. The two pieces were bonded together using acrylic bonding cement and left overnight to reach full strength. The purpose of the smaller disk bonded to the larger disk is two-fold. First, it provides extra support for the stainless steel shaft that will be mounted to the rotating disk. Second, it also helped significantly in the construction of the piece since it provided a secure location to mount in a lathe as the outer diameter of the larger disk was reduced to the desired size.

Once the acrylic bond reached full strength, final machining was finished on part 4. The outer edge (surface B in Figure 2.7) of the large disk was grabbed in a circular chuck on the lathe with the protruding small disk facing outward (toward the tool). The bottom surface of the large disk (surface A) was butted against the back surface of the chuck so that surface A was perpendicular to the Z-axis of the lathe. Using a standard cutting tool, the diameter of the smaller disk was reduced until the outer edge of the small disk (surface D) was perfectly circular. Using the automatic feed in the Z-direction resulted in a much smoother surface than

advancing the tool by hand. Note that these cuts were taken until the tool face scratched surface C. Next, the same tool was used to take approximately 50 thousands of an inch off of surface E by advancing the tool in the X-direction. This cut corrects thickness variations caused by gluing the two acrylic pieces together and makes surfaces A, C, and E perfectly parallel to each other. After this series of cuts, surfaces A and E should be parallel to each other. The smaller disk should have a perfectly round outer edge (D) and surface D should be perpendicular to A and E. Without removing the piece from the lathe, the hole for the 1/4-20 tap that goes in the center of the disk was made. A pilot hole was first drilled with a center drill to minimize tool deflection when making the actual hole. Next, the 1/4-20 hole was tapped using the tailstock of the lathe to ensure that the tap was advanced perpendicular to surface A.

At this point the piece was removed and re-clamped into the lathe by grabbing the protruding small disk (surface D). Surface C was butted against the surface of the chuck teeth to align surface A perpendicular to the Z-axis of the lathe. Since surface D was perfectly concentric with the tapped hole that was drilled, the outer edge of the large disk (surface B) can now be cut down to the proper diameter to fit within the acrylic cylinder. Generous cuts (50 thousandths) were made until the disk approaches the correct diameter, again advancing the tool in the Z-axis with the automatic feed resulted in a much smoother surface. As the correct diameter was reached, cuts of 10 or 5 thousands were taken on the diameter and the fluid container was used to test the fit between each cut. Cuts were made until the disk just barely fit into the acrylic tube. Additional cuts can always be made in the future

if the disk is found to be too large and is scraping the sides of the acrylic tube. However, if the disk is accidentally made too small, a new one must be machined.

Construction for the acrylic disk (part 4) was now complete and the stainless steel shaft (part 5) can be constructed. A piece of 0.25 inch, mild, precision-ground, stainless steel shaft was cut to the correct length and squared and beveled on both ends. Next, one end of the shaft was manually threaded by single-point threading on the lathe for 1/4-20 threads. The threads were 0.25 inches longer than necessary as a margin for error. Finally, the shaft was clamped into the mill and an end-mill was used to create the flat surface on the other end for set-screws.

The process of thread-locking the stainless steel shaft (part 5) into the acrylic disk (part 4) was also very critical. Because of the low tolerances to which threads are machined, there will be significant wobble between the steel shaft and the acrylic disk if no thread-locking compound is used. In order to permanently secure the shaft to the acrylic disk in a perpendicular fashion, a thread-locking compound is used and the shaft and disk are held in a perpendicular configuration during the entire drying period. Loctite® Threadlocker Blue 242® was used as the thread-locking compound and a v-block and v-block clamp were used to hold the shaft and acrylic disk in a perpendicular configuration during the drying process. The shaft was clamped into the v-block using a v-block clamp with the threaded end protruding 0.5 inches from one end of the v-block. The thread-locking compound was then applied to the threads on the acrylic disk and the shaft. The acrylic disk was screwed onto the shaft until surface E comes in contact with the v-block and

tightened slightly. The tension in the threads held the disk against the v-block and perpendicular to the shaft until the thread-locking compound set. After the bond reached full strength overnight, part 6 was complete.

2.4. Motor Assembly Selection

The motor assembly consists of a brushed DC motor, a planetary gearbox, and an encoder for velocity feedback. The specifications of the selected assembly are shown in Table 2.1. A brushed DC motor was chosen for its relative ease to power and control. The maximum operating torque was not a concern since the viscosities of the fluids used were so low that the motor would be operating under minimal load. Choice of the gearbox was made based on a few factors. In the design of the motor/lid assembly (part 35), the output shaft of the gearbox is directly connected to the shaft of the rotating lid and must act as one of the two points of support for the shaft. Thus, a relatively large gearbox (6 mm output shaft) with a ball-bearing output shaft was selected even though the maximum operating torque on the gearbox far exceeds the torques expected in the system. Since the motor would be rotating in a single direction at a constant speed, backlash within the gearbox was not a concern and a planetary gearbox was suitable. A standard optical encoder with 500 counts per turn was chosen to provide a means for velocity feedback. With sub-degree resolution on the rotation of the motor shaft, the encoder was more than sufficient to accurately determine the velocity of the output shaft of the gearbox.

Motor	
Maxon Part #	236655
Type	Brushed, DC
Nominal Voltage	24 V
Nominal Power	14 W
Nominal Speed	6000 RPM
Max Continuous Current	1 A
Max Continuous Torque	36.7 mNm
Gearbox	
Maxon Part #	166161
Type	Planetary
Reduction	23:1
Number of Stages	2
Max Continuous Torque	2.25 Nm
Encoder	
Maxon Part #	110513
Counts per Turn	500
Channels	3

Table 2.1 – Motor assembly specifications

Choice of the maximum speed for the motor and gearbox reduction ratio depends greatly on the working fluid and the degree of flexibility desired. A low reduction gearbox would allow the setup to achieve a higher maximum rotation rate and thus higher Reynolds numbers (equation (1.2)). However, since brushed DC motors are difficult to control smoothly at low rotation rates, a low reduction gearbox would also mean poor control at low Reynolds numbers. The optimal choice for the gearbox reduction would depend on the viscosity of the working fluid

and the desired Reynolds number range. Suppose the lowest desired Reynolds number was 500 and the highest is 5000. Sample calculations of the required rotation rates, assuming the radius of the rotating lid-driven cylinder is 2 inches as in this experimental setup, are shown below in (2) to (2.7).

$$R = 2\ inch = 0.0508\ m \tag{2.1}$$

$$\nu = kinematic\ viscosity\ in\ \frac{m^2}{s} \tag{2.2}$$

$$Re = \frac{\Omega R^2}{\nu} \tag{2.3}$$

$$500 = \frac{\Omega_{low}(0.0508\ m)^2}{\nu} \qquad 5000 = \frac{\Omega_{high}(0.0508\ m)^2}{\nu} \tag{2.4}$$

$$\Omega_{low} = 1.9375 \times 10^5 \nu\ \frac{rad}{s} \quad \Omega_{high} = 1.9375 \times 10^6 \nu\ \frac{rad}{s} \tag{2.5}$$

$$\begin{aligned} \Omega_{low} &= 1.9375 \times 10^5 \nu\ \frac{rad}{s} \times \frac{1\ rev}{2\pi\ rad} \times \frac{60\ s}{1\ min} \\ &= 1.85 \times 10^6 \nu\ \ RPM \end{aligned} \tag{2.6}$$

$$\Omega_{motor} = \Omega_{lid} \times Gearbox\ Reduction\ Ratio \tag{2.7}$$

Using viscosities for water, 80% glycerin-water by volume at 20°C (Cheng 2008), and liquid gallium (Brito et al. 2001) , Table 2.2 summarizes the minimum and maximum required motor rotation rates given a gearbox reduction ratio of 23:1. Due to the large variations in the viscosities of various fluids, the required minimum and maximum rotation rates for the motor (right column Table 2.2) vary dramatically depending on the working fluid. The gearbox ratio was selected so that the minimum required rotation rate was on the order or 50 or 100 RPMs to ensure controllability of the motor at the desired low Reynolds number. For the

configuration used in this experimental setup, a motor with a maximum rotation rate of 6000 and a 23:1 reduction gearbox was selected. This puts water on the lower end of the operating speeds for the motor/gearbox combination and gives the flexibility of using working fluids with higher viscosities. However, if future experiments are to be done with liquid metals, a higher reduction gearbox is necessary since the lower viscosity liquid metals would require a motor with the 23:1 gearbox to run at speeds too low to ensure controllability. Likewise, if experiments on the fluids with much higher viscosities are desired (80% glycerin-water solution), a lower reduction gearbox would be necessary to bring the maximum required motor speed down to 6000 RPMs.

	$\nu\left[\frac{m^2}{s}\right]$	Required Ω_{lid} [RPM]		Required Ω_{motor} [RPM] (Gear Ratio = 23:1)	
		Low	**High**	**Low**	**High**
Water	1.00×10^{-6}	1.85	18.50	42.6	425.5
80% Glycerin-Water	4.10×10^{-5}	76	760	1748	17476
Gallium	3.1×10^{-7}	0.57	5.74	13.2	131.9

Table 2.2 – Required rotation rates with 23:1 gearbox sample calculations

2.5. The Motor Control System

Control of the motor that drives the lid on the experimental setup was accomplished using an NI cRIO-9014 – CompactRIO Real-Time Controller with an NI 9505 module. The NI 9505 module is a full H-bridge brushed DC servo motor module and features a built in encoder interpreter and current sensor. The NI cRIO-9014 is necessary to use the NI 9505 module and allows the user to create custom software that controls the module and ultimately the motor. A schematic of the architecture of the control system is shown in Figure 2.8.

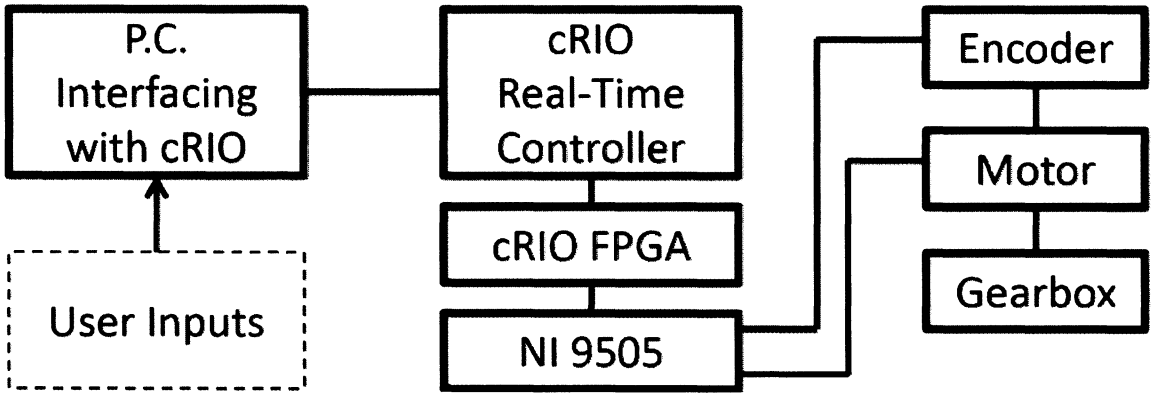

Figure 2.8 – Architecture of motor control system

The cRIO real-time controller is part of the cRIO chassis and can be thought of as an onboard computer that is capable of storing and executing virtual instruments (VIs). VIs are essentially National Instruments' name for programs with a graphical user interface. Also embedded into the cRIO chassis is the cRIO FPGA (Field Programmable Gate Array) which handles the low level logic and processing. Together the real-time controller and the FPGA make up to the cRIO-

9014 chassis and can be thought of as a portable computer that is capable of running VIs but that has no operating system. By itself, the cRIO-9014 has no input/output capabilities; instead it relies on a full range of modules that look like cartridges that plug into the chassis. One of the available modules for the cRIO-9014 is the NI 9505, which gives the cRIO the ability to control brushed DC motors. The NI 9505 has a full H-bridge motor driver, current sensor, and encoder interface for velocity feedback. Separate power sources are required for the cRIO-9014 and the NI 9505. The power source connected to the NI 9505 should be rated to the same voltage and current as required for the motor since the NI 9505 does not have an onboard voltage regulator and simply acts as a switch between the power source and the motor. Custom wire leads and ribbon cable connectors were made to connect the NI 9505 to the motor and encoder. Finally, a personal computer running NI Labview connects to the cRIO-9014 via an Ethernet cable allowing the user to compile and run VIs as well as providing a visual interface for the user.

In order to accomplish velocity control for the motor, two Labview VIs were used. The framework came from sample VIs provided by Labview but major modifications were required to make them usable. The first VI runs on the FPGA and interfaces between the FPGA and the NI 9505 (FPGA VI). This VI samples the motor current, keeps track of encoder counts, and runs two PID controllers which regulate a PWM (pulse-width modulation) signal to the motor. The second VI runs on the real-time controller of the cRIO and is akin to a driver program for the FPGA VI. This driver VI obtains user inputs for the controller gains, desired velocity, and other parameters and feeds them to the FPGA VI. The driver VI is also responsible

for displaying the velocity and status of the motor and interfaces with the personal computer to provide the graphical user interface. The paragraphs below briefly describe the structure of the VIs and how they work.

Within the FPGA VI, the two major tasks being accomplished are tracking of encoder counts and running the two PID control loops. All loops running on the FPGA are referenced to a 40 MHz internal clock which provides vary accurate timing for computing rotation rates from encoder information. An encoder is a device attached to the rotating shaft of a motor that produces a digital signal as the shaft rotates. The digital signal is made up of a series of two square waves and there is a characteristic number of counts per turn produced by the encoder (Figure 2.9). The two square waves are offset a quarter of a wave length in phase so that the direction of rotation can be determined by monitoring whether channel A leads channel B or vice versa. The built-in encoder interface for the NI 9505 actually counts the rise and fall signal of each encoder channel as a separate encoder tick. This quadruples the resolution of the encoder and the 500 count per turn encoder actually produces 2000 ticks per turn. This is illustrated in Figure 2.9.

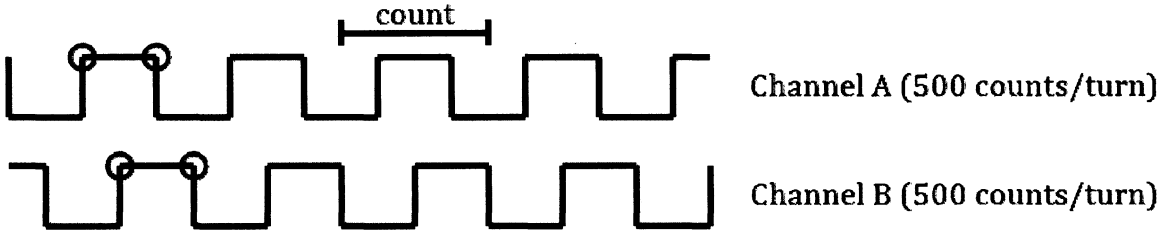

Figure 2.9 – Diagram of signals from encoder channels; circles mark points where NI 9505 registers a tick.

The encoder loop within the VI tracks the total number of encoder ticks as well as the amount of time that has elapsed between the last two encoder ticks. The VI computes the rotation rate by using the elapsed time between the last two encoder counts and reports this value to the driver VI running on the real-time controller.

The other main function of the FPGA VI is running the two PID control loops which regulate a PWM signal to the motor. The controller gains and velocity set-point are provided to the FPGA VI by the driver VI. The architecture for the two PID controllers is shown below in Figure 2.10.

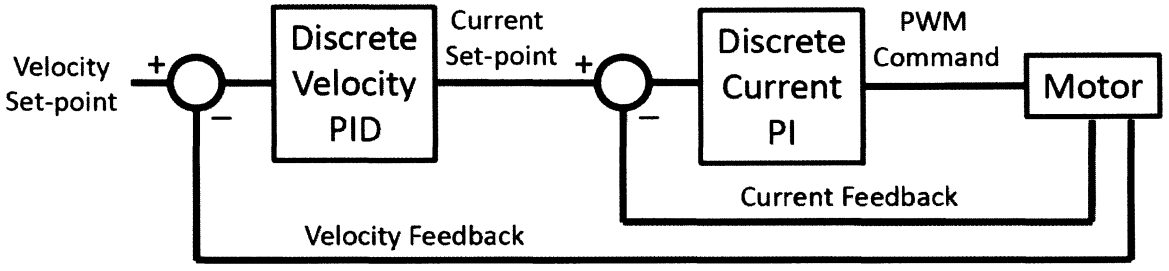

Figure 2.10 – Architecture of discrete velocity controller

The NI 9505 is able to obtain two feedback variables from the motor: the velocity or rotation rate and the current. Starting with a desired velocity for the motor, a velocity error is computed and fed into the discrete velocity PID control loop. This control loop outputs a command current for the motor based on the error in the velocity signal and the gains provided. This command current is then compared to the measured current from the motor and the computed current error is fed into a second PI controller. The output from this current PI control loop determines the duty cycle of the PWM signal, which ultimately drives the motor.

The discrete PID control loop on the velocity runs once every 600 μs and the PI control loop for the current runs 10 times faster, once every 60 μs. These values were determined during experiments to provide relatively good performance. The basic calculations for each control loop are performed by a built-in discrete PID function that is part of Labview software package. One of the limitations of this discrete PID function is that it can only accept integer values for the control variables and only output integer values. Thus, creative choices for the scaling of all variables had to be made in order to obtain desirable resolutions. For example, rather than representing the rotation rate of the motor as a decimal value which must be computed from the time elapsed between encoder counts, the motor velocity was represented as the number of encoder ticks that have occurred within one cycle of the velocity control loop. By using this representation of the motor velocity, the FPGA VI only has to store a single integer value and perform a single integer subtraction operation every loop cycle in order to compute the feedback velocity. The appropriate set-point value is computed by the driver VI, as shown in (2.8) and (2.9) and provided to the FPGA VI. Δt is the velocity loop period.

$$\Omega_{desired}\frac{rev}{min}\times\frac{2000\ ticks}{rev}\times\frac{1\ min}{60\ s}\times\ \Delta t\frac{s}{loop}=\#\ \frac{ticks}{loop} \tag{2.8}$$

$$\begin{aligned} 180\frac{rev}{min}\times\frac{2000\ ticks}{rev}\times\frac{1\ min}{60\ s}\times(600\times10^{-6})\frac{s}{loop} \\ =3.6\frac{ticks}{loop} \end{aligned} \tag{2.9}$$

Note that because Δt is so small, the number of ticks per loop may be very small (only 3.6 in the above example) and can have a decimal value. Since these values

must be rounded to an integer for the discrete PID function, this results in poor resolution of 50 motor RPM for every 1 tick/loop. In order to improve the resolution of the controller while still working with only integer values, both the set-point velocity value and the feedback velocity are multiplied by a factor of 20 before rounding. This increases the resolution of the controller and serves as a work around for the controller's inability to manipulate decimal values.

Scaling for the PI controller on the motor current was more straightforward. The NI 9505 provides the current feedback as an integer value with the units of $1/162^{nd}$ of an Amp. The command current produced by the velocity control loop is compared against the measured motor current and the error is fed into a discrete PI controller. The output from the this controller is fed into a PWM signal generator with 0 corresponding to 0% duty cycle and 2000 corresponding to 100% duty cycle. Since the motor current can change very quickly, the derivative gain was not used to avoid instability in this control loop. The purpose of having this control loop on the motor current is to prevent over loading the motor in situations where the motor has stalled due to physical obstruction.

The gains for the two discrete PID controllers are shown in the Table 2.3. Since the motor is relatively easy to control, all gains were determined experimentally through trial and error. The control requirements on the motor were relatively simple: have the ability to ramp to and hold at a constant velocity. Since the time scale of the motor is much shorter than the expected dynamics of the fluid, only the steady-state response of the system was significant. It would also be desirable to

avoid any oscillations in the velocity of the motor as it progresses from one set-point to another, since these could create unwanted perturbations in the flow. Given these two facts, the gains were adjusted until the system was over-damped with a small integral gain on each controller to improve steady-state tracking.

Parameter	Velocity Loop	Current Loop
Loop Period [μs]	600	60
Proportional Gain	5	1
Integral Gain	0.01	0.01
Derivative Gain	1	0

Table 2.3 – Controller gains for velocity and current loop

2.6. Ultrasonic Doppler Velocimeter

A DOP3010 Ultrasonic Doppler Velocimeter (UDV) manufactured by Signal Processing S.A. was used as the fluid visualization for the work presented in this thesis. The device employs pulsed ultrasonic waves in order to accomplish its velocity measurements. A probe sends out packets of ultrasonic waves into the flow media and then measures, at specific time intervals after the emission of the sound pulses, the reflected echoes returned by seed particles or natural impurities in the fluid. This process is repeated many times a second (based on the Pulse Repetition Frequency) and by comparing successive measurements using statistical correlations, the velocity component of the fluid parallel to the direction of the ultrasonic pulse is deduced. A more detailed explanation of the underlying working principles of the device can be found in (Willemetz) and (Messer).

The software package used to collect data from the DOP3010 is also provided by Signal Processing S.A. and all optional software packages were installed. These optional software packages allow the control of some parameters of the device that are not available under the basic software package. Although the DOP3010 is capable of controlling up to 10 different probes, it was found that simultaneous measurements cannot be accomplished from multiple probes. The device is only able to switch from one probe to the next and collect data from each probe sequentially. Since our experiment would benefit only if samples can be obtained from different probes simultaneously, all experiments presented in this thesis

utilized a single probe. A schematic of the data acquisition system is show in Figure 2.11 below.

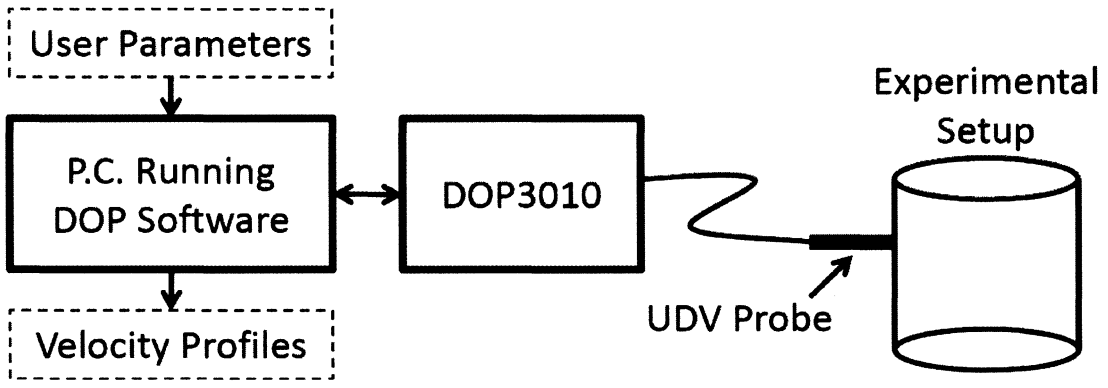

Figure 2.11 – Schematic of UDV data acquisition system

The UDV probe was mounted to the experimental setup in order to record the velocity profile. The probe was connected to the DOP3010 via a BNC connector. The DOP3010 provides excitation to the probe and performs all of the low-level computations associated with producing a velocity profile. The DOP3010 was connected to a personal computer running the DOP software and communicates via a USB connection. The DOP software can be used to set operating parameters and ultimately produces the velocity profiles of interest. These velocity profiles can be viewed in real-time in the DOP software and stored into binary files for post processing or further visualization.

The performance of the UDV is greatly affected by a number of parameters that must be set within the software package. These parameters affect both the spatial and temporal resolution of the velocities profiles that are obtained as well as

the amount of noise that is present in the velocity profile. Figure 2.12 shows a screenshot of the operating parameters in the DOP software. The section below will give a general description of each parameter and its significance. The section following outlines how each parameter was selected for the experiments presented in this thesis.

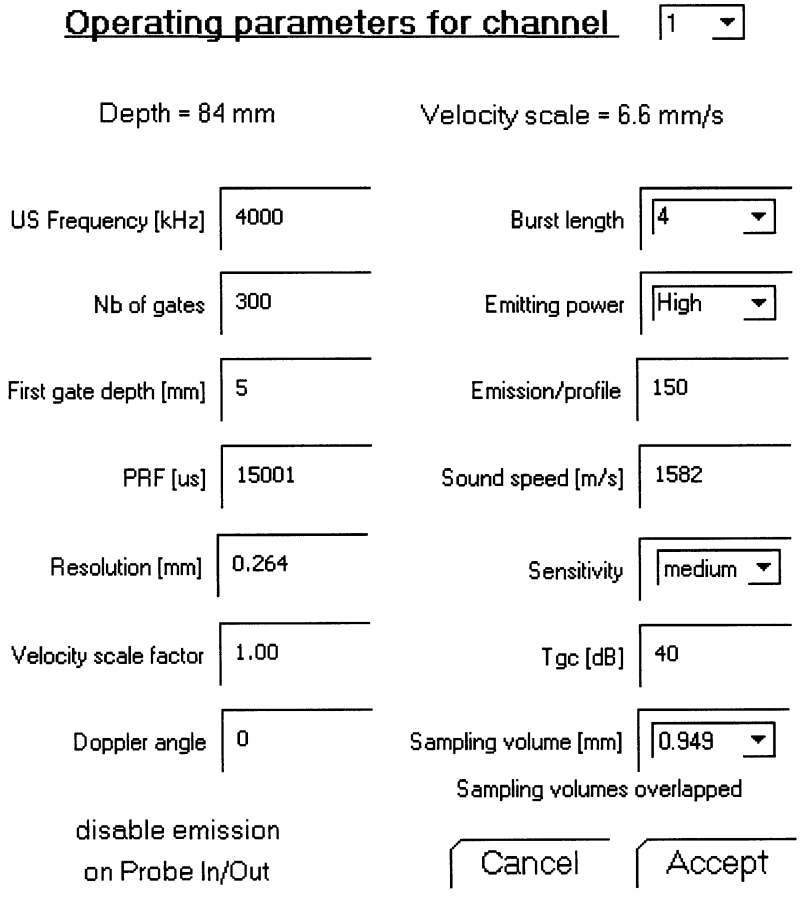

Figure 2.12 – DOP software operating paramters

To begin, the parameters that can be set immediately include the "Sound speed" and the "US Frequency". The "Sound speed" parameter is the acoustic

velocity in the flow media under investigation. Since the UDV technique is based on the emission and reception of ultrasonic pulses, knowledge of the acoustic speed is necessary in many internal calculations. A small position bias in the velocity profile may result when the ultrasonic beam must pass through multiple materials with different acoustic speeds, such as the container and the fluid itself.

The "US Frequency" is determined by the probe being used. For all experiments presented in this thesis a 5 mm transducer, 4 MHz probe (TR0405LS) was used. The ultrasonic frequency is also used in many internal calculations and determines, in part, the spatial resolution and the maximum measurable velocity. The ultrasonic frequency also determines the amount of attenuation in the signal; higher frequencies attenuate more than lower frequencies. The probe that was used for this thesis was recommended by the manufacturer of the UDV for this application and is similar to the probes used in related studies (Eckert and Gerbeth 2002; Eckert et al. 2003; Grants et al. 2008).

To set the special resolution and the domain in which the UDV generates the velocity profile, several "gate" parameters are set. As mentioned in Section 1.3, the UDV is able to provide the velocity component of the fluid parallel to the line of propagation of the ultrasonic pulse as a function of distance along that line. However, it does not do this in a continuous fashion. Instead, the velocity is computed as the average velocity of particles within a small volume of fluid known as a "gate" or sampling volume. These gates are not physical manifestations within the fluid. They are a product of when and for how long the UDV samples the echoes

that it receives. These gates are placed at discrete, uniformly distributed points along the line of propagation of the ultrasonic beam. Figure 2.13 below shows UDV gates idealized as cylindrical volumes of fluid and the line of propagation of the ultrasonic beam shown as the dotted line along which the gates are distributed.

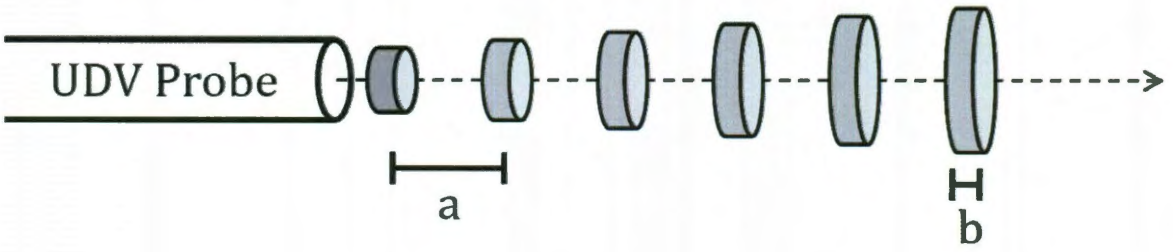

Figure 2.13 – UDV gates along line of propagation

The distance 'a' is the gate spacing (center to center) and 'b' denotes the longitudinal gate size. The UDV averages the particle velocities parallel to the line of propagation within each gate and returns this average value for each gate. Thus the "velocity profile" that is produced is fluid magnitudes in the direction of the line of propagation as a function of the distance along that line.

Figure 2.13 depicts the gate spacing and gate size set such that a > b. In this case, the sampling volumes do not overlap and there are regions within the flow that are not measured. However, it could be the case that the parameters are set such that b > a. In this case, the sampling volumes actually overlap each other and averaging occurs over a region that is larger than the gate spacing. Although this may seem disconcerting, the UDV manual (Willemetz) states that overlapping sampling volumes are common when high spatial resolution is desired. It should

also be noted that in reality, the gates or sampling volumes are not perfect cylinders with well defined boundaries. Instead they are more tear shaped and have boundaries that blend into the rest of the flow making any overlap of sampling volumes less significant (Messer). The lateral size of the sampling volume (measured perpendicular to the dotted line in Figure 2.13) also changes since the ultrasonic pulses tend to diverge outward as they travel through the fluid. Thus the gates that are further from the probe have a larger lateral dimension when compared to gates closer to the probe tip. The amount of divergence experienced by the ultrasonic beam for the 5 mm, 4 MHz probe is on the order of 5 mm of lateral expansion at 100 mm from the tip of the probe (Messer).

The longitudinal gate size (measured parallel to the line of propagation) is set by the "Sampling volume" drop down menu on the bottom right of the parameters list as seen in Figure 2.12. There are only 6 discrete values of the sampling volume size available and these discrete values are a function of the burst length and acoustic velocity. The gate spacing or "Resolution" can be set in millimeters in a range of 0.132 mm to 20 mm in steps of 0.132 mm, but the step size and minimum size is also a function of the acoustic velocity.

To fully specify the domain in which the velocity profile will be generated, the location of the first gate and the number of gates must be provided. This determines both the start and end location of the measurement domain. The maximum number of gates available is 1000 and the maximum depth at which a measurement can be obtained is dependent on the Pulse Repetition Frequency and

the acoustic velocity. The idea behind maximum measurable depth is that there must be sufficient time for a pulsed ultrasonic beam to reach a certain depth beyond the probe and reflect back to the probe before another pulse needs to be sent. In general, one would first choose a "Sampling volume" size and "Resolution" that would be able to resolve the changes that are expected for the investigation. The first gate location and the number of gates can then be chosen to fully span the domain in which velocity profiles are desired. In occasions where the desired measurement domain is very large, the resolution or gate size may need to be enlarged to accommodate the limit on the maximum number of gates.

Special consideration also needs to be taken in setting the location of the first gate due to a phenomenon called "ringing." Ringing refers to the continued vibration of the ultrasonic transducer housing for a few microseconds even after excitation to the transducer is removed. Thus when the probe sends out an ultrasonic pulse the entire probe experiences ringing for a short period of time after the excitation is removed. The probe is unable to accurately measure the reflected echoes during this period of time because the ringing effect saturates the sensors. However, since the ringing effect is only present for a few microseconds, only the region a few millimeters from the tip of the probe is affected. Thus the UDV is unable to obtain accurate velocity profiles for the first few millimeters beyond the tip of the probe. Since our probe is mounted on the outside of the fluid container a first gate depth of 5 mm is chosen and most of the effects from ringing are avoided.

Another important operating parameter for the UDV is the pulse repetition frequency (PRF). The PRF determines the frequency at which ultrasonic pulses are emitted into the flow media and in effect acts as the sampling frequency of the UDV. It directly affects the maximum measurable velocity, the maximum measureable depth, the degree to which transient behavior within the flow is averaged, and the quality of the measured velocity profile. For a given mean fluid velocity, if the PRF is too low the fluid particles move too much between emissions and the UDV is not able to measure the velocity without aliasing. For a PRF that is set too high, there is no discernable change in the fluid particle positions between emissions and the flow appears stagnant even when there is movement. The PRF also affects the maximum measurable depth since an ultrasonic pulse must be given sufficient time to travel through the measurement domain and produce echoes before another pulse is sent. Simple equations given in the DOP manual that relate the PRF to the maximum measureable depth and maximum measurable velocity are reproduced below:

$$P_{max} = \frac{C}{2 \cdot F_{PRF}} \tag{2.10}$$

$$V_{max} = \frac{F_{PRF} \cdot C}{4 \cdot f_e} \tag{2.11}$$

where P_{max} is the maximum measurable depth in [m], C is the acoustic velocity in [m/s], F_{PRF} is the PRF in [Hz], and f_e is the emitting frequency in [Hz]. In general the PRF is chosen based on the maximum velocity that is anticipated in the flow field rather than the maximum desired depth that needs to be measured. This produces a much cleaner velocity profile and the measurement domain depth can always be adjusted by varying the gate properties described in the previous paragraphs.

Along with these two important metrics, the PRF also has an effect on the amount of noise in the velocity profile and the overall temporal resolution of the UDV. The PRF is set by specifying the pulse repetition period in microseconds and is adjustable between 64 to 64,000 microseconds in steps of 1 microsecond.

The number of emissions per profile and the PRF in combination determine the temporal resolution and overall sampling rate of the UDV. Since the UDV produces velocity profiles by performing statistical correlations on the echoes it receives, a velocity profile generated by a single emission is prone to noise. Insufficient echo strength in certain portions of the domain due to scattering of the ultrasonic beam or interference patterns of weak, residual ultrasonic pulses still reverberating in the measurement domain can cause measurement artifacts and noise in the velocity profile. These problems can be greatly alleviated by simply averaging multiple emissions to generate a single velocity profile. Tens or even hundreds of emissions can be used to generate a single profile in order to produce a clean, relatively noise free velocity profile. However, this reduction in noise and artifacts comes at the price of lower temporal resolution, since the effective sampling rate of the UDV would be decreased by a factor equal to the number of emissions per profile. In general this is not an issue, since the PRF is usually on a much faster time scale than any transience or periodicity in the flow field. After choosing the PRF based on the maximum anticipated velocity in the flow field, the number of emissions per profile can be increased until noise is reduced to an acceptable level or until the sampling rate is reduced to the lowest acceptable range in order to capture some transient or periodic behavior of interest.

There are also operating parameters for the UDV that directly affect the amount of noise and measurement artifacts in the velocity profile. These parameters affect echoes which are used to produce the velocity profiles. The emitting power is related to the strength of the ultrasonic pulses that at are emitted. This power level is only adjustable in three discrete steps (low, medium, or high) and can be set by a drop-down menu in the parameter list. The higher the emitting power, the stronger the reflected echoes will be. The highest emitting power was used in almost all cases for this thesis, since weak echo profiles was a major issue encountered.

A related parameter to the emitting power is the Tgc or the amplification level. This value is adjustable between -40 to 40 decibels and can be set individually for each gate in the measurement domain. There are both manual and automatic methods to set the amplification level. In the automatic mode, the DOP software tries to determine an optimal amplification profile to reduce saturation while amplifying weak regions in the echo profile. The echo profile is similar to the velocity profile and is the magnitude of the received echo strength as a function of distance beyond the tip of the probe. The three manual modes of setting the amplification level are uniform, slope, and custom. In uniform mode, a uniform amplification level is applied to all gates in the measurement domain. This may not be desirable since in general, the echo profile weakens with increasing distance from the probe tip. Thus in the slope method, the user sets an amplification level for the first gate and the last gate and a linearly increasing amplification level is applied

to all gates in between. Finally in the custom mode, the amplification of each gate can be individually set by the user.

The sensitivity parameter determines the lower bound on the received echo strength for which a velocity will be calculated. In cases where the echo strength is very low, the velocity that is computed may be nonphysical and noisy. Thus to avoid computing nonphysical velocities, gates with low echo strength are rejected and simply replaced with a zero value. The sensitivity parameter determines the lower bound of the acceptable echo strength. Higher sensitivity means echoes with lower intensity will be accepted and the computed velocity profile will be more prone to noise. If the fluid is properly seeded with particles and the UDV is receiving strong echoes from all gates, changing the sensitivity parameter will not affect the computed velocity profile even if a very low sensitivity is used. Thus the sensitivity parameter can be used to determine the fidelity of measurements since changing it should not affect the velocity profile.

There are also a few miscellaneous operating parameters. The velocity scale is continuously adjustable between 0.1 and 1 and determines the range of velocity values that will be computed. Setting the value to 1 will allow the UDV to measure velocities up to the maximum measurable velocity as determined by the PRF. A value of 0.1 will limit the maximum computed velocity to be 10% of the maximum measurable velocity and allows higher resolution in the computed velocity over a smaller range of velocity values.

The "Doppler angle" parameter is essentially a post processing scheme that scales the velocity computed by the UDV by a factor of $\frac{1}{\cos(\theta)}$, where θ is the Doppler angle. The Doppler angle is used in situations where the UDV probe is mounted at a known angle to the flow velocity vector, such as in channel or pipe flow, and allows the UDV to display the "true" velocity rather than the velocity component parallel to the UDV probe. If this post-processing feature is not desired or not applicable, the Doppler angle can be set to 0 and the UDV will output the velocity component of the fluid parallel to the probe without any scaling.

2.7. Working Fluid and Seed Particles

Two different working fluids were used for the investigations in this thesis. Although the long term goal is to perform experiments using conducting liquid metals as the working fluid, the experimental setup is first verified with water and a 20% glycerin-water mixture. Regular tap water is a natural choice to test with first for its availability, ease of handling, and ease of disposal. The UDV requires the addition of small plastic beads to the water to act as acoustically reflective particles for the ultrasonic pulses. A sample of copolyamide particles, recommended by the UDV vendor for experiments with water, was purchased. The beads are called Griltex 2A P1 and properties for the beads can be found in Table 2.4.

UDV Copolyamide Particles (Griltex 2A P1)	
Size Distribution	60% 50 μm 40% 80 μm
Published Density (MSDS)	$1.00 \frac{g}{cm^3}$

Table 2.4 – UDV particle properties

Several different concentrations of UDV beads were tested in initial experiments to determine an optimal concentration. Too few particles will result in a lack of echoes from regions of the flow, and the velocity profile generated by the UDV will have "holes" where the velocity cannot be computed. However, too many particles can cause excess scattering of the ultrasonic pulses and also result in poor

echo profiles for the UDV. A very high particle concentration could also begin to affect the dynamics of the flow. A particle concentration of 0.1 grams of particles per 1 liter of water was selected. Appendix B contains a detailed description of how the UDV beads were mixed into the water.

There were two major issues encountered with water as the working fluid for the experiments. It was discovered during experimentation with water that the vortex breakdown bubbles and the flow field in general are very sensitive to perturbations. Vibrations cause by typing on or bumping the table on which the experimental setup was located produced noticeable changes in the flow field observed by the UDV. Even after isolating the setup on a separate table, it was still very difficult to control the experiment due to the sensitivity of the breakdown bubbles and the amount of ambient vibration. This problem was further exacerbated by settling of the UDV beads as described below.

Although the density of the recommended beads is reported to be $1.00 \frac{g}{cm^3}$ (same density as water), it was found during experiments that the UDV beads would settle out of water fairly quickly. This suggests that the UDV beads actually have a slightly higher density than tap water. This would not present a problem in experiments with fast moving flows, since the flow itself would keep the particles well mixed. However, for the experiments performed here, the mean fluid velocity is only on the order of 2-6 mm/s. The time scales for the dynamics of the flow were also very long, necessitating long wait times before transient behavior settled. The combination of poor density matching of the UDV beads and slow fluid velocities

resulted in excessive setting of the UDV beads during experiments. The effect is very noticeable on the UDV velocity profiles, as there is a gradual increase in the number of holes (zero velocity regions) within the velocity profile due to poor echo strength. This required the water/bead mixture to be periodically re-agitated by manually pumping the mixture with a syringe. There was approximately a 1 to 1.5 hour window after agitating the mixture before the velocity profiles became unusable. The transient behavior when switching between different Reynolds numbers usually lasted on the order of 10-20 minutes for the experiments. Thus only one or two data sets could be collected before the experiments had to be stopped in order to re-agitate the solution. The short working window also meant that there was insufficient time for the fluid to reach a quiescent state after re-agitating before experiments had to begin.

Given the problems encountered with using water as the working fluid, a more viscous glycerin-water solution was tested. This inadvertently led to the development of a strategy that solved many of the problems encountered with using water for these experiments. It was conjectured that the higher viscosity of the glycerin-water solution would more readily damp perturbations and make the system less sensitive to external disturbances. Initial results with the glycerin-water solution were promising, as it appeared to have made the system more stable. As an additional benefit, it was also discovered that using the glycerin-water solution also remedied the bead suspension problem. At the time, the only beads that were available for testing were the $1.00\,\frac{g}{cm^3}$ beads used with the water solution.

Since the testing with water revealed that the beads were actually denser than water, a 20% by volume glycerin-water solution was chosen, resulting in a 6% increase in the density of the solution compared to water. After preparing the 20% glycerin-water solution, the UDV beads were added in a similar procedure as before. It was found that approximately a quarter of the UDV beads added to the solution would immediately float to the top of the container. Over the course of further mixing and running initial experiments, the beads that floated in the solution were removed since they clung to the sides of the fluid container or to the rotating disk. However, the remaining beads in the solution did not settling to the bottom and stayed suspended extremely well. Even after sitting several days in a completely quiescent state, there would be no noticeable settling of the UDV beads. This suggests that there is a distribution in the density of the UDV beads being used and a 20% glycerin-water solution exactly matches the density of a majority of these beads. Thus, after the glycerin-water solution is prepared and the lighter beads in the distribution have been removed, the remaining solution with the suspended UDV beads can be used for days without having to re-agitate. The initial amount of beads added to the solution can be adjusted to ensure sufficient quantities of the beads remain in solution after skimming off the lighter beads. This allows the experimental setup to be run continuously without interruption and allows startups from a quiescent flow field.

By switching to a 20% glycerin-water solution, many of the problems encountered with bead setting and very slow dynamics of the flow field are solved. If future experiments are to be performed with solutions with even higher glycerin

content, the author suggests the following strategy. First, purchase beads or particles of approximately the right density for the desired glycerin-water composition. The composition of the glycerin-water solution can then be fine tuned to exactly match the density of the beads by experimentation to achieve perfect suspension within the solution. This strategy would actually benefit from loose tolerances on the density distribution of the beads since this would make density matching with the glycerin-water solution easier to achieve.

Properties for water and the glycerin-water solution can be found in Table 2.5. The density and kinematic viscosity of the glycerin-water solution are pulled from a curve-fit performed by (Cheng 2008). The acoustic viscosity is calculated as the weighted averaged by mass of the glycerin-water solution based on published values of the acoustic viscosity for pure water and pure glycerin.

	Kinematic Viscosity $\left[\frac{m^2}{s}\right]$	**Density** $\left[\frac{kg}{m^3}\right]$	**Acoustic Velocity** $\left[\frac{m}{s}\right]$
Tap Water	1.0×10^{-6}	998	1480
20% Glycerin-Water by Volume(23°C)	1.72×10^{-6}	1060	1582

Table 2.5 – Properties of working fluids

Chapter 3

Methods

This chapter presents the experimental and numerical methods used. Section 3.1 discusses how the operating parameters for the UDV are selected and how the experimental system works. The sources of experimental error are identified and discussed. Section 3.2 cites the two existing three-dimensional, time-dependent simulation codes that were used to model the rotating lid-driven cylinder problem for comparison with experimental results. Since development of the numerical methods was not the focus of this thesis, only input parameters and meshes for the numerical methods are presented.

3.1. Experimental Methods

3.1.1. Selection of UDV Operating Parameters

Selection of the operating parameters for the UDV play an important role in the quality of the velocity profiles obtained. A description of the parameters can be found in 2.6. This section focuses on the strategy used for selecting the parameters based on the experiments run. The "assisted mode" of the UDOP software was used initially for a set of experiments with water as the working fluid. In "assisted mode", the user selects the values for a few key parameters and the other parameters are computed automatically by the UDOP software. After gaining a better understanding of how the UDV works, the parameters were fine tuned for the set of experiments with the glycerin-water solution. Both are shown in Table 3.1.

Parameter	Water	20% Glycerin-Water By volume (23°C)
US Frequency $[kHz]$	4000	4000
Number of Gates	300-500 depending on desired measurement domain	300-500 depending on desired measurement domain
First Gate Depth $[mm]$	5	5
PRF $[\mu s]$	6273	7001 – 15001 depending on maximum anticipated velocity
Resolution $[mm]$	0.247	0.264

Velocity Scale Factor	0.5-1.0 depending on maximum anticipated velocity	0.5-1.0 depending on maximum anticipated velocity
Doppler Angle	0°	0°
Burst Length	4	4
Emitting Power	Medium	High
Emissions/Profile	150	150
Sound Speed $\left[\frac{m}{s}\right]$	1480	1582
Sensitivity	Low	Medium
Tgc [dB]	40	40
Sampling Volume $[mm]$	0.888	0.949

Table 3.1 – UDV parameters used for different working fluids

Parameters such as the burst length, sound speed, and ultrasonic frequency are set either by default, or directly associated with the working fluid and UDV probe. Since high spatial resolution was desired, the sample volume size was set to the smallest available size based on burst length and sound speed. There are only 6 discrete values of the sample volume size available in the form of a drop down menu. As the value is lowered, a warning will state that the lowest sampling volume has been reached. It is possible to reach even lower sampling volume sizes by decreasing the burst length. However, this was not investigated, as lower burst

length values seemed to increase the amount of noise in the velocity profile. The Doppler angle scaling feature was not used, so this value was set to 0° for all experiments.

The spatial resolution was also set to be the smallest value (providing the highest resolution) that would still allow the UDV to measure the entire fluid domain. Once these values were set, the other parameters were usually adjusted on a case by case basis to reduce the noise level, match the maximum anticipated velocity, and measure the entire flow domain.

The measurement domain was determined by the depth of the first gate and the number of gates being used. In general, the measurement domain was set to entirely encompass the flow domain with some extra gates that would extend past the container walls. There is no harm in keeping these extra gates, since the boundaries of the flow domain can always be determined by looking at the velocity profile or echo profile. The depth of the first gate was set to 5 mm for all experiments performed. This avoided the ringing effect (as described in Section 2.6) that is present in the first few millimeters past the tip of the probe and coincides approximately with the beginning of the flow domain, since the ultrasonic pulses must first travel through the container walls. The choice of the number of gates depended on the depth of the flow domain. Sample calculations for the depth of the last gate are shown in (3.1) to (3.2)

$$x_{last} = x_{first} + \Delta x \times (N - 1) \tag{3.1}$$

$$x_{last} = 5\ mm + 0.264 \times (500 - 1) = 136.7\ mm, \tag{3.2}$$

where x_{last} is the depth of the last gate, x_{first} is the depth of the first gate, Δx is the resolution, and N is the total number of gates. Thus if the end of the fluid domain is anticipated to be around 130 mm past the UDV probe, 500 or even 550 gates could be used.

Next, the velocity magnitude that is computed and displayed was determined by a combination of two parameters: the PRF and the velocity scale. Note that in the parameter menu, the PRF parameter is actually misnamed. The value input there is actually the pulse repetition period in μs, rather than the pulse repetition frequency (PRF). The PRF determines the maximum velocity that the UDV is physically capable of measuring, V_{max}, according (2.11) repeated here with sample calculations using the values for the glycerin-water solution:

$$V_{max} = \frac{F_{PRF} \cdot C}{4 \cdot f_e}$$

$$V_{max} = \frac{\frac{1}{15001 \times 10^{-6}} \cdot 1480}{4 \cdot 4 \times 10^{6}} = 0.00617 \frac{m}{s} = 6.2 \frac{mm}{s}; \tag{3.3}$$

Here F_{PRF} is the PRF frequency, C is the sound speed, and f_e is the emitting frequency. Thus in the glycerin-water solution with a pulse repetition period of 15001 μs, the UDV is physically capable of measuring a maximum fluid magnitude of 6.2 mm/s. However, V_{max} is not necessarily the maximum velocity magnitude that is being computed and displayed. The maximum computed and displayed velocity

magnitude, V_{disp}, is determined by scaling V_{max} by the velocity scale factor, V_{scale}, which can range from 0.1 to 1.0.

$$V_{disp} = V_{scale} \times V_{max}. \quad (3.4)$$

The velocity scale factor is useful because the UDV has a limited resolution in the computed velocity values and can only calculate 256 different velocity values. For example, it might be desirable to use a pulse repetition frequency of 15001 μs (which is able to measure a flow up to 6.2 mm/s) for a flow with a maximum velocity of only 2 mm/s. By using a velocity scaling factor of approximately 0.4, the resolution of the computed velocity values can be concentrated in the desired region so that all 256 available velocity values are placed between $\left[-2\frac{mm}{s}, 2\frac{mm}{s}\right]$.

The PRF also plays a role in the amount of noise in the velocity profile and the temporal resolution. Generally, increasing the PRF will reduce the amount of noise or artifacts present in the velocity profile. However, a longer PRF also leads to more averaging of the flow field and may be detrimental when trying to measure flows with fast dynamics or periodicity. The overall temporal resolution of the UDV is determined by the PRF and the number of emissions that are averaged per profile. The overall acquisition time for a single velocity profile is given in the sample calculations below, where $\Delta t_{profile}$ is the acquisition time for a single profile, $N_{emissions}$ is the number of emissions per profile, and $(Computation\ Time)$ is the amount of time necessary to perform the computations to generate the velocity profile and is a physical characteristic of the UDV device.

$$\Delta t_{profile} = \frac{1}{F_{PRF}} \times N_{emissions} + (Computation\ Time) \tag{3.5}$$

$$\Delta t_{profile} = 15001\ \mu s \times 150 + (250{,}000\ \mu s) = 2.5\ s. \tag{3.6}$$

As the above equations demonstrate, the number of emissions per profile plays a direct role in temporal resolution. Increasing the number of emissions per profile produces cleaner velocity profiles, but lowers the temporal resolution since more averaging is introduced. In addition to the brief description and sample calculations above, Table 3.2 describes the appropriate strategy to handle some of the common problems encountered when using the UDV.

Problem	Strategy
Measurement domain does not cover the flow domain.	1. Increase the number of gates. *Or, if maximum number of gates is already being used (1000):* 2. Increase the gate spacing to make each gate span a longer region.
Maximum fluid velocity exceeds V_{disp} and the velocity signal is aliasing.	1. Increase the velocity scale. *If $V_{scale} = 1.0$ already:* 2. Decrease the pulse repetition period (increase PRF).
Maximum fluid velocity is well below V_{disp} and more resolution is desired in the velocity values.	1. Decrease the velocity scale. *If $V_{scale} = 0.1$ already:* 2. Increase the pulse repetition period (decrease PRF).
Weak echo profile and many "holes" (region of zero velocity) in the velocity profile.	1. Increase the emitting power. 2. Increase the amplification level (Tgc). 3. Increase the amount of beads in the working fluid. 4. Increase the sensitivity.
There are many artifacts or noise in the velocity profile, often appearing as sharp spikes in the velocity profile.	1. Decrease the sensitivity. 2. Increase the number of emissions per profile. 3. Increase the pulse repetition period (decrease PRF).
There is transience that is occurring on a time scale smaller than the current acquisition time.	1. Decrease the number of emissions per profile. 2. Decrease the pulse repetition period (increase PRF).

Table 3.2 – Strategies for common problems encountered when using UDV

3.1.2. Using the Experimental System

Now that construction of the experimental assembly (Chapter 2) and Ultrasonic Doppler Velocimetry has been discussed, a brief overview of the entire experimental system is presented. Figure 1.1 shows a full schematic of the experimental system. A personal computer runs software for both the DOP3010 and the cRIO motor control system and handles all data collection and controls. The cRIO motor control system performs velocity control on a motor that rotates the lid of the experimental setup. The DOP3010 connects to a UDV probe, which is mounted to the experimental setup and produces velocity profiles via Ultrasonic Doppler Velocimetry.

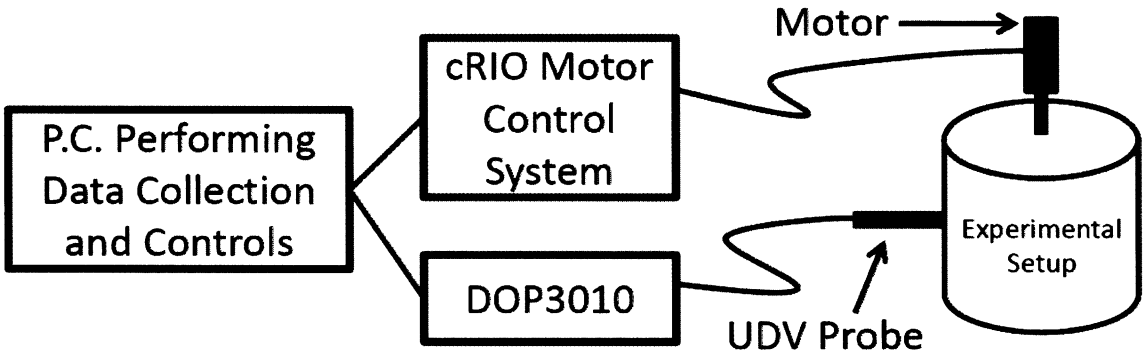

Figure 3.1 – Schematic of the expermental system

The experimental setup consists of three main pieces: the fluid container, the motor/lid assembly, and the probe mounts. The reader is referred to the assembly drawing of part 37 in Appendix A for a picture. The fluid container is a cylindrical container 4 inches in inner-diameter with an open top and posts for securing probe

mounts. The motor/lid assembly consists of a rotating acrylic disk and a motor that rotates the disk. The motor/lid assembly sits on top of the fluid container, and the height of the rotating disk can be adjusted to achieve different aspect ratios (Equation (1.1)). Finally, there are two types of probe mounts that attach to the fluid container and mount probes either to the bottom or the sides of the fluid container. Figure 3.2 shows a cross-sectional view of the experimental setup. Fluid contained within the dotted lines in Figure 3.2 constitutes the experimental domain. The aspect ratio of this cylinder can be adjusted by changing the length of the shaft connecting the rotating lid (Appendix A, part 5), or by adjusting the height of the aluminum standoffs (part 25). The vertical location of the rotating lid can also be fine tuned at the shaft coupler.

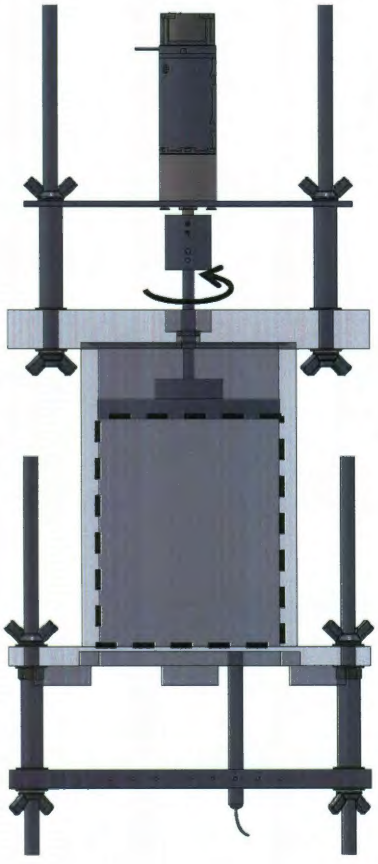

Figure 3.2 – Side view of expermental setup with expermental domain marked by dotted line

To setup the experiment, the cylindrical fluid container is filled to a height 0.25 inches above the desired aspect ratio of the experimental domain. The motor/lid assembly is then lowered onto the fluid container. The extra working fluid ensures that the experimental domain will be completely filled. Because of the extra working fluid, there is actually a layer of fluid that sits on top of the rotating lid during experiments. Detailed instructions in Appendix B describe how the motor/lid assembly is lowered into the fluid to avoid trapping air bubbles. Given the small gap size between the walls of the cylinder and the rotating lid, and the viscous effects of the fluid, there should be very little convective fluid exchange between the experimental domain and the fluid sitting on top of the rotating lid.

Mounting of the UDV probes to the experimental setup is fairly straightforward for the bottom probe mount. The probe is inserted into the device (part 8) at the desired offset point. A pea-sized drop of ultrasound transmission gel (Aquasonic 100) is placed on the tip of the probe. The tip of the probe is then pressed onto the bottom of the fluid container. The drop of ultrasonic gel should compress outward and surround the probe, completely enclosing the interface between the probe and the acrylic. The set screw can then be tightened to hold the probe in place. Here a nylon #6-32 screw is used to avoid damaging the UDV probe.

For all experiments presented in this thesis, probes mounted to the sides of the fluid container were mounted perpendicular to one of the flat surfaces created by the bevels. Unlike the bottom probe, where the geometry of the probe mount

automatically holds the UDV in the desired configuration, the side probe mount requires a more complex alignment procedure.

The vertical height of the probe support plate is determined by the desired height of the UDV probe. From there, the two sliding/rotating joints are adjusted so that the probe is held perpendicular to one of the beveled surfaces. Given the small circular cross-sectional area of the probe, it is difficult to tell whether the probe is actually perpendicular to a flat surface, especially when the ultrasonic transmission gel is used. To make this alignment process easier and more consistent, a probe alignment block was fabricated out of acrylic (Appendix A, part 38). The probe is inserted into the block and the block is held against the flat surface to which the probe is to be mounted. The rotating/sliding joints of the probe mount can then be adjusted to hold the probe in this configuration. Once all degrees of freedom have been locked, the probe is removed from the clamp, the ultrasonic gel is applied to the probe, and the probe is placed back in the desired configuration. Figure 3.3 shows a UDV probe mounted to one of the side bevels; the probe mount is to the right and is not pictured.

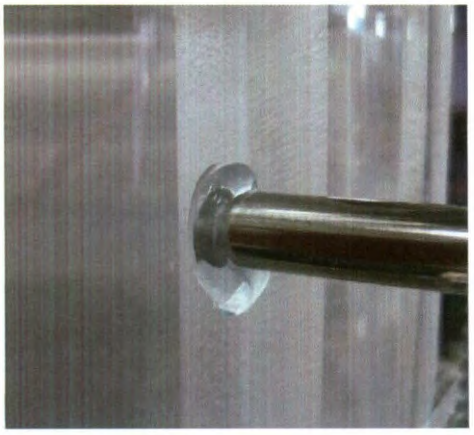

Figure 3.3 – UDV probe mounted to side bevel with ultrasonic transmission gel

Once the UDV probe has been mounted in the desired position, the DOP3010 and the cRIO motor controller are connected. The data acquisition and controls software is initiated on the P.C. and experiments begin. Instructions for starting up the data acquisition and controls software can be found in Appendix B.

3.1.3. Sources of Experimental Error

A number of factors contribute to the potential sources of experimental error. First, measurements of the diameter for the fluid container (part 1) and the rotating disk (part 6) are presented to characterize the size of the gap between these two parts. Two disks were machined, one corresponding to an aspect ratio of 2.5 for the fluid domain (as diagramed in part 6) and another with a longer shaft corresponding to an aspect ratio of 1.25. Digital calipers accurate to within 0.0005 inches were used to take ten measurements on the inner diameter of the fluid container and the outer diameter of the rotating disks at different points. The maximum and minimum measurements are presented in Table 3.3.

	Minimum Diameter (Inches)	**Maximum Diameter (Inches)**	**Maximum Gap Size (Inches)**
Fluid Container (part 1)	4.0110	4.0370	--
Rotating Disk ($\gamma = 2.5$)	3.9895	3.9915	0.0475
Rotating Disk ($\gamma = 1.25$)	3.9845	3.9860	0.0525

Table 3.3 – Gap size between rotating disk and fluid container

The eccentricity and wobble of the outer edge of the rotating disk due to improper alignment are also potential sources of error since these introduce

undesirable perturbations to the flow field. These measurements were made by clamping the rotating shaft of each disk into a collet chuck on the lathe. A feeler gauge was then used to take measurements accurate to 0.0005 inches as the disk was rotated by hand. These measurements are tabulated in Table 3.4.

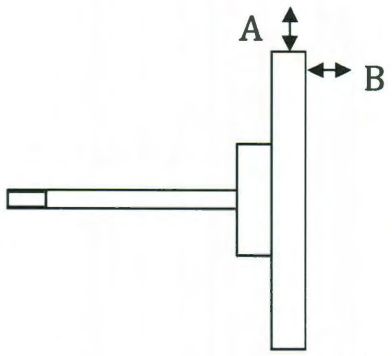

	Measurement A (Inches)	Measurement B (Inches)
Rotating Disk ($\gamma = 2.5$)	±0.003	±0.0015
Rotating Disk ($\gamma = 1.25$)	±0.0015	±0.0035

Table 3.4 – Measurements of eccentricity and wobble of rotating disks

Aside from geometrical errors, variation in the velocity of the motor was also of concern. Testing of the motor controller revealed that during steady-state operation, the average motor velocity fluctuated by approximately ±0.25 RPMs. Of greater concern however, were very high frequency oscillations in the computed velocity of the motor that were actually quite large. An example of this can be seen

in Figure 3.4 for a velocity set-point of 300 RPM. Table 3.5 shows the average, minimum, and maximum velocity over a 1 second interval. As can be seen from the table, the motor controller is able to keep the average motor velocity at the correct value. However, the high frequency oscillations in the velocity can deviate up to 20% from the set-point. A variety of tests were performed in order to identify the source of the high frequency oscillations. It was found that the high frequency oscillations are insensitive to the motor controller gains or the controller loop rates. The oscillations are also unaffected by physically loading the output shaft of the motor. Mechanical noise from the gearbox was ruled out as a possible cause because of the high frequency of the oscillations and the fact that the amplitude of the oscillations changed with the set-point. Electrical noise was ruled out by running the motor with several different power supplies. Instabilities in the motor controller were also ruled out since the oscillations were insensitive to the controller gains and loop rates. Based on observations of the motor during testing and the high frequency at which the oscillations were occurring, the oscillations in the computed velocity seemed to be non-physical.

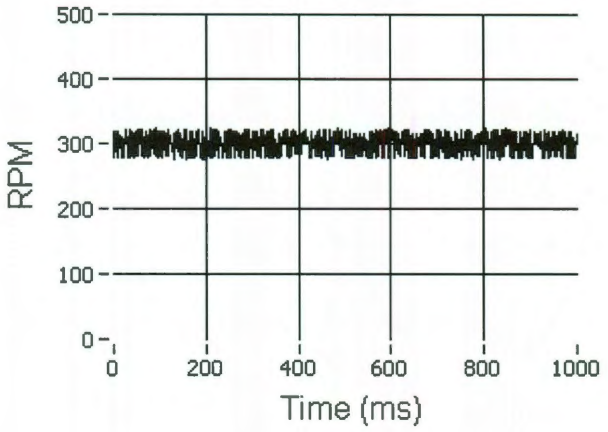

Figure 3.4 – Plot of motor velocities for set-point of 300 RPM

Velocity Setpoint (RPM)	Average (RPM)	Min (RPM)	Max (RPM)	Deviation
50	50.2	41.6	60.4	-17% +21%
100	100.3	89.2	113.0	-11% +13%
150	150.2	134.5	167.0	-10% +11%
200	200.1	180.9	222.5	-10% +11%
250	250.3	227.2	276.5	-9% +11%
300	300.2	272.6	331.7	-9% +11%

Table 3.5 – Average, minimum, and maximum motor velocity for various velocity set-points

Based on the above evidence, the author believes that the motor controller is keeping the rotation rate steady and at the correct velocity. The high frequency oscillations observed in the computed velocity of the motor are most likely the result of an electrical artifact in how the velocity is actually computed and reported by the FPGA VI (described in Section 2.5). Unlike the velocity being computed by the PID control loop, which calculates an "average" velocity once per loop cycle, the velocity that is reported by the FGPA VI is computed based on the amount of elapsed time between two encoder ticks. Although this provides the best estimate of the "instantaneous" velocity of the motor, it is contingent upon very accurate spacing of the encoder ticks. A very small phase shift in the encoder channels will cause discrepancies in the distance between encoder ticks and lead to the high frequency oscillations in the computed velocity. This is illustrated in Figure 3.5.

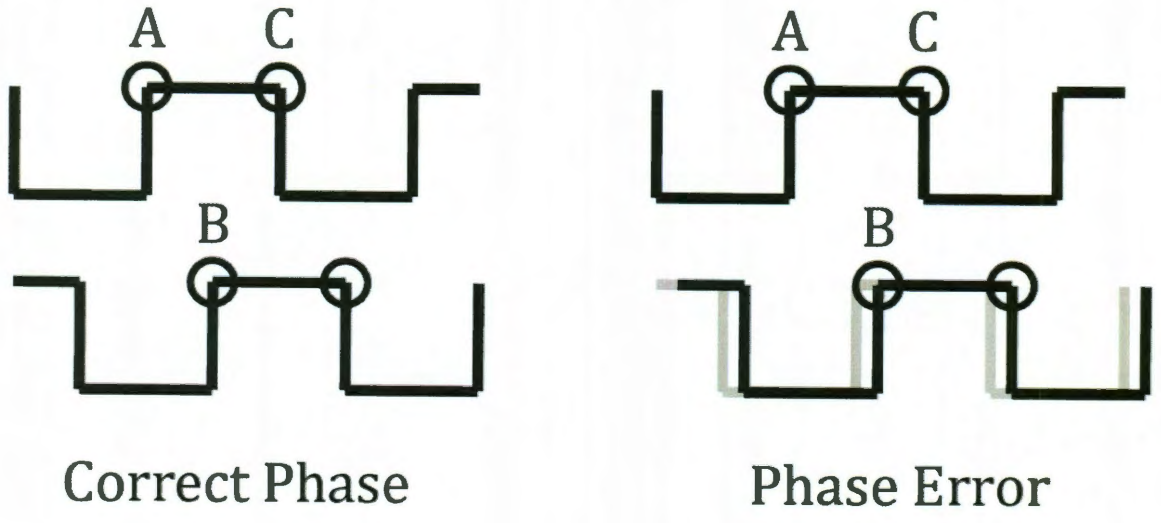

Figure 3.5 – Phase error causing oscillations in computed velocity

To investigate this error, assume that the encoder is rotating at a constant velocity. In the encoder with the correct phase, the distance or amount of time elapsed between encoder ticks A-B and B-C are exactly the same. Thus the FPGA VI would report a constant velocity. However, even if there is just a 10% error in the perceived location of the encoder ticks between the two channels, this will cause the time elapsed between ticks A-B to be 10% longer than the correct value and the time elapsed between B-C will be 10% shorter than the correct value. Although the encoder is rotating at a constant velocity, a small phase error will cause the FPGA VI to report velocities that are oscillating between ±10% of the correct value at a very high frequency. This is exactly the type of behavior exhibited by the system. However, this theory is still very difficult to verify. Without a method of verifying the instantaneous velocity at the output shaft of the motor, only physical intuition and the above explanation are offered as evidence that the motor is indeed turning at a constant velocity and that the observed oscillations are an artifact of the electronics. One possible way to reduce the effect of mechanical and electrical noise on the velocity of the motor is to attach a large inertial mass to the output of the gearbox as in (Stevens *et al.* 1999).

Another potential source of experimental error is variations in the viscosity of the glycerin-water solution due to temperature changes or compositional inaccuracy. Figure 3.6 shows a plot of the viscosity of a glycerin-water solution as composition and temperature is varied. This is based on a curve fit performed by (Cheng 2008). The plot demonstrates that the viscosity of the glycerin-water solution is quite sensitive to both temperature variations and compositional

changes. To characterize the degree of temperature variation present, the ambient air temperature of the room where the experimental setup was located was measured over the course of 2 hours every 10 minutes. It was found that the ambient air temperature was 23°C ± 0.1°C. Due to the extremely low speeds present in the fluid flow, viscous heating would be negligible and the experimental setup should be isothermal at the ambient room temperature. The glycerin-water solution was prepared by volume in a graduated cylinder and the compositional variation is estimated to be on the order of 1-2%.

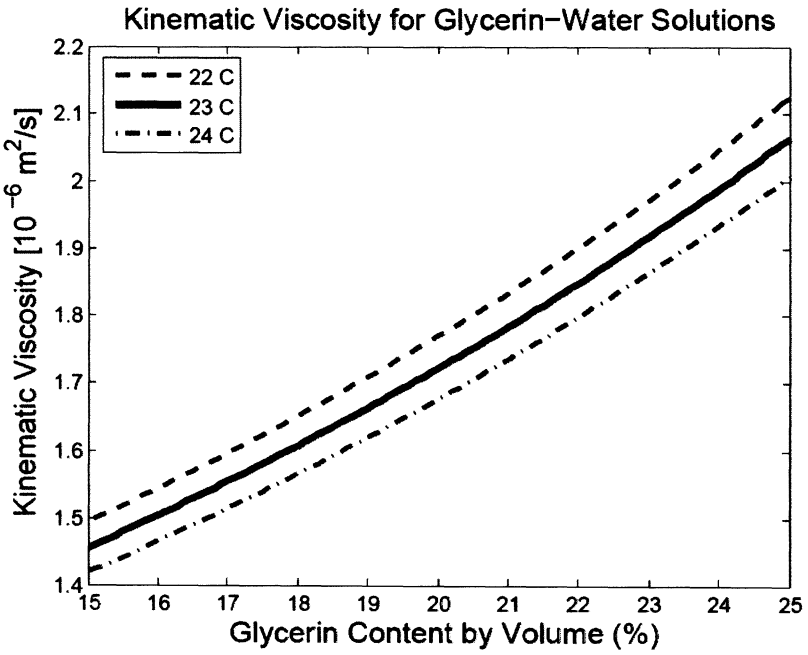

Figure 3.6 – Kinematic viscosity of glycerin-water solution as a function of temperature and composition

3.2. Numerical Simulations

Existing codes used to perform 3D simulations of the rotating lid-driven cylinder are presented. Numerical simulations were originally performed to generate theoretical flow fields that could be compared to experimental measurements obtained with the UDV. Derivation, development, and implementation of a computational fluid dynamics code are not the focus of this thesis. However, some convergence difficulties specific to the rotating lid-driven cylinder problem were encountered in the process of using a three-dimensional, spectral element CFD code developed in the research group by Kenneth E. Davis (Davis 2011). Thus, simulations on a second, open-source CFD code that has been well documented and benchmarked were also used for comparison (Blackburn and Sherwin 2004). In an effort to document the difficulties encountered, a summary of all numerical simulations, even those not used for comparison with experimental results, will be presented in the Chapter 4 and Appendix D.

3.2.1. Problem Statement

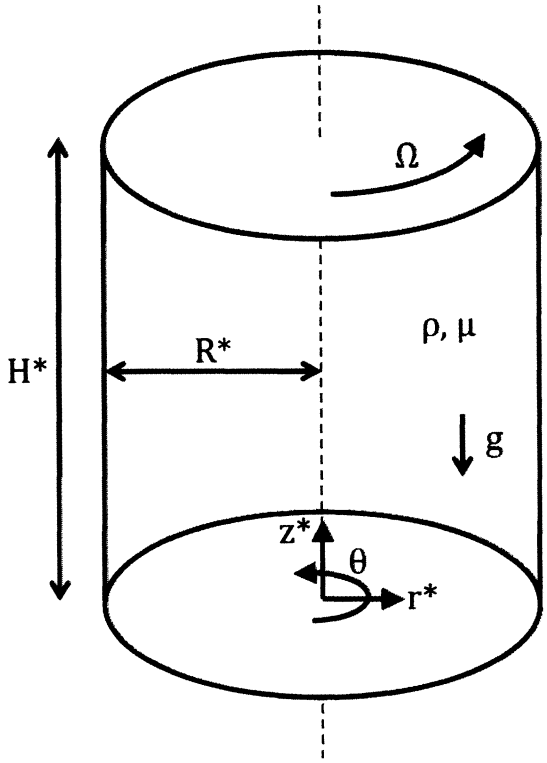

Figure 3.7 – Model of rotating lid-driven cylinder

Figure 3.7 shows a model for the rotating lid-driven cylinder problem. An incompressible fluid with uniform, constant properties completely fills an un-deforming cylinder. The cylinder has height H^*, radius R^*, and the top of the cylinder rotates at a constant angular velocity Ω. The governing equations for an incompressible, Newtonian fluid with constant properties are:

$$\nabla^* \cdot \boldsymbol{V}^* = 0 \tag{3.7}$$

$$\rho\left[\frac{\partial \boldsymbol{V}^*}{\partial t^*} + (\boldsymbol{V}^* \cdot \nabla^*)\boldsymbol{V}^*\right] = -\nabla^* P^* + \mu \nabla^{*2} \boldsymbol{V}^* - \rho g \hat{\boldsymbol{z}} \tag{3.8}$$

Where $\boldsymbol{V}^*$ is the dimensional velocity vector, P^* is the dimensional pressure, ρ is the density, μ is the dynamic viscosity, g is the acceleration due to gravity, and $\hat{\boldsymbol{z}}$ is the unit vector in the axial direction of the cylinder. The reader is referred to chapters 4 and 9 of (Cengel and Cimbala 2009) for the details in deriving of the above governing equations. Assuming an incompressible, constant density fluid and a constant gravitational acceleration, the pressure can be redefined to incorporate the hydrostatic effect of gravity and eliminate that term from the equation:

$$\hat{P}^* = P^* + \rho g z \tag{3.9}$$

$$\rho\left[\frac{\partial \boldsymbol{V}^*}{\partial t^*} + (\boldsymbol{V}^* \cdot \nabla^*)\boldsymbol{V}^*\right] = -\nabla^* \hat{P}^* + \mu \nabla^{*2} \boldsymbol{V}^*. \tag{3.10}$$

From here we define the following characteristic parameters, where asterisks indicate dimensional quantities:

Characteristic Parameters	
Length	R^*
Velocity	ΩR^*
Frequency	Ω
Pressure	$\rho(\Omega R^*)^2$

Using the above characteristic parameters, the following non-dimensional variables are defined:

$$\nabla = R^* \nabla^* \quad \rightarrow \quad \nabla^* = \frac{1}{R^*}\nabla \tag{3.11}$$

$$t = \Omega t^* \quad \rightarrow \quad t^* = \frac{1}{\Omega} t \tag{3.12}$$

$$\boldsymbol{u} = \frac{\boldsymbol{V}^*}{\Omega R^*} \quad \rightarrow \quad \boldsymbol{V}^* = \Omega R^* \boldsymbol{u} \tag{3.13}$$

$$P = \frac{\hat{P}^*}{\rho(\Omega R^*)^2} \quad \rightarrow \quad \hat{P}^* = \rho(\Omega R^*)^2 P, \tag{3.14}$$

where ∇ is the non-dimensional del operator and t, $\boldsymbol{u}$, and P are the non-dimensional variables for time, velocity, and pressure respectively. Plugging in the above non-dimensional variables into the dimensional continuity equation (3.7) yields:

$$\frac{1}{R^*} \nabla \cdot (\Omega R^* \boldsymbol{u}) = 0$$

$$\frac{\Omega R^*}{R^*} (\nabla \cdot \boldsymbol{u}) = 0$$

$$\nabla \cdot \boldsymbol{u} = 0. \tag{3.15}$$

Likewise the dimensional momentum equation (3.10) becomes:

$$\rho \left[\frac{\partial(\Omega R^* \boldsymbol{u})}{\partial\left(\frac{1}{\Omega} t\right)} + \left((\Omega R^* \boldsymbol{u}) \cdot \frac{1}{R^*} \nabla \right) (\Omega R^* \boldsymbol{u}) \right] = -\frac{1}{R^*} \nabla(\rho(\Omega R^*)^2 P) + \mu \left(\frac{1}{R^*}\right)^2 \nabla^2 (\Omega R^* \boldsymbol{u})$$

$$\rho \Omega^2 R^* \frac{\partial \boldsymbol{u}}{\partial t} + \rho \Omega^2 R^* (\boldsymbol{u} \cdot \nabla) \boldsymbol{u} = -\rho \Omega^2 R^* \nabla P + \frac{\mu \Omega}{R^*} \nabla^2 \boldsymbol{u}$$

$$\frac{\partial \boldsymbol{u}}{\partial t} + (\boldsymbol{u} \cdot \nabla) \boldsymbol{u} = -\nabla P + \frac{\mu}{\rho \Omega R^{*2}} \nabla^2 \boldsymbol{u} \tag{3.16}$$

Next we define two non-dimensional parameters reproduced from (1.1) and (1.2):

$$\gamma = \frac{H^*}{R^*}$$

$$Re = \frac{\rho \Omega R^*}{\mu} = \frac{\Omega R^*}{\nu}.$$

Here γ is the aspect ratio, Re is the Reynolds number, and ν is the kinematic viscosity. Plugging the definition of Re into (3.16) we arrive at:

$$\frac{\partial \boldsymbol{u}}{\partial t} + (\boldsymbol{u} \cdot \nabla)\boldsymbol{u} = -\nabla P + \frac{1}{Re}\nabla^2 \boldsymbol{u}. \tag{3.17}$$

Next we define the boundary conditions in non-dimensional, cylindrical coordinates, noting that: r, θ, and z are the non-dimensional radial, azimuthal, and axial coordinates (as shown Figure 3.7) and $\boldsymbol{u} = \{u, v, w\}$ where u, v, and w are the radial, azimuthal, and axial velocities of the cylinder respectively. For the rotating lid-driven cylinder problem, we have no-slip on all surfaces with the walls and bottom of the cylinder stationary, and a constant rotation at the lid of the cylinder:

$$\left\{ u = v = w = 0 : \begin{array}{c} r = 1 \\ 0 \le \theta < 2\pi \\ 0 \le z \le \gamma \end{array} \right\} \tag{3.18}$$

$$\left\{ u = v = w = 0 : \begin{array}{c} 0 \le r \le 1 \\ 0 \le \theta < 2\pi \\ z = 0 \end{array} \right\} \tag{3.19}$$

$$\left\{ u = w = 0, v = r : \begin{array}{c} 0 \le r < 1 \\ 0 \le \theta < 2\pi \\ z = \gamma \end{array} \right\} \tag{3.20}$$

The non-dimensional parameter for the aspect ratio, γ, is used to specify the non-dimensional coordinate for the top of the cylinder, since all length coordinates have been scaled by the characteristic length R^*. The characteristic velocity scale, ΩR^*, is also used in the definition of the boundary condition for the rotating lid to make all terms non-dimensional.

Thus we arrive at the non-dimensional governing equations for the rotating lid-driven cylinder problem with boundary conditions in equations: (3.15), (3.17), and (3.18) through (3.20). Note that Re and γ are the only two parameters in the governing equations. This means that any experimental or numerical result can be directly compared as long as the Re and γ are the same for both systems. The unknowns are three velocity components (u, v, w) and a scalar pressure field P.

Two existing 3D, time-dependent spectral element CFD codes were used to solve the above problem for Reynolds numbers in the range of 0 to 3000 for an aspect ratio of $\gamma = 2.5$. At this aspect ratio the flow is expected to be steady and axisymmetric at low Reynolds numbers. At approximately $Re = 2700$ the flow transitions to a periodic, axisymmetric, and pulsating instability. This result has been supported by several published works, both experimental and numerical, with the results summarized in Table 3.6.

Author	Analysis Type	Re_{cr}	ω_{cr}
(Gelfgat *et al.* 1996) (Gelfgat *et al.* 2001)	Linear Stability Analysis	2706	0.172
(Escudier 1984)	Experimental	~2670	--
(Stevens *et al.* 1999)	Experimental	~2700	0.174
(Lopez and Perry 1992)	Numerical	~2650	0.175
(Sørensen *et al.* 2006)	Experimental	2600	0.201

Table 3.6 – Predicted periodic, axisymmetric instability for $\gamma = 2.5$

Note that ω_{cr} is the non-dimensional natural frequency of the critical instability (in this case the axisymmetric instability). It is computed as

$$\omega_{cr} = \frac{2\pi f}{\Omega}, \tag{3.21}$$

where f is the frequency of the instability in hertz, and Ω is the lid angular velocity.

The goal here is to compute the flow field for both the base-flow and the periodic flow for this $\gamma = 2.5$ case and compare the results to experimental measurements obtained with UDV. It is hoped that UDV measurements can identify both the steady base-flow as well as the periodic, axisymmetric flow above the critical Reynolds number.

3.2.2. Three-Dimensional, Time-Dependent Spectral Element Code

A three-dimensional, time-dependent spectral element CFD code (abbreviated SEMG) that was developed in the research group by Kenneth E. Davis (Davis 2011) was used initially to perform numerical simulations of the above problem. A structured cylindrical mesh generator was used to match the true dimensions and aspect ratio of the experimental setup. All material properties were input in a consistent unit system (metric). The code was run in cylindrical coordinates so that the boundary conditions could be applied exactly. Due to memory constraints in the version used, the maximum number of elements was limited to approximately 4000 with 3rd and 1st order interpolation on velocities and pressure, respectively. Table 3.7 gives a summary of the run parameters used with SEMG. The flow was solved in cylindrical coordinates with 3rd order interpolation on velocities and 1st order on pressures. Newton-Raphson and GMRES were used as the non-linear and linear solvers, respectively. For transient runs, 3rd order backward differentiation was recommended by the author of SEMG and used for all transient simulations. Note that the material properties, fluid domain (mesh), and boundary conditions are all input in dimensional form. The code then uses scaling parameters provided by the user to scale all terms in the governing equations to be of similar order and tries to maintain a well-conditioned system. Also note that although the flow is predicted to be axisymmetric in all Reynolds numbers simulated, a fully 3D simulation was performed in order to verify the axisymmetric assumption. The 3D simulation also simplifies the post processing for comparisons with UDV measurements.

SEMG Simulation Parameters	
Coordinate System	Cylindrical
Unknowns	3 Velocities and Pressure
Velocity Interpolation Order	3
Pressure Interpolation Order	1
Nonlinear Solver	Newton Raphson
Linear Solver	GMRES
Pre-conditioners	Both diagonal and Incomplete LU factorization with zero fill (ilu0) were tested
Time-stepping Method	Backward differentiation 3rd order
System Tolerance (non-dimensional)	Varied between 10^{-6} *to* 10^{-8} as reported in results
Gravity and Buoyancy Approximations	Off
Fluid Properties (assuming water as working fluid)	Assumed Constant: $\rho = 1000\,\frac{kg}{m^3}$ $\mu = 0.001\,\frac{Ns}{m^2}$
Dimensions of Cylinder	$R^* = 0.0508\,m$ $H^* = 0.127\,m$
Scaling Parameters	$length \sim R^*$ $velocity \sim \Omega R^*$ $pressure \sim \rho(\Omega R^*)^2$ $time \sim \frac{R^*}{v}$
Boundary Condition	$v = \Omega r, u = w = 0\ (Lid)$

Table 3.7 – Input parameters for SEMG simulations

When convergence issues with the SEMG code were first experienced, it was initially thought that mesh-refinement was the culprit. Thus a number of different meshes were tested on this code. The different meshes used are presented and results are provided in Appendix D. Although none of the numerical simulations performed with SEMG were used for comparison with the experimental results due to convergence issues, they are still documented here for future work.

As noted previously, all input parameters for SEMG are dimensional and match the actual experimental setup. The radius R^* and height H^* of the cylinder to be meshed are set equal to the dimensions of the experimental setup in metric units (consistent with material properties). The structured mesh generator evenly distributes points in the r and z directions with the option of including boundary layers on surfaces or the center of the cylinder. Uniform wedges in the θ direction are then generated to form the cylinder. $Nr, N\theta$, and Nz are the total number of elements in the r, θ, and z directions. Boundary layers are defined by setting the number of elements in the layer, the size of the initial boundary layer element, and the geometric growth ratio between boundary layer elements. The size of the Nth boundary layer element is defined as:

$$\Delta z_N = \Delta z_0 \times GR^{N-1}, \tag{3.22}$$

where Δz_0 denotes the size of the first boundary layer element in the z direction and GR is the geometric growth ratio. An equivalent boundary layer option is available in the radial direction, where Δr_0 is the size of the first boundary layer element in the r direction. Non-boundary layer elements are then evenly distributed in the

remainder of the domain. Parameters for all meshes used are summarized in Table 3.8.

$\gamma = 2.5, R^* = [0, 0.0508], H^* = [0, 0.127], \theta = [0, 2\pi]$ **Boundary layers are included on:** **outer surface of cylinder (in r) and lid of cylinder (in z)**						
$Nr \times N\theta \times Nz$	BL_r	Δr_0	GR_r	BL_z	Δz_0	GR_z
$12 \times 20 \times 12$	3	0.00254	1.2	3	0.00635	1.2
$15 \times 20 \times 15$	3	0.002	1.2	3	0.005	1.2
$8 \times 12 \times 20$	3	0.0035	1.2	4	0.00254	1.2
$12 \times 10 \times 30$	3	0.002	1.2	5	0.0017	1.2
$10 \times 10 \times 25$	3	0.0035	1.2	4*	0.0025	1.2
$12 \times 10 \times 25$	3*	0.002	1.2	3*	0.002	1.2

Table 3.8 – Mesh parameters for $\gamma = 2.5$ cylinder. BL denotes the number of boundary layer elements. * denotes a boundary layer is specified on both ends of the dimension (sides and center for r, top and bottom for z)

The total number of elements used was limited by both memory and reasonable run-speed for the SEMG code, since it had not yet been parallelized. The number of boundary layer elements and the initial size were usually selected such that the last boundary layer element was smaller than the size of the non-boundary layer elements by approximately the geometric growth ratio. Visualizations of each mesh in the (r, z) plane are included in Figure 3.8 and Figure 3.9.

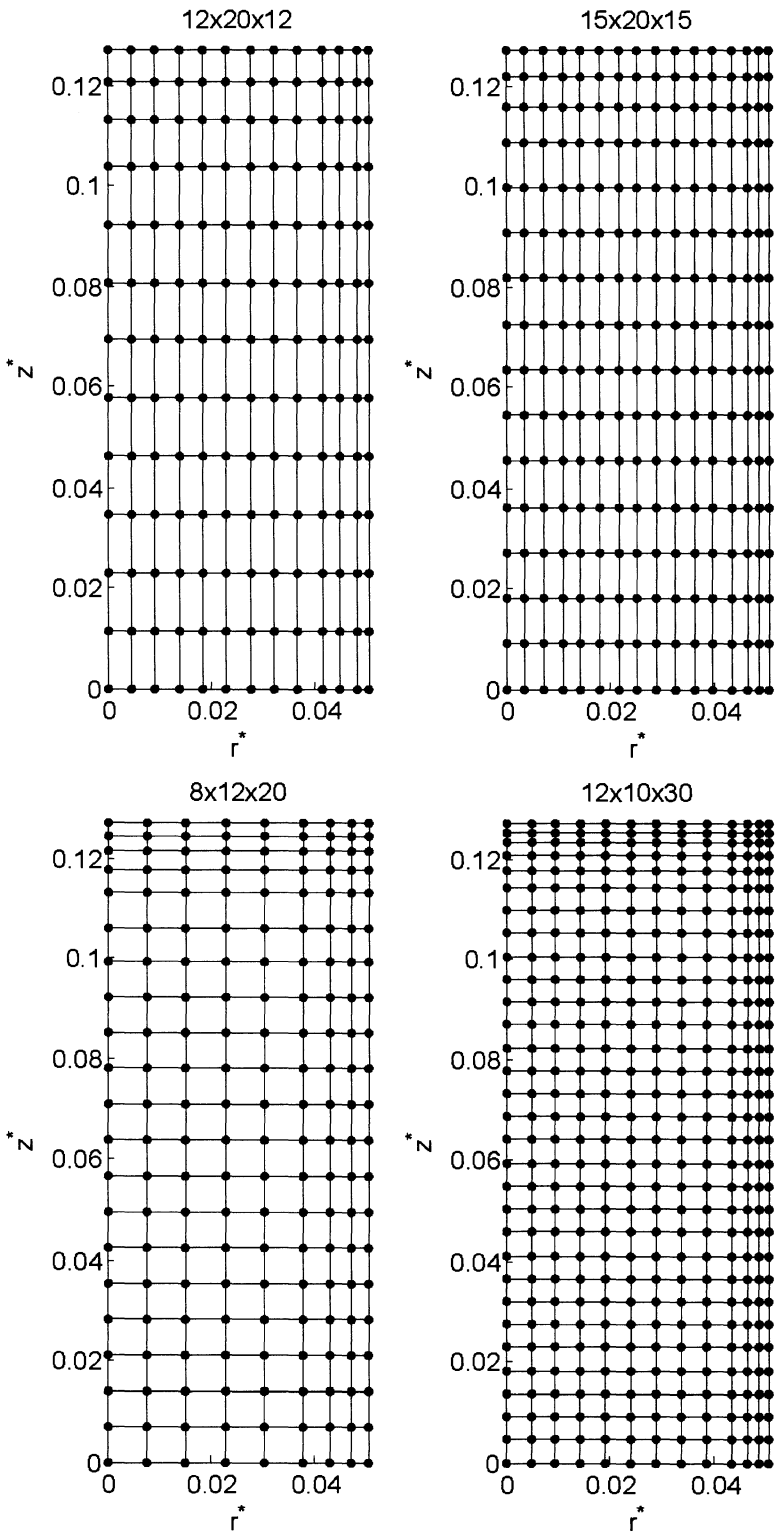

Figure 3.8 – (r, z) projections of meshes for $\gamma = 2.5$ used with SEMG

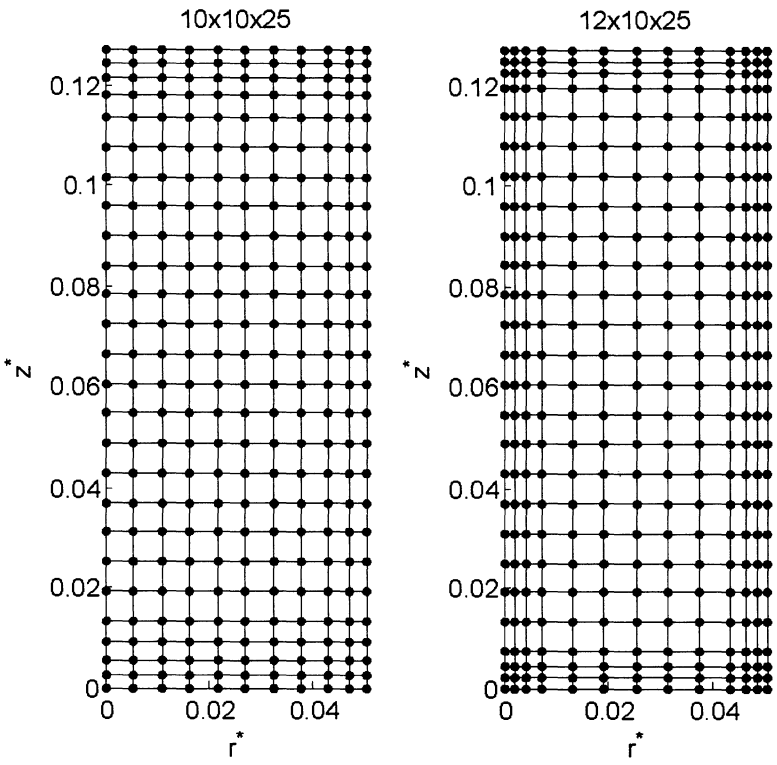

Figure 3.9 – (r, z) projections of meshes for $\gamma = 2.5$ used with SEMG

3.2.3. SEMTEX Spectral Element Code

Once convergence issues with SEMG were discovered to be non-trivial to isolate and solve, numerical simulations were moved to a well-established open-source spectral element CFD code, since development of numerical methods was not the main focus of this thesis. Formulation and development of the SEMTEX code can be found in (Blackburn and Sherwin 2004). SEMTEX uses spectral elements in the (r, z) plane and a Fourier expansion in the azimuthal (θ) direction. Thus only a two-dimensional mesh in the (r, z) plane is generated and the user simply specifies the number of desired terms in the Fourier expansion for the θ direction. A summary of the input parameters for SEMTEX can be found in Table 3.9. Unlike the procedure in SEMG, the input parameters for SEMTEX were all non-dimensional with $\Omega = 1$, $R = 1$ and $H = \gamma$. The Reynolds number was adjusted by changing the kinematic viscosity to achieve the desired parameter. Since the governing equations for this problem depend only on Re and γ, results are easily scaled between a dimensional or non-dimensional system for comparison. The default time-step size of $\Delta t = 0.01$ was used for a few runs, but was doubled to $\Delta t = 0.02$ to reduce run times. The CFL number was monitored as the code time-stepped and remained reasonable ($\sim$0.1) throughout all simulations. Time-dependent simulations were performed for all Reynolds numbers. The code was time-stepped to a steady-state solution, if one existed.

SEMTEX Simulation Parameters	
Coordinate System	Cylindrical
Unknowns	3 Velocities and Pressure
Number of Fourier terms in θ	32
Interpolation Order for Velocity and Pressure	3rd
Time-stepping Order	2nd
Relative/Absolute Tolerance	10^{-12}
Dimensions of Cylinder (non-dimensional)	$R = 1$ $H = \gamma = 2.5$
Fluid Properties	$\nu = \frac{1}{Re}$
Boundary Conditions	Ω is always set to 1. Re adjusted by changing ν $v = r, u = w = 0$ (Lid)
Time Step Size	$\Delta t = 0.01$ (Default) or $\Delta t = 0.02$

Table 3.9 – Input parameters for SEMTEX simultaions

A single two-dimensional (r, z) mesh was generated with the structured mesh generator used previously and converted to a format usable by SEMTEX. Two different resolutions in the θ direction were tested on this mesh. The two-dimensional mesh had the same (r, z) resolution as the 12x10x25 mesh used for the SEMG code and was simply scaled so that $R = 1$. A visualization of the mesh can be seen in Figure 3.10 with boundary layer parameters shown in Table 3.10.

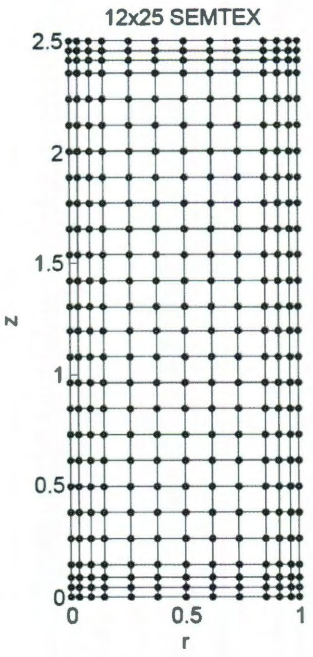

Figure 3.10 – 12x25 $(r,\ z)$ mesh for SEMTEX

12×25, (r,z) Mesh Parameters for SEMTEX **$R = 1, H = \gamma = 2.5$** Boundary layers on center and sides in r and on top and bottom in z			
Nr	12	Nz	25
BL_r	3*	BL_z	3*
Δr_0	0.0394	Δz_0	0.0394
GR_r	1.2	GR_z	1.2

Table 3.10 – Mesh parameters for 12x25 SEMTEX mesh

3.2.4. Numerical Flow Visualization and Analysis

Paraview is an open-source data visualization and analysis program that was used to interpret the results from the numerical simulations. Both SEMG and SEMTEX can output *.vtk files which are readable by Paraview. Once a flow field has been imported into Paraview through a *.vtk file, a number of different filters, plots, and visualization methods can be applied. Data is also extracted from Paraview as *.csv files and imported into Matlab for plotting or further analysis.

One clarification of note involves the convention used by SEMTEX when it orders velocity variables. Rather than the standard convention where $\boldsymbol{u} = \{u, v, w\}$ and u, v, w correspond to the radial, azimuthal, and axial velocities respectively, SEMTEX uses u, v, w corresponding to the axial, radial, and azimuthal velocities. For the purposes of this thesis the standard convention will always be used even when referring to SEMTEX results.

For SEMG, although the simulation generates a velocity field in cylindrical coordinates, the results are converted to Cartesian coordinates when converted into a *.vtk file. Thus results from SEMG are imported into Paraview in Cartesian coordinates where $\boldsymbol{u}_{xyz} = \{V_x, V_y, V_z\}$ with the x and y axis aligned in the (r, θ) plane and the z axis is the same as in cylindrical coordinates. Calculations for converting velocity fields between Cartesian and cylindrical coordinates can found in Appendix C.

Chapter 4

Experiments and Results

This chapter presents the experiments performed for this thesis and results. First numerical simulations are presented to help the reader visualize the general flow characteristics of the rotating lid-driven cylinder problem. Numerical and experimental results are then compared for tests run with tap water as the working fluid and a 20% glycerin-water solution by volume as the working fluid. These tests are meant to verify the accuracy of the UDV and determine the strengths and limitations of UDV as a suitable flow visualization technique for this configuration.

4.1. Numerical Simulation Results

Numerical simulations were performed for $\gamma = 2.5$ on both SEMG and SEMTEX with Reynolds numbers ranging from $Re = 500$ to $Re = 3000$ in steps of 500. The steady, axisymmetric base-flow is dominant until approximately $Re = 2700$ when the $k = 0$ instability sets in, leading to an axisymmetric periodic flow. Thus the $Re = 2500$ run is expected to be axisymmetric and steady while the $Re = 3000$ run is expected to be axisymmetric and periodic. Simulations are performed to generate flow-fields which are compared to experimental measurements both of the base-flow and of the instability. Identification of the critical Reynolds number was not the goal, thus choosing $Re = 3000$ ensured that the instability grew quickly in time, shortening the required computation time, while remaining below the critical Reynolds number for the next instability at $Re \approx 3300$ (Gelfgat *et al.* 2001; Sørensen *et al.* 2006).

Steady runs with SEMG were performed by ramping up the Reynolds number and using the results from the previous Reynolds number as the initial guess. An initial run at $Re = 1$ was performed with zero initial conditions to ensure convergence of the linear solver. Convergence issues at higher Reynolds numbers were experienced with SEMG steady runs generally when $Re > 2000$. These convergence issues and the benchmarking runs of SEMG against SEMTEX are documented in Appendix D in case future work is to be done on this problem, but are omitted here since they are not necessary for the understanding of this thesis.

SEMTEX uses a transient solver for all cases and time-steps to steady-state solutions when they exist. The initial run with $Re = 500$ and zero initial conditions converged with no issues and successive runs used previous steady-state results as the initial condition. Only results from SEMTEX at the various Reynolds numbers using the 12x25 (r, z) mesh with 32 azimuthal modes are presented but these are quantitatively similar to convergent runs on SEMG.

4.1.1. Numerical Simulations: $\gamma = 2.5$, $Re = 500$

At $Re = 500$ the flow field generated in the rotating lid-driven cylinder is steady, axisymmetric and forms a vortex with most of the downward mass flux concentrated in a jet near the outside wall. Despite the low Reynolds number and the axisymmetry, the flow is still quite complex. The rotating lid acts as a viscous pump, drawing fluid up in the center and flinging it out and down the sides. The concentrated vortex is in the shape of an elongated toroid with an overall azimuthal velocity that causes the fluid particles to swirl as they travel. Visualizations of this flow are provided in Figure 4.1. The picture on the left shows streamlines projected onto the (r, z) half-plane with the azimuthal velocity component removed. The rotating lid is at the top of the picture and the left edge corresponds to the outside wall of the cylinder. The right edge is the axis of the cylinder. The lines are colored by velocity magnitude. The picture on the right shows 3D stream tracers that have been seeded near the core of the cylinder. The point $(r = 0, z = 1.25)$ is marked by the red, yellow, and green cross. The maximum velocity at the outer edge of the lid is $\Omega R = 1$ for all cases and the Reynolds number is adjusted by varying kinematic viscosity. The flow is steady and axisymmetric.

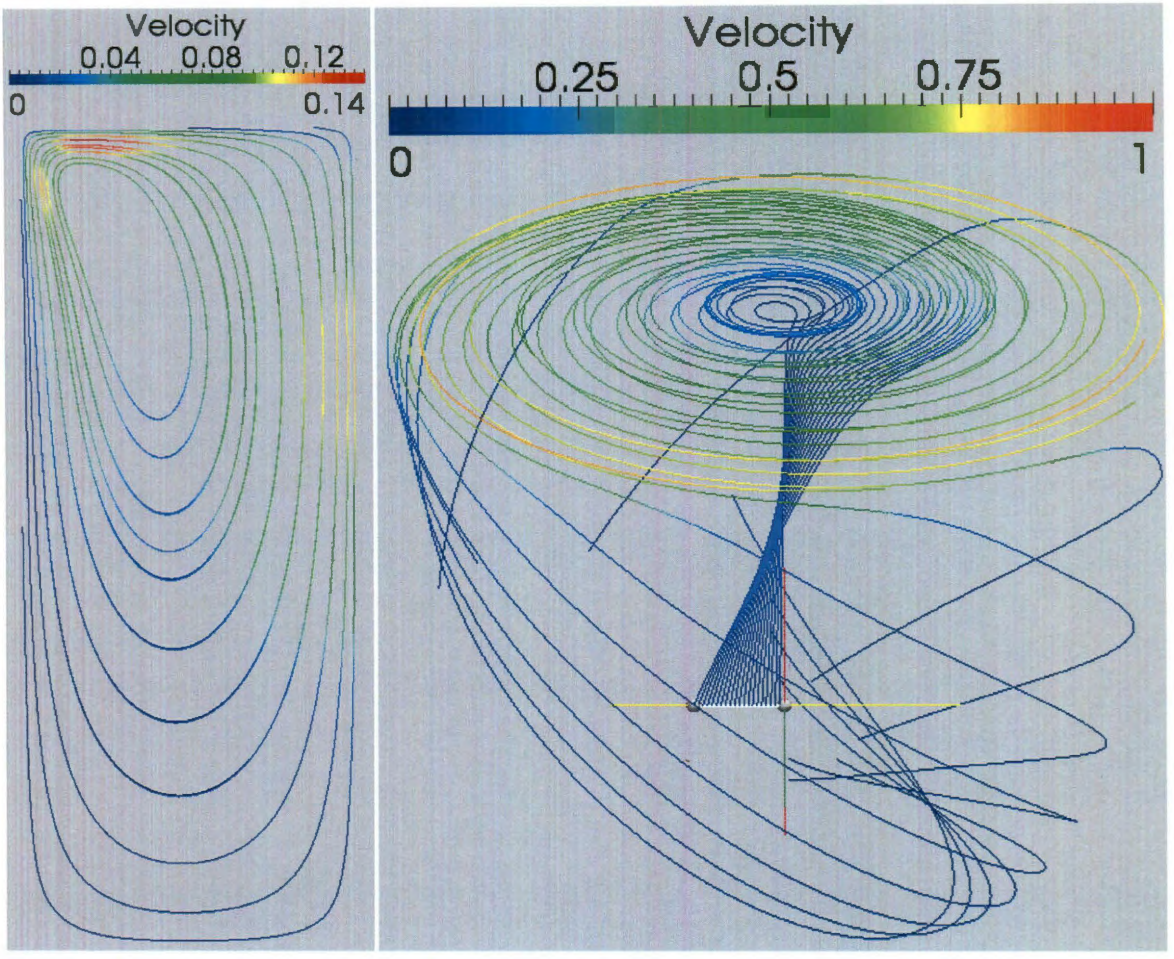

Figure 4.1 – Flow visualizations: $\gamma = 2.5$, $Re = 500$

For $Re = 500$ a majority of the flow is traveling significantly slower than the maximum input velocity at the edge of the lid. The azimuthal velocity imparted by the rotating disk is only dominant in the region very close to the lid. The axial flow is fairly weak, especially in the bottom third of the cylinder. Also, fluid is drawn toward the disk in a relatively wide cone in the core of the cylinder. However, fluid jets down along the walls of the cylinder in a narrow gap, as seen in the top left corner in Figure 4.1 (left).

4.1.2. Numerical Simulations: $\gamma = 2.5$, $Re = 1000$ to $Re = 1500$

The flow characteristics do not change significantly as the Reynolds number is increased to 1500. Figure 4.2 and Figure 4.3 show similar visualizations for $Re = 1000$ and $Re = 1500$ cases respectively. The axial recirculation becomes stronger and travels further down into the bottom of the cylinder. This is evident by the elongation of the circular paths in Figure 4.2(left) and Figure 4.3(left) and the higher velocities when compared with the $Re = 500$ case.

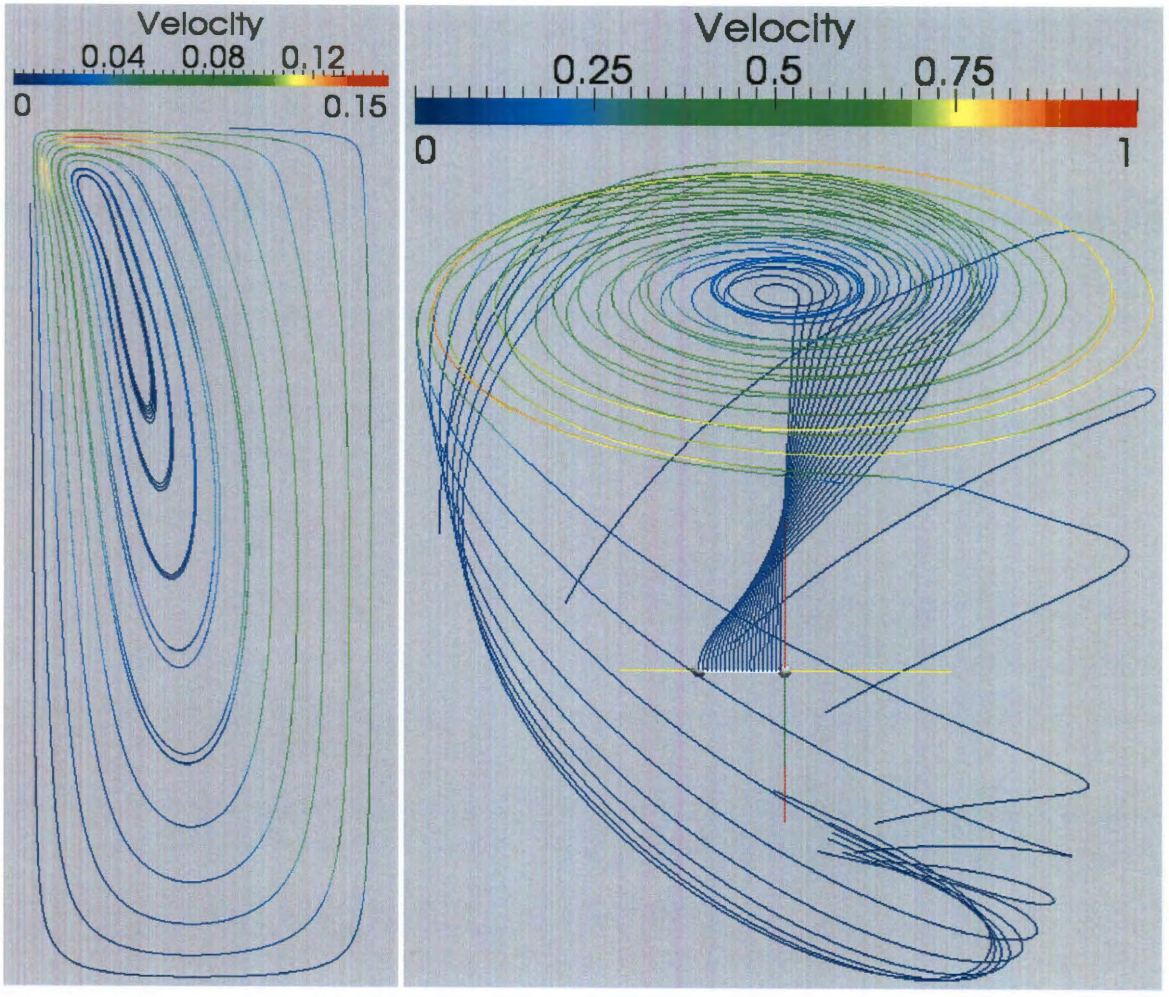

Figure 4.2 – Flow visualizations: $\gamma = 2.5$, $Re = 1000$

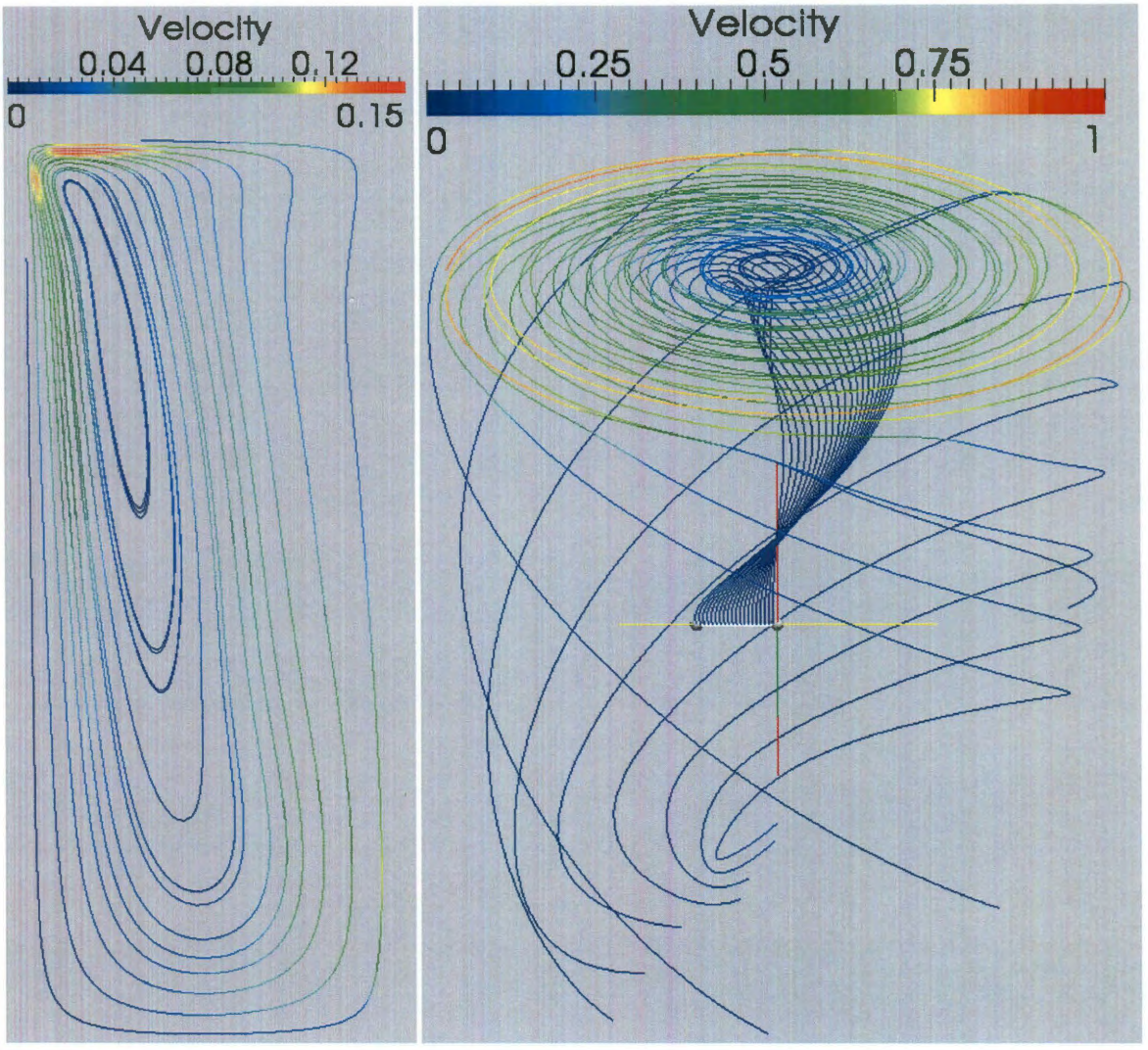

Figure 4.3 – Flow visualizations: $\gamma = 2.5$, $Re = 1500$

The azimuthal velocity component also becomes more dominant in the flow field, as evident by the tighter helical path of the stream tracers near the core of the cylinder in Figure 4.2(right) and Figure 4.3(right). The bending of streamlines away from the core of the cylinder near the lid in Figure 4.3(left) also suggests that the flow is beginning to slow in that region and portends vortex breakdown and the formation of a recirculation bubble.

4.1.3. Numerical Simulations: $\gamma = 2.5$, $Re = 2000$ to $Re = 2500$

At $Re = 2000$, two re-circulating vortex breakdown bubbles form as shown in Figure 4.4(left). The flow remains steady and axisymmetric. The inner core of the cylinder is almost stagnant above the first recirculation bubble but the axial velocity remains high in narrow bands between the outer wall and the inner core of the cylinder.

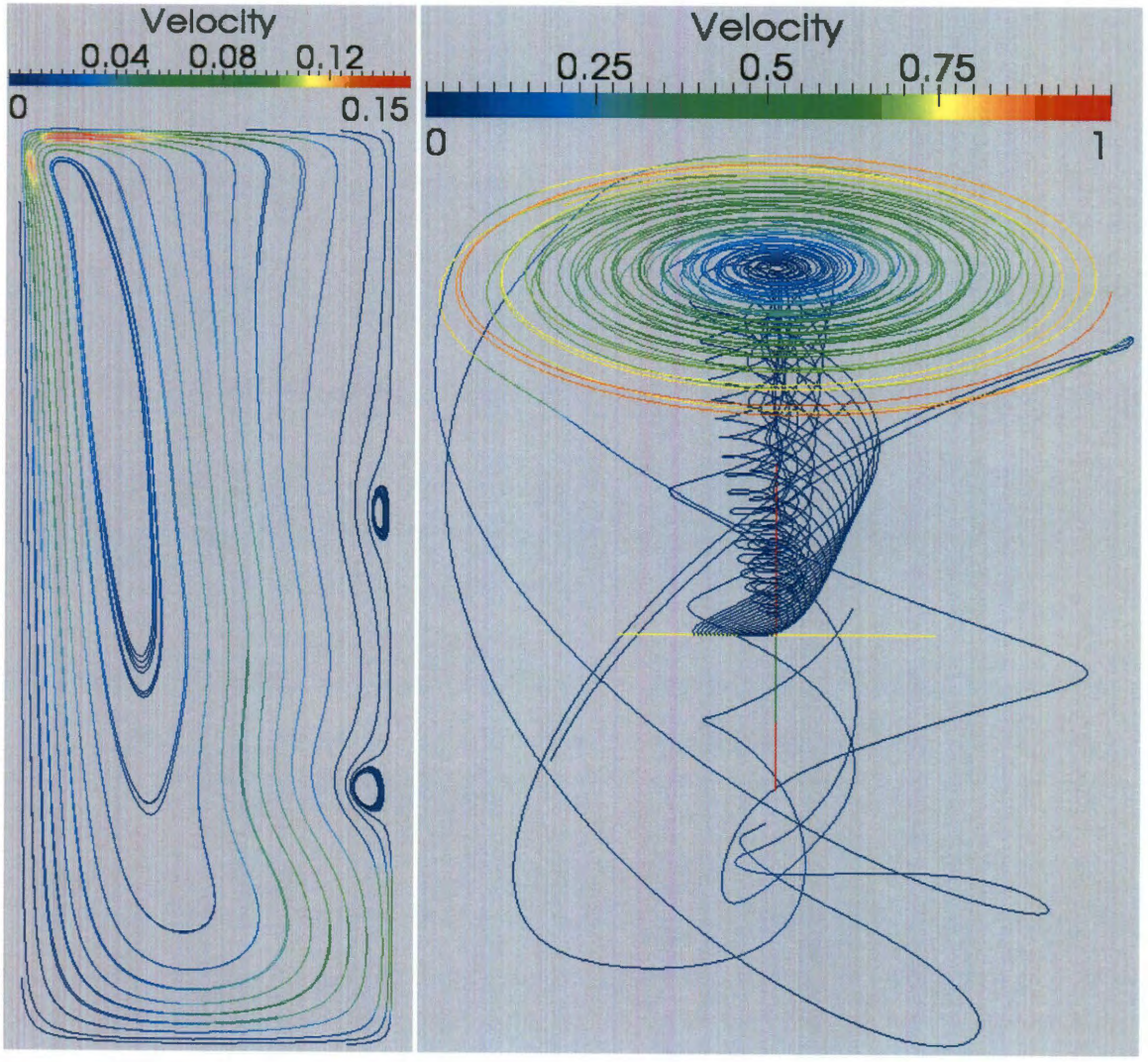

Figure 4.4 – Flow visualizations: $\gamma = 2.5$, $Re = 2000$

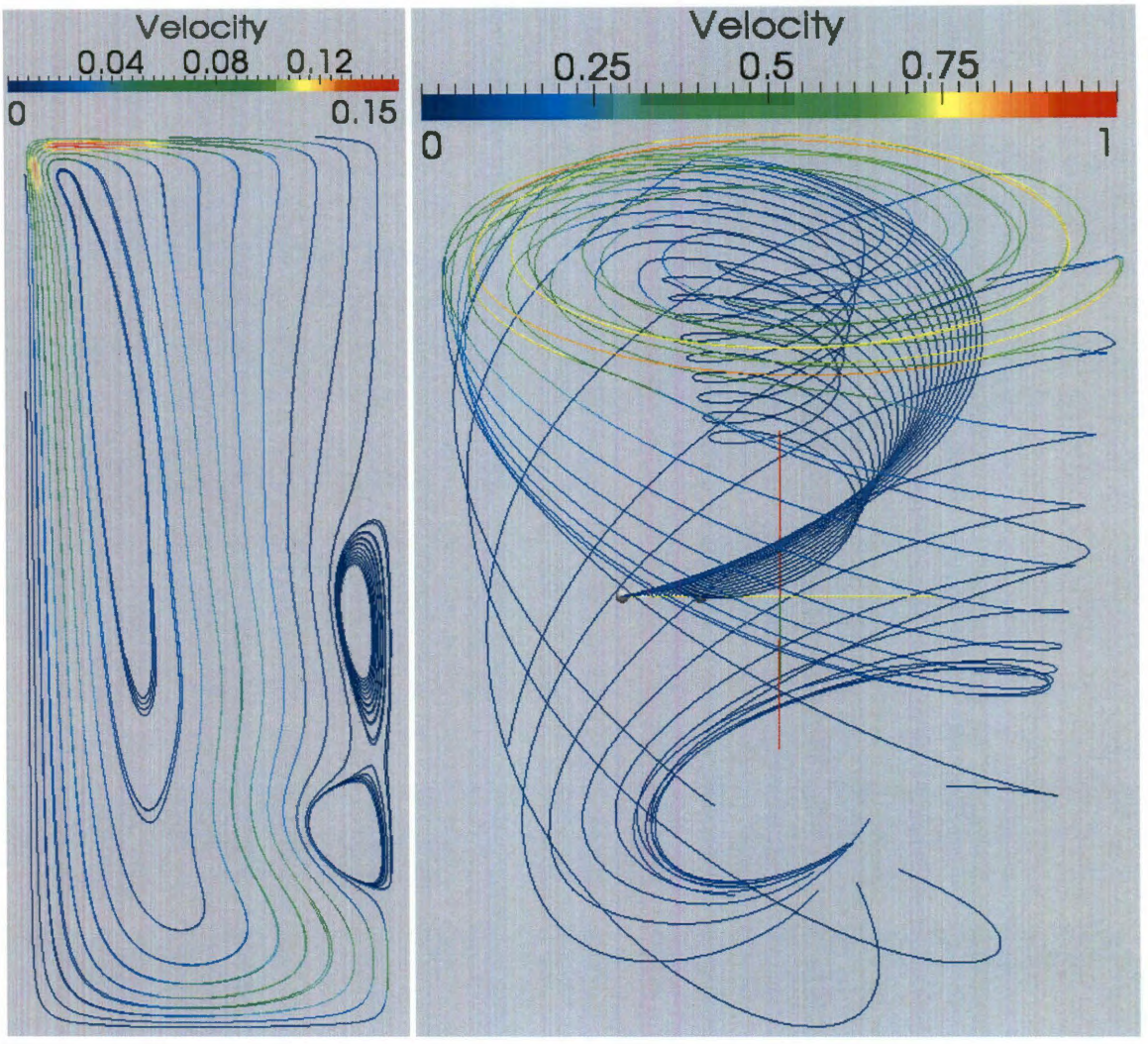

Figure 4.5 – Flow visualizations: $\gamma = 2.5$, $Re = 2500$

At $Re = 2500$ the recirculation bubbles grow, join together, and move farther down in the flow field, as shown in Figure 4.5(left). Large gradients exist at the bottom of the cylinder for both $Re = 2000$ and $Re = 2500$. The seed particles in Figure 4.5(right) are placed away from the axis of the cylinder to show the flow around the core. The maximum velocity in the (r, z) plane remains approximately 15% of the maximum input velocity up to $Re = 3000$.

4.1.4. Numerical Simulations: $\gamma = 2.5, Re = 3000$

At $Re = 3000$, numerical simulations show that the flow becomes time-periodic but remains axisymmetric. This is consistent with the findings in literature summarized in Table 3.6. The specific parameters used for the transient run are shown in Table 4.1. The simulation was run for 4000 non-dimensional time units to bypass the initial transients in the solution. The simulation was then run for another 200 non-dimensional time units and data was recorded every 2 non-dimensional time units. The CFL number remained on the order of 0.1 during all time-steps.

$\gamma = 2.5, Re = 3000$ Transient SEMTEX Parameters	
Δt (non-dimensional)	0.02
Data Collected (non-dimensional)	$\hat{T} = 4000$ *to* $\hat{T} = 4200$
Iterations Between Data Writes	100

Table 4.1 – $Re = 3000$ transient simulation parameters

Figure 4.6 shows streamlines of the flow projected into the (r, z) plane for a single period of the flow at $Re = 3000$. As before, the left boundary of each picture is the wall of the cylinder and the right boundary is the axis. $T = 0$ in the picture corresponds to the data collected at $\hat{T} = 4002$ in the overall simulation. Figure 4.7 shows (r, θ) slices of the cylinder at the mid-plane ($h = 1.25$). The figure shows that the flow is axisymmetric in all three velocity components. Only slices at $T = 0$ are shown, since there are only subtle variations in these figures through time.

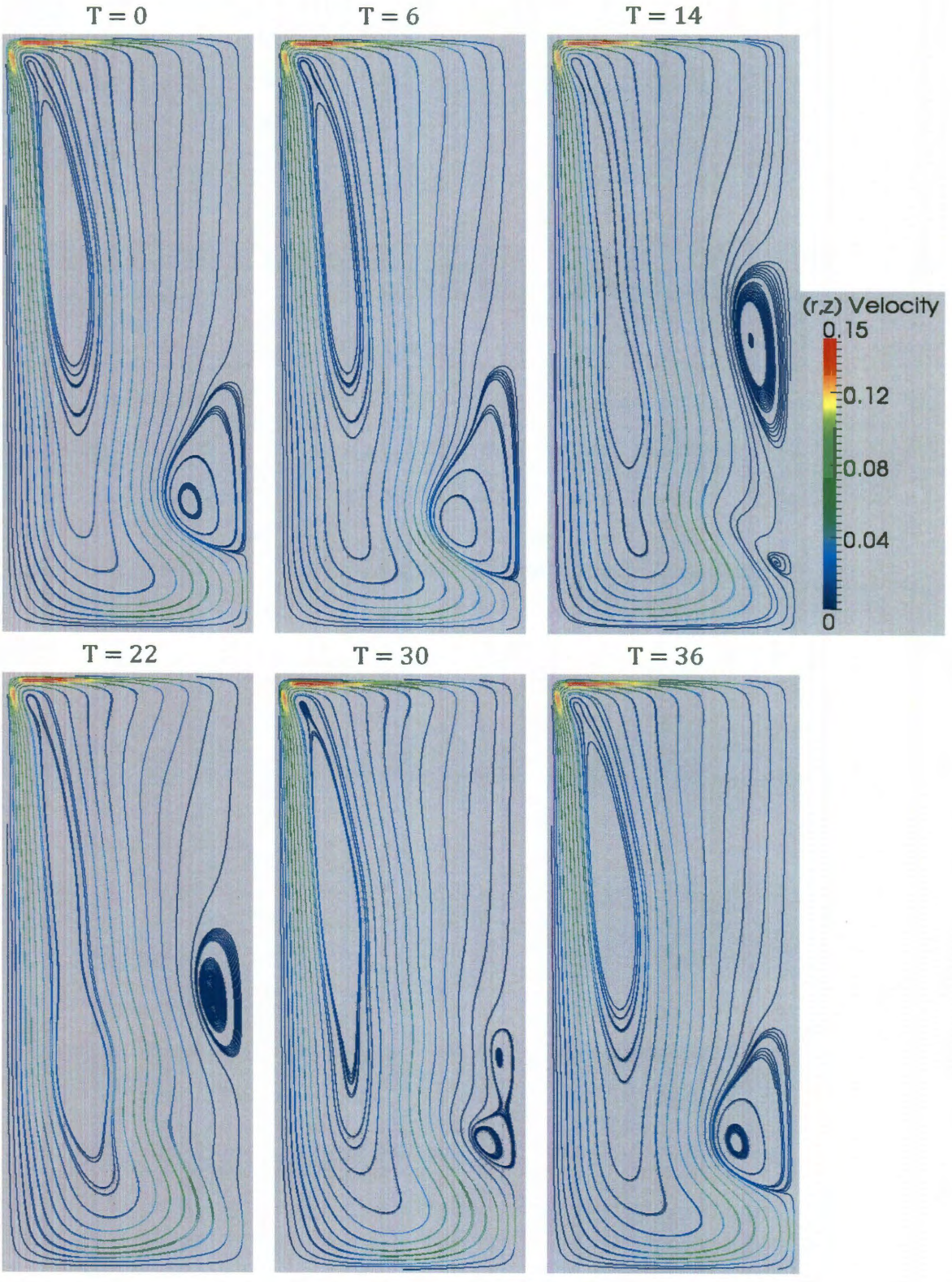

Figure 4.6 – Streamlines in (r, z) half plane for $Re = 3000$

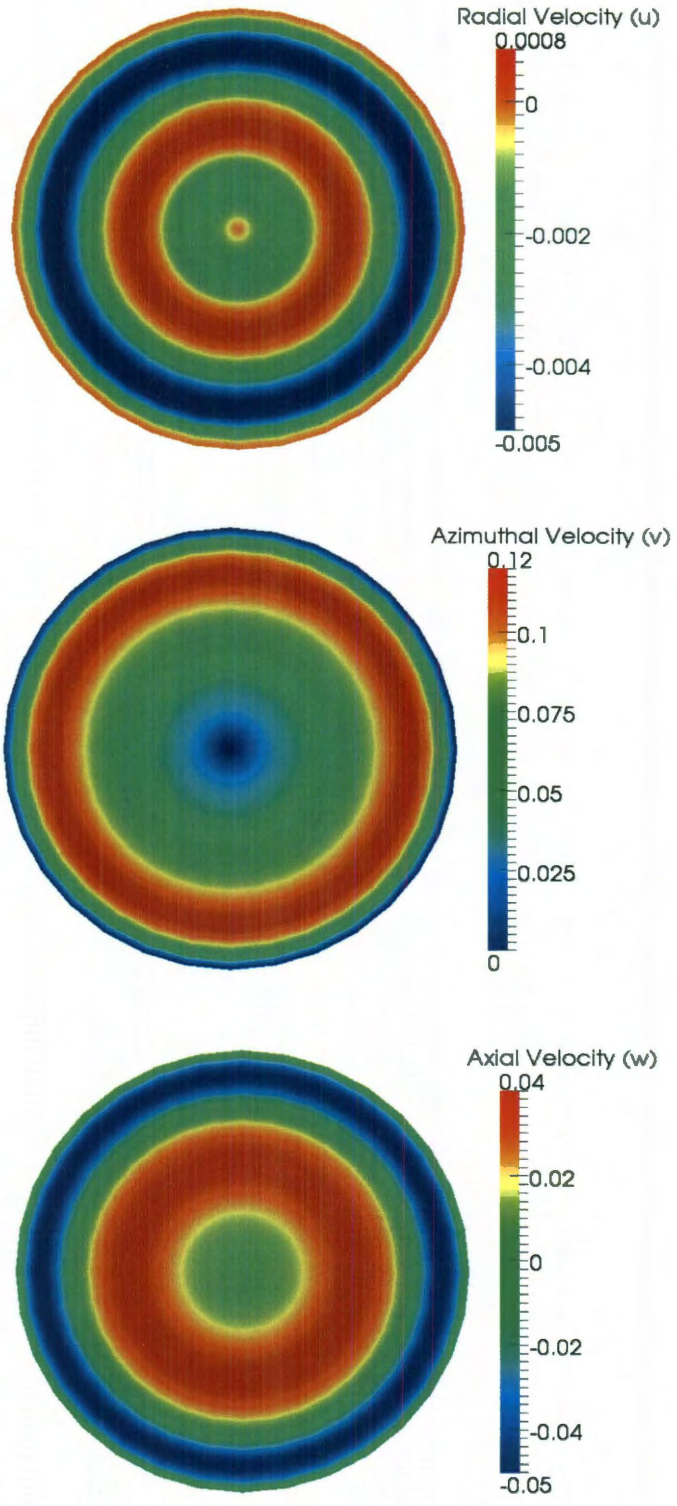

Figure 4.7 – (r, θ) slices at mid-plane of the cylinder $(h = 1.25)$ showing (u, v, w) are axisymmetric for $Re = 3000$ at $T = 0$

To demonstrate the periodic behavior of the flow, a velocity profile along a line is plotted as a surface in time. In a "time-profile plot" distance along the line is plotted on the ordinate, time is plotted along the abscissa, and the velocity is plotted as a colored field. For the time-profile plots presented, the axial velocity, *w*, is sampled along a line parallel to the axis of the cylinder but offset at certain radial distances. Figure 4.8 shows the axis of the cylinder as a solid line. The representative dashed line is that along which data is sampled. By sampling only the axial velocity, *w*, along this line, the profile obtained is the same velocity profile measured by the UDV when probes are mounted on the bottom surface of the cylinder.

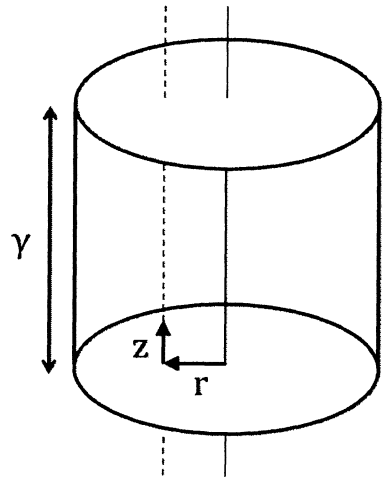

Figure 4.8 – Dotted line along which data is sampled for "time-profile" plots

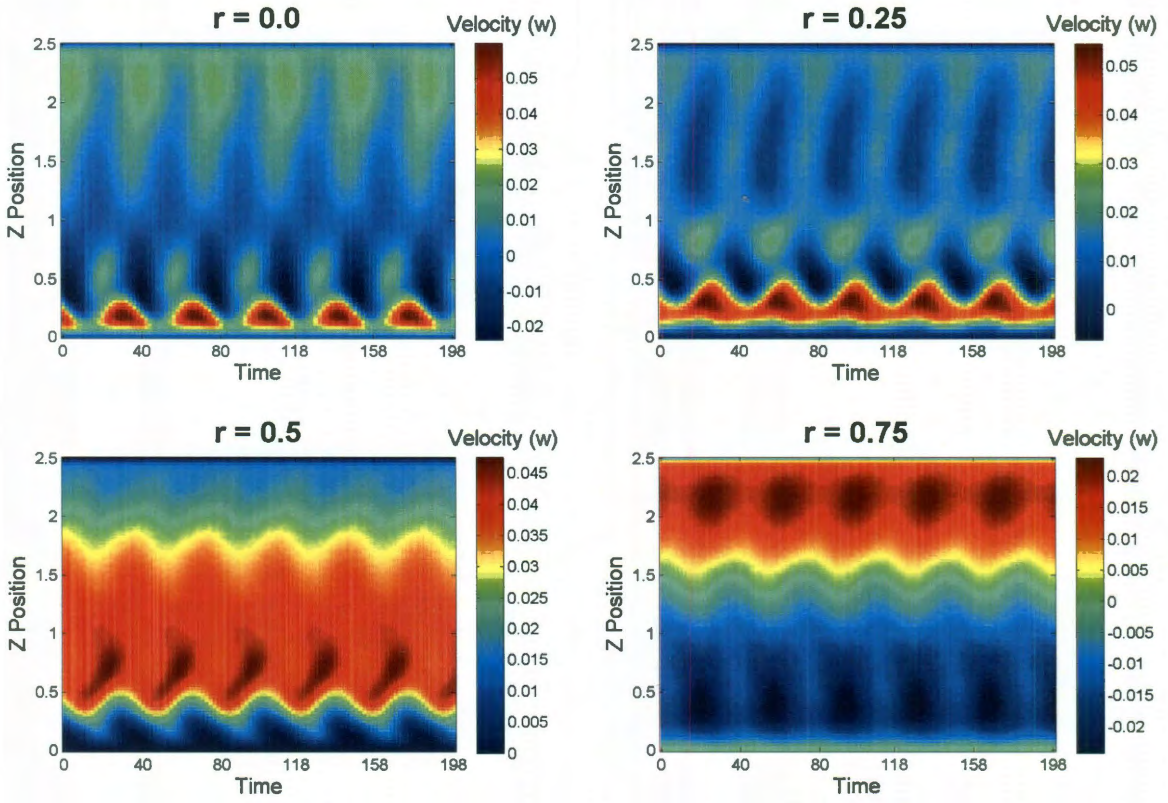

Figure 4.9 – Time-profile plots of axial velocity at various *r* values along a line parallel to the axis of the cylinder. All values are non-dimensional.

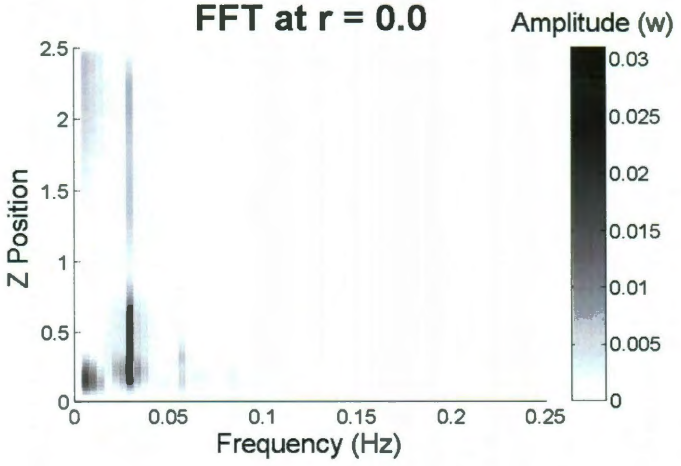

Figure 4.10 – FFT of time-profile plot to determine frequency of periodicity

Figure 4.9 shows four time-profile plots corresponding to different radial offsets. The periodicity of the solution can be clearly observed. To quantitatively determine the frequency of the periodicity, a Fast Fourier Transform (FFT) is performed on the w velocity as it varies through time, for every point along the z-position. This type of information must be plotted in three dimensions and again a colored 2D plot is used. Figure 4.10 has the z location along the cylinder on the ordinate, frequency on the abscissa, and the amplitude of the velocity in the field. The steady-state component of the velocity ($f = 0\ Hz$) has been removed from the plot so that the non-zero frequency components are easier to observe. A strong frequency component is observed at $f = 0.0273\ Hz$. A non-dimensional frequency calculated using Equation (3.21) is comparable to the observed frequency of this instability found in published results (Table 3.6).

$$\omega = \frac{2\pi(0.0273)}{1.0} = 0.1715$$

4.2. Experimental Results: Water

Experimental results obtained with tap water as the working fluid are compared to SEMTEX numerical results. Table 4.2 shows a summary of relevant dimensions and fluid properties.

Water Experiment		
Radius of Cylinder, R^*	2 *inches*	0.0508 m
Height of Cylinder, H^*	5 *inches*	0.127 m
Aspect Ratio, γ	2.5	
Kinematic Viscosity		$1 \times 10^{-6} \frac{m^2}{s}$

Table 4.2 – Cylinder dimensions and fluid properties for water experiments

The UDV probe was mounted to the bottom of the cylinder at four different radial offsets. In this probe configuration, the UDV recorded the axial component of the fluid velocity along a line parallel to the axis of the cylinder, but offset in the radial direction. Since the UDV measures positive velocities away from the probe, the sign convention is consistent with the coordinate system defined for the cylinder and the UDV directly measures the axial velocity, w. Table 4.3 summarizes the radial offset values used, the Reynolds numbers at which data was collected, the acquisition time for each UDV profile, and the number of profiles collected. The radial offset values are shown both in dimensional and non-dimensional units.

Summary of Data Collected			
Radial Offset	**Reynolds Number**	**UDV Profile Acquisition Time [s]**	**Number of Profiles Collected**
$r^* = 0.0\ m$ $r = 0$	1000	1.05	499
	1500	1.05	499
	2000	1.05	593
	2500	1.05	499
$r^* = 0.0127\ m$ $r = 0.25$	1000	1.05	500
	1500	1.05	699
	2000	1.05	500
	2500	1.05	499
$r^* = 0.0254\ m$ $r = 0.5$	1000	1.05	687
	1500	1.05	500
	2000	1.05	499
	2500	1.05	500
$r^* = 0.0381\ m$ $r = 0.75$	1000	1.05	500
	1500	1.05	500
	2000	1.05	519
	2500	1.05	499

Table 4.3 – Summary of data collected for experiments with water

Figure 4.11 shows the measurement configuration of the UDV and how comparison data from numerical simulations is sampled. The UDV is positioned to measure the axial velocity, w, along each of the blue lines. However, since the beam of the UDV diverges as it travels through the fluid, the average velocity that it computes is a weighted average of the axial velocities in the cone represented by the green and red lines. The axial velocity is extracted from numerical simulations along each set of green, blue, and red lines and compared with UDV measurements. The velocity profiles extracted from numerical results for the blue line represent the ideal velocity profile that should be obtained. The velocity profiles along the red and green line represent bounds for the velocity that could be expected due to divergence of the UDV beam. Generally, velocity profiles along the red, green, and blue lines are fairly similar. However, there are a few cases where large differences are observed. The red and green lines represent the sensitivity of the UDV measurements to the path of the beam.

In Figure 4.12 through Figure 4.15 two types of plots are used to present experimental measurements of the axial velocity at a variety of Reynolds numbers and radial offsets. Plots shown on the left are similar to the "time-profile plots" shown in Section 4.1.4. Profiles of the w velocity are collected by the UDV at regular intervals according to the acquisition time in Table 4.3. The z position of the measurement is plotted in the ordinate, time is plotted in the abscissa, and the velocity, w, is plotted in the field as color. Time-profile plots are used to identify any time variation of the velocity profile. Since the flow field is expected to be steady at $Re < 2700$, the "average-profile plots" shown on the right are used to compare the

velocity profiles against numerical results. To generate the average-profile plots, all velocity profiles collected by the UDV are averaged in time and plotted as a solid, black line with *w* velocity on the abscissa and axial location (*z* coordinate) on the ordinate.

Velocity profiles extracted from numerical simulations corresponding to the lines shown in Figure 4.11 are scaled to match the experiments and are also plotted. Velocities along the ideal blue line are plotted as a blue, dashed line and labeled "center". Velocities along the green and red lines that form a cone are plotted as thin dotted green lines or dash-dotted red lines. These are labeled as "outer" and "inner" respectively. All results except for the radial offset are reported dimensionally and only one legend is produced for each set of four average-profile plots.

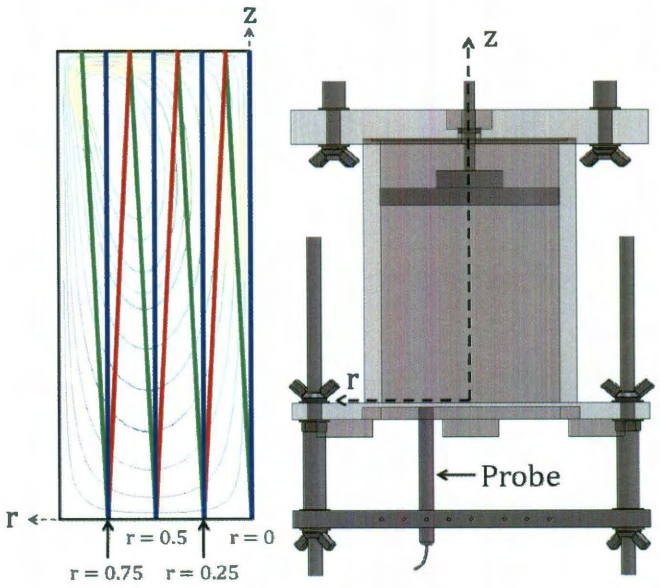

Figure 4.11 – Measurement configuration and lines along which numerical simulation data was extracted

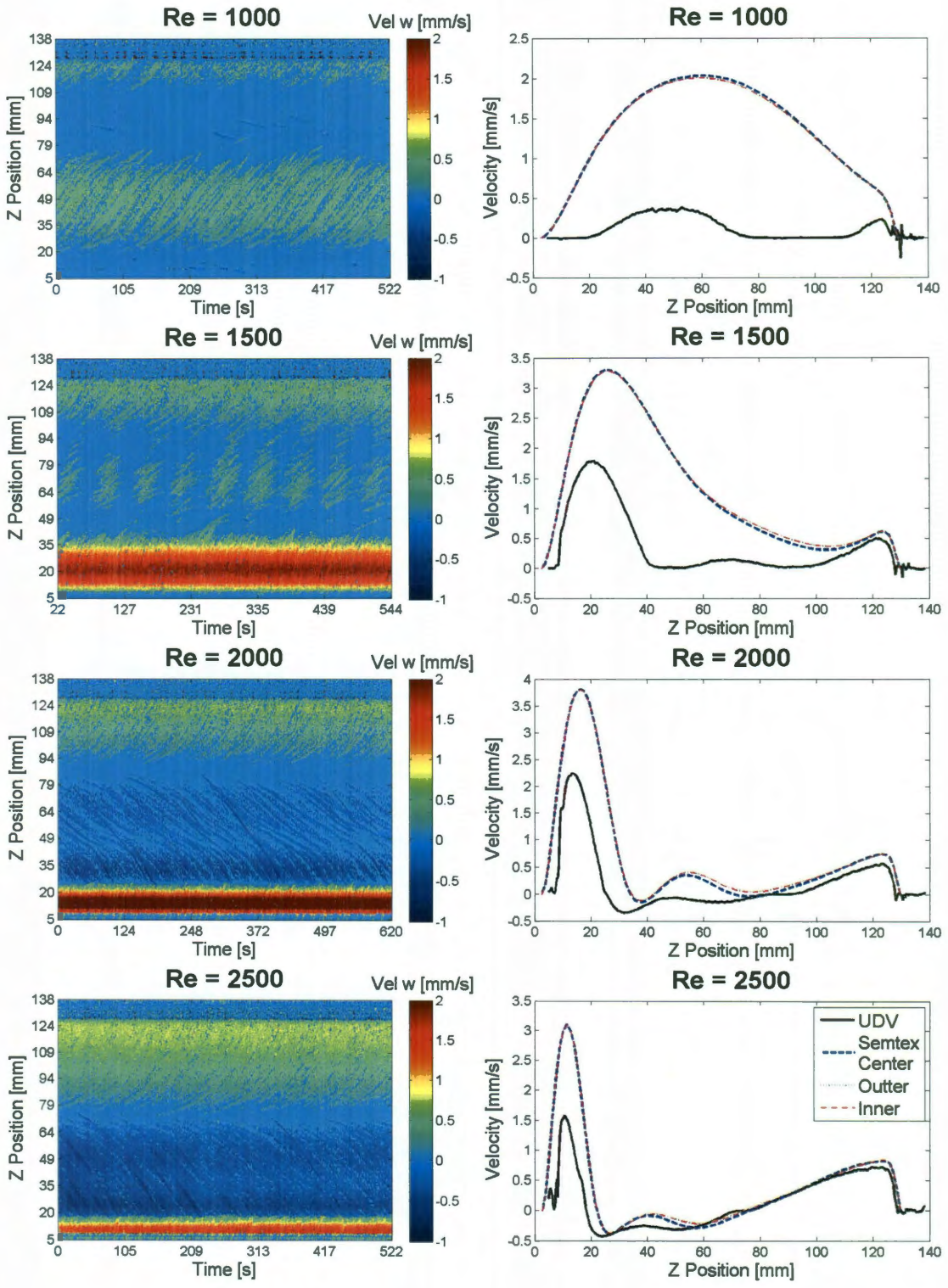

Figure 4.12 – Time-profile and average-profile plots for $r = 0$ offset, water

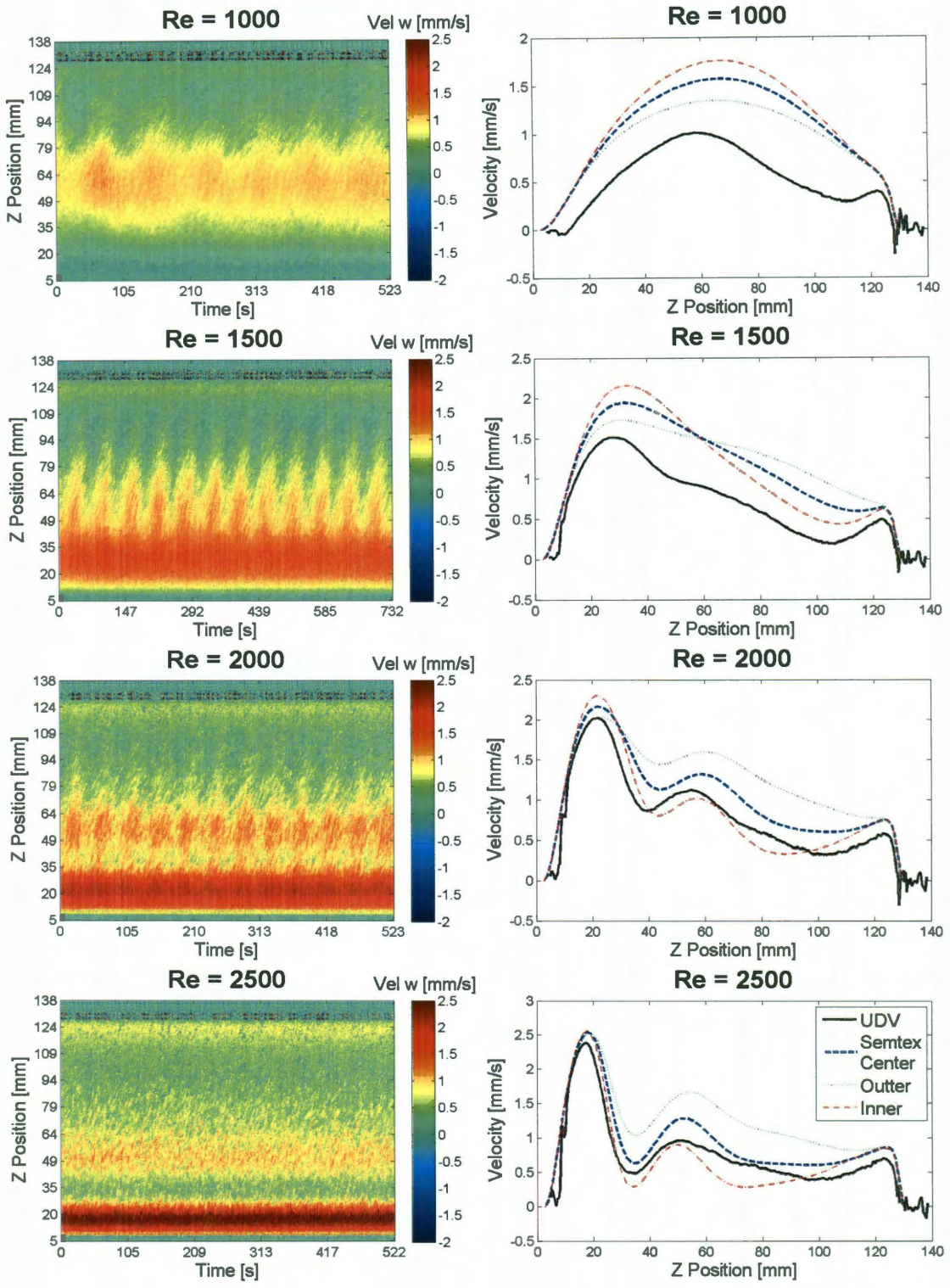

Figure 4.13 – Time-profile and average-profile plots for $r = 0.25$ offset, water

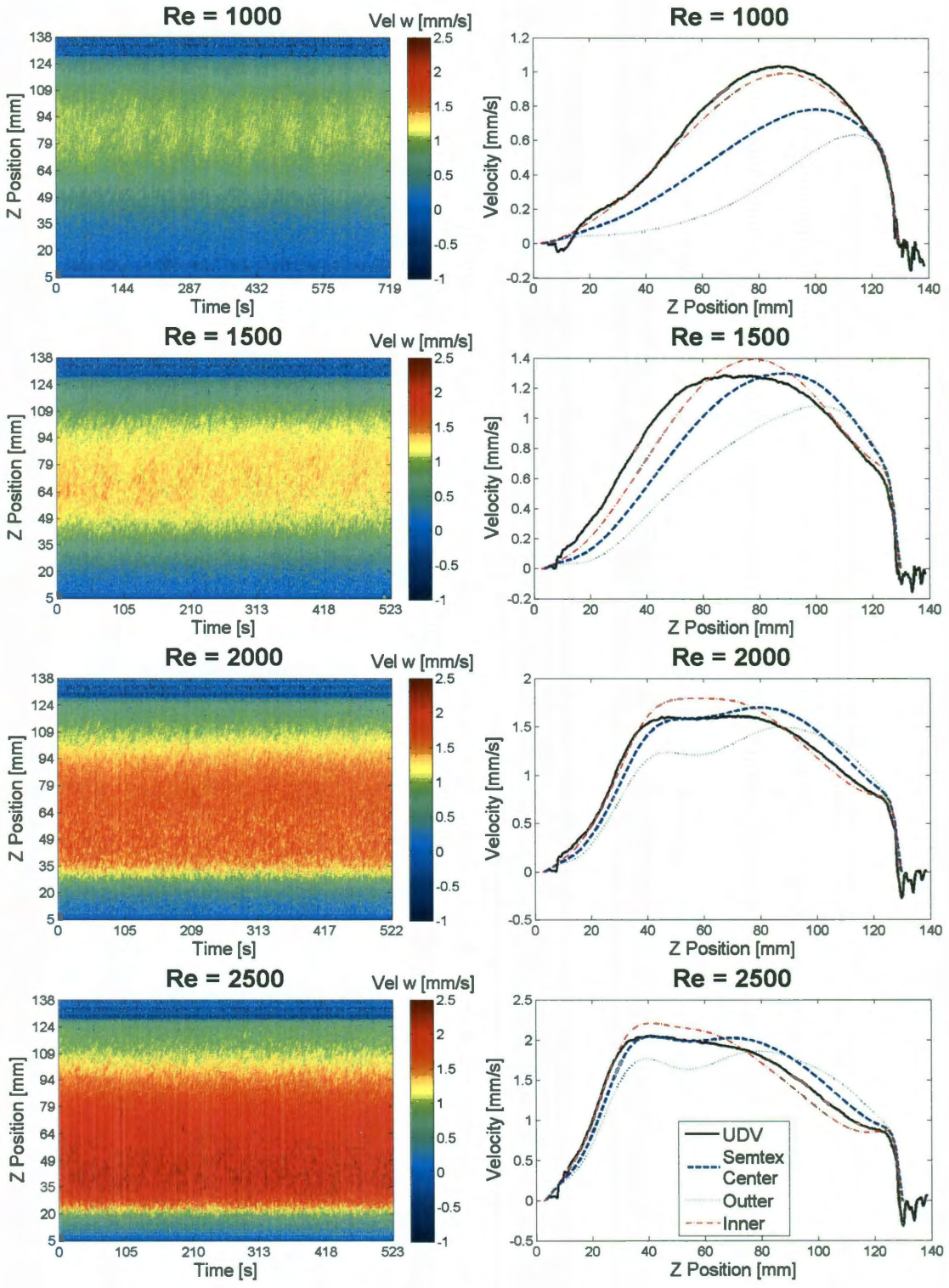

Figure 4.14 – Time-profile and average-profile plots for $r = 0.5$ offset, water

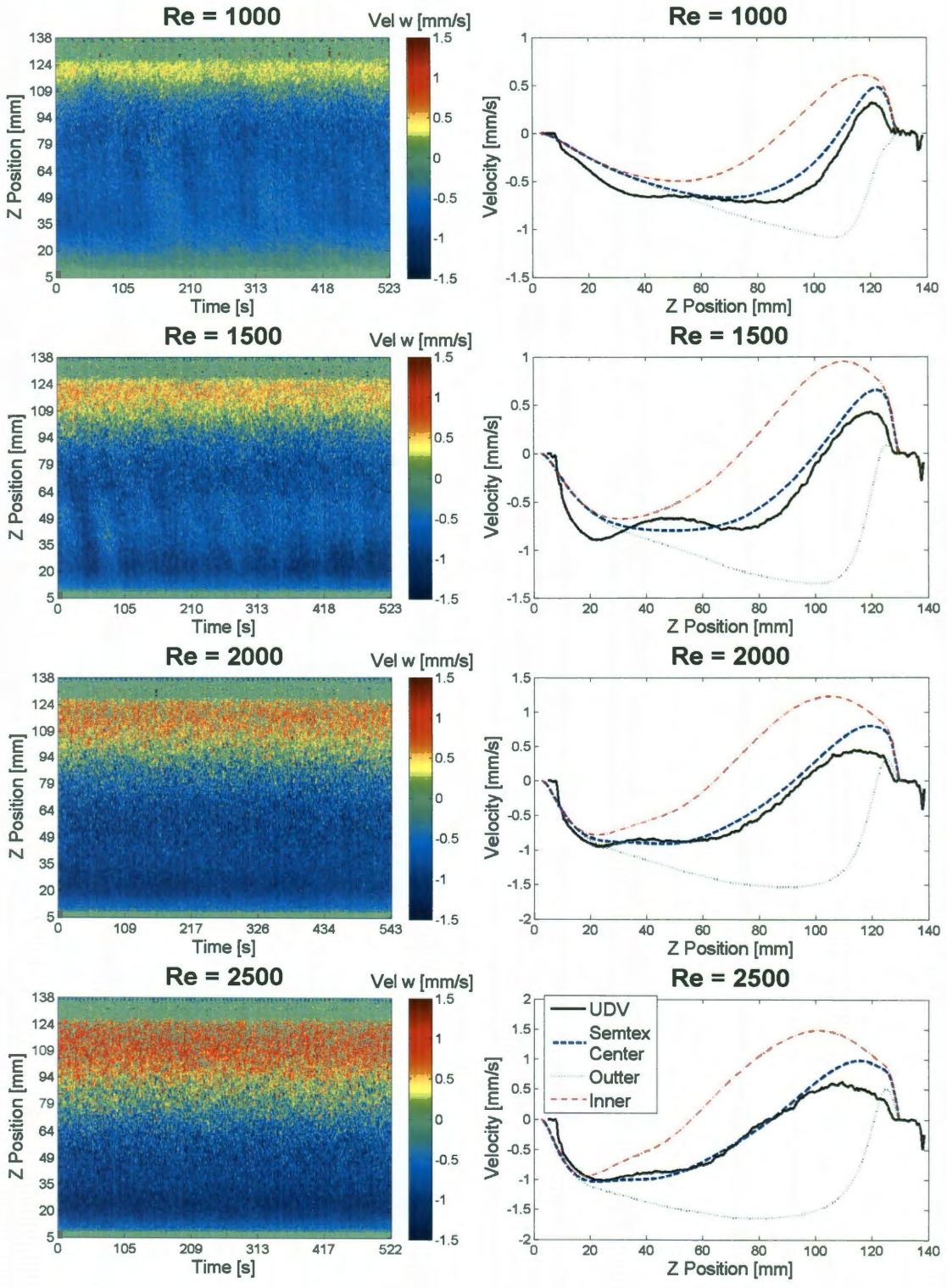

Figure 4.15 – Time-profile and average-profile plots for $r = 0.75$ offset, water

Note it is possible to observe the beginning and end of the fluid domain from the discontinuous changes in color at the top and bottom of time-profile plots. Good agreement between the experimentally measured velocity profiles and the numerical simulations is observed for the $r = 0.25$ to $r = 0.75$ offsets in the average-profile plots, and agreement improves as the Reynolds number is increased. Results from the $r = 0$ case are fairly poor but also show improved agreement as the Reynolds number is increased. A potential cause for discrepancies at $r = 0$ is insufficient time for the experiment to reach steady state before data was recorded. In general, the UDV measurements seemed to under-predict the velocity magnitude. This small bias could be attributed to discrepancies in the fluid viscosities used for calculations, inaccuracies in the rotation rate, or inherent inaccuracies and limitations in the UDV.

Although the flow is predicted to be steady at these Reynolds numbers, the time-profile plots demonstrate that the collected profiles contain a high degree of noise and in some cases exhibit time-dependence. Noise in the system is evident from the non-uniformity in color along the abscissa (in time). This could be caused by a combination of seed particle issues described in Section 2.7, noise inherent in the UDV system, or the low viscosity of water. The low viscosity of water results in a lower overall velocity magnitude for the flow for these low Reynolds number tests. It also makes the flow more susceptible to instabilities caused by external perturbations. Time periodic flow is observed in the $r = 0.25$ trials and a few other isolated trials. It is conjectured the vortex breakdown bubbles formed in the flow are very sensitive to external perturbations and can begin to oscillate or pulsate.

Experimental tests at $Re = 3000$ were expected to be periodic. However they were found to be very inconsistent and are not presented for water. During some trials, the $Re = 3000$ flow would be steady but very noisy. Other tests produced a flow that was periodic but at very high or very low frequencies that were not consistent with the periodic instability that is observed in literature and numerical simulations. These inconsistencies for the $Re = 3000$ tests are thought to be caused by seed particle settling or unstable and turbulent flows triggered during the ramping in Reynolds number.

Despite the issues encountered with noise and an unsteady flow field, the results were promising. It was clear that the UDV is able to resolve subtle changes in the flow field and accurately measure axial velocities that were traveling toward and away from the probe. Once averaged in time, even noisy profiles were shown to produce relatively good results when compared to numerical simulations. Although time-dependent flows were observed when steady flows were expected, it was hypothesized that moving to a higher viscosity working fluid would solve these problems.

4.3. Experimental Results: 20% Glycerin-Water Solution

Experimental results using a 20% glycerin-water solution by volume are presented. Using this working fluid increased the kinematic viscosity by a factor of 1.72 and resolved many of the seed particle suspension issues (Section 2.7). The increase in kinematic viscosity requires a proportional increase to the rotation rate necessary to achieve a certain Reynolds number. Thus in addition to improving the stability of the flow, the increased viscosity also results in a flow field that has an overall higher velocity magnitude. Table 4.4 shows a summary of relevant dimensions and fluid properties.

20% Glycerin-Water Experiment		
Radius of Cylinder, R^*	2 *inches*	0.0508 m
Height of Cylinder, H^*	5 *inches*	0.127 m
Aspect Ratio, γ	2.5	
Kinematic Viscosity		$1.72 \times 10^{-6} \frac{m^2}{s}$

Table 4.4 – Cylinder dimensions and fluid properties for 20% glycerin-water experiment

4.3.1. Experimental Results $Re = 1000$ to $Re = 2500$

Experimental results below the critical Reynolds number were collected at different radial offsets with a probe mounted to the bottom of the cylinder, as in results presented for water. Table 4.5 summarizes the offset values used, the Reynolds numbers at which data was collected, the acquisition time for each UDV profile, and the number of profiles collected for steady-state runs below the critical Reynolds number for the 20% glycerin-water solution. Note that a longer acquisition time is used for all of the runs with the glycerin-water solution. The longer acquisition time combined with the higher overall velocity magnitude of the flow resulted in a dramatic decrease in the amount of noise in the UDV measurements.

Figure 4.16 through Figure 4.19 shows time-profile and average-profile plots for a variety of radial offsets and Reynolds numbers that were collected for the glycerin-water solution. The presentation format is exactly the same as that used for the experimental results with water.

Summary of Data Collected			
Radial Offset	**Reynolds Number**	**UDV Profile Acquisition Time [s]**	**Number of Profiles Collected**
$r^* = 0.0\ m$ $r = 0$	1000	2.51	201
	1500	2.51	230
	2000	2.17	227
	2500	2.17	264
$r^* = 0.0127\ m$ $r = 0.25$	1000	2.51	200
	1500	2.51	199
	2000	2.51	99
	2500	2.51	99
$r^* = 0.0254\ m$ $r = 0.5$	1000	2.17	204
	1500	2.17	202
	2000	2.17	201
	2500	2.17	203
$r^* = 0.0381\ m$ $r = 0.75$	1000	2.17	207
	1500	2.51	202
	2000	2.51	255
	2500	2.51	232

Table 4.5 – Summary of data collected for experiments with 20% glycerin-water

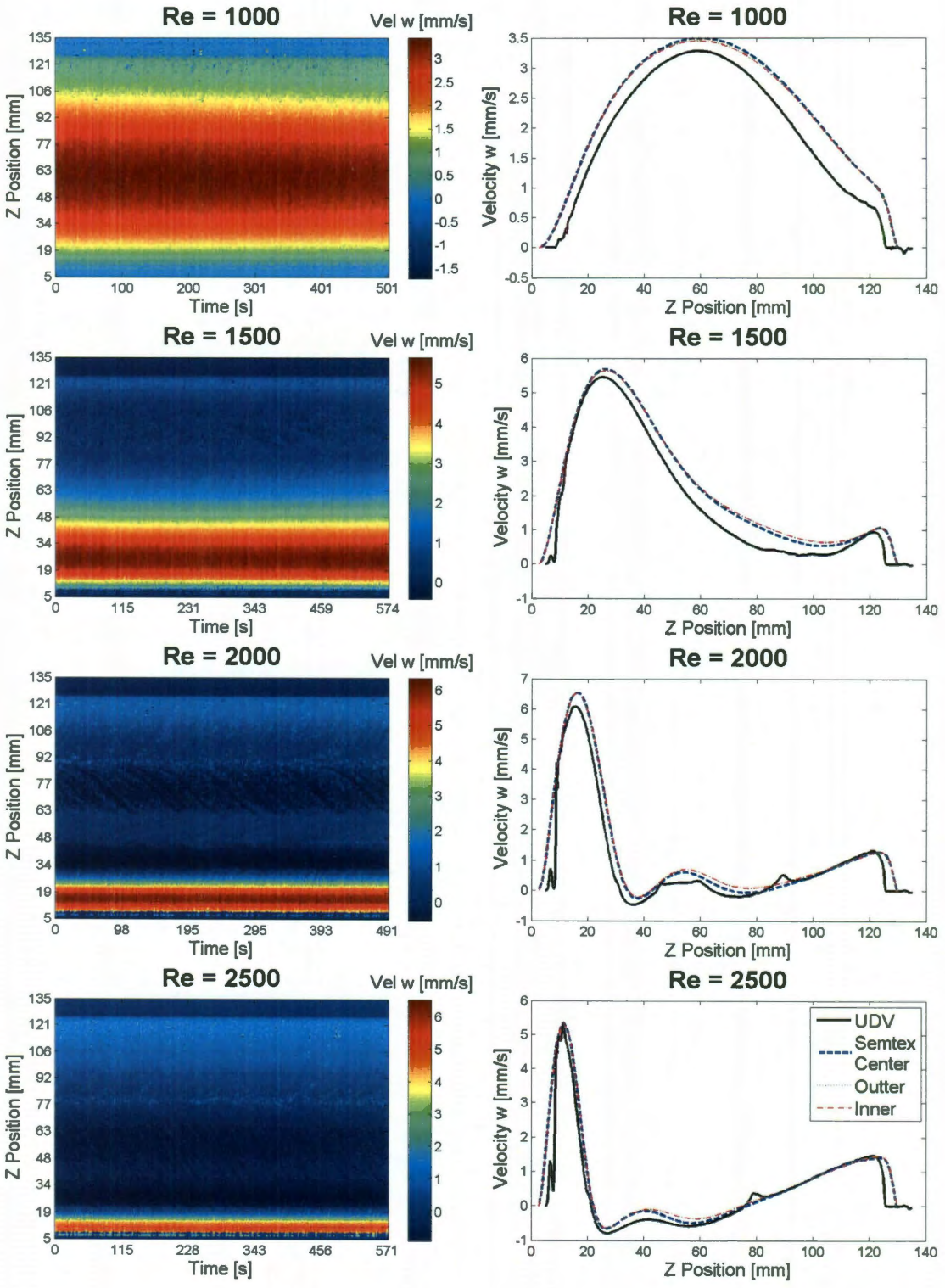

Figure 4.16 – Time-profile and average-profile plots for $r = 0$ offset 20% glycerin-water by volume

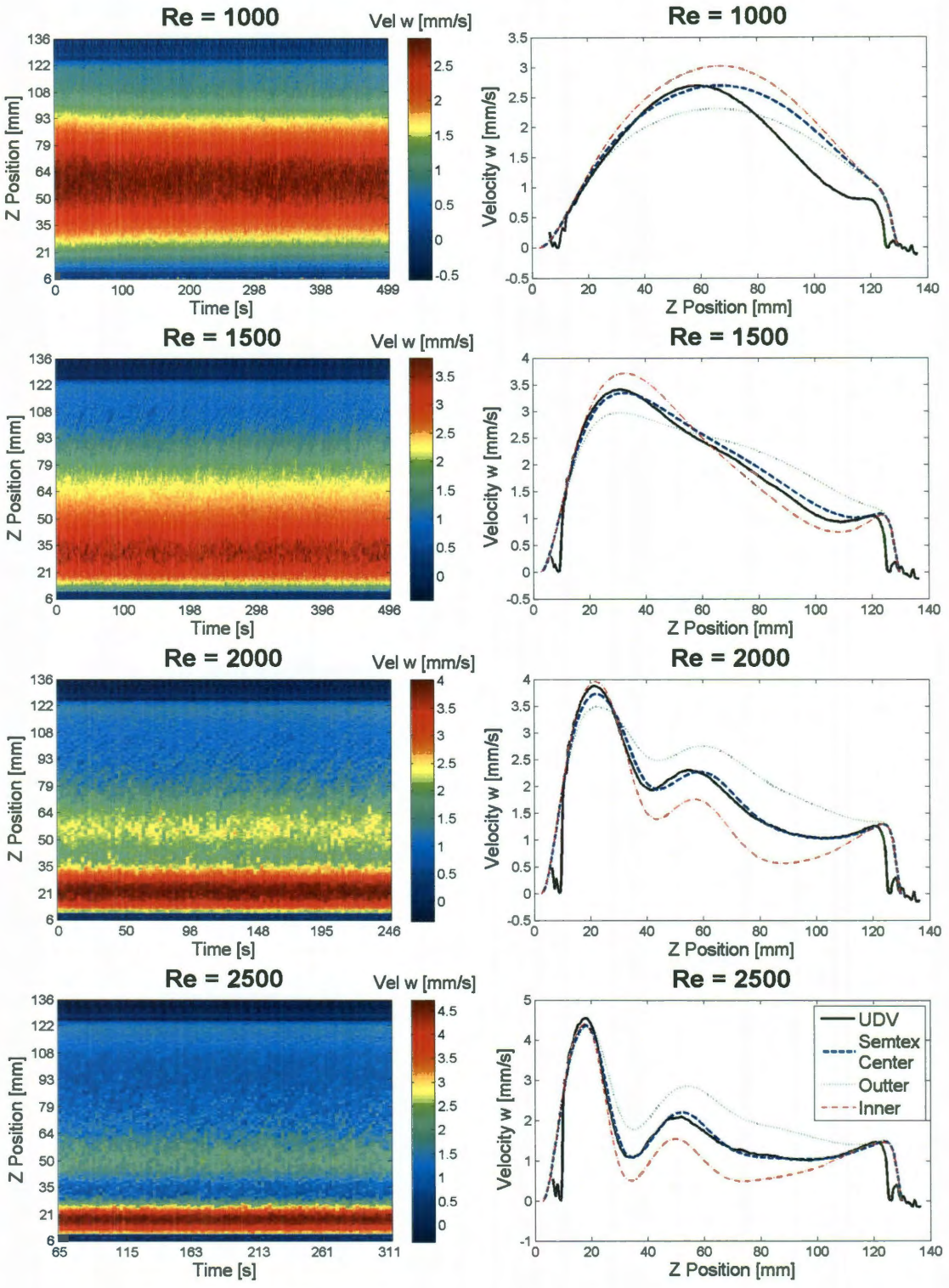

Figure 4.17 – Time-profile and average-profile plots for $r = 0.25$ offset 20% glycerin-water by volume

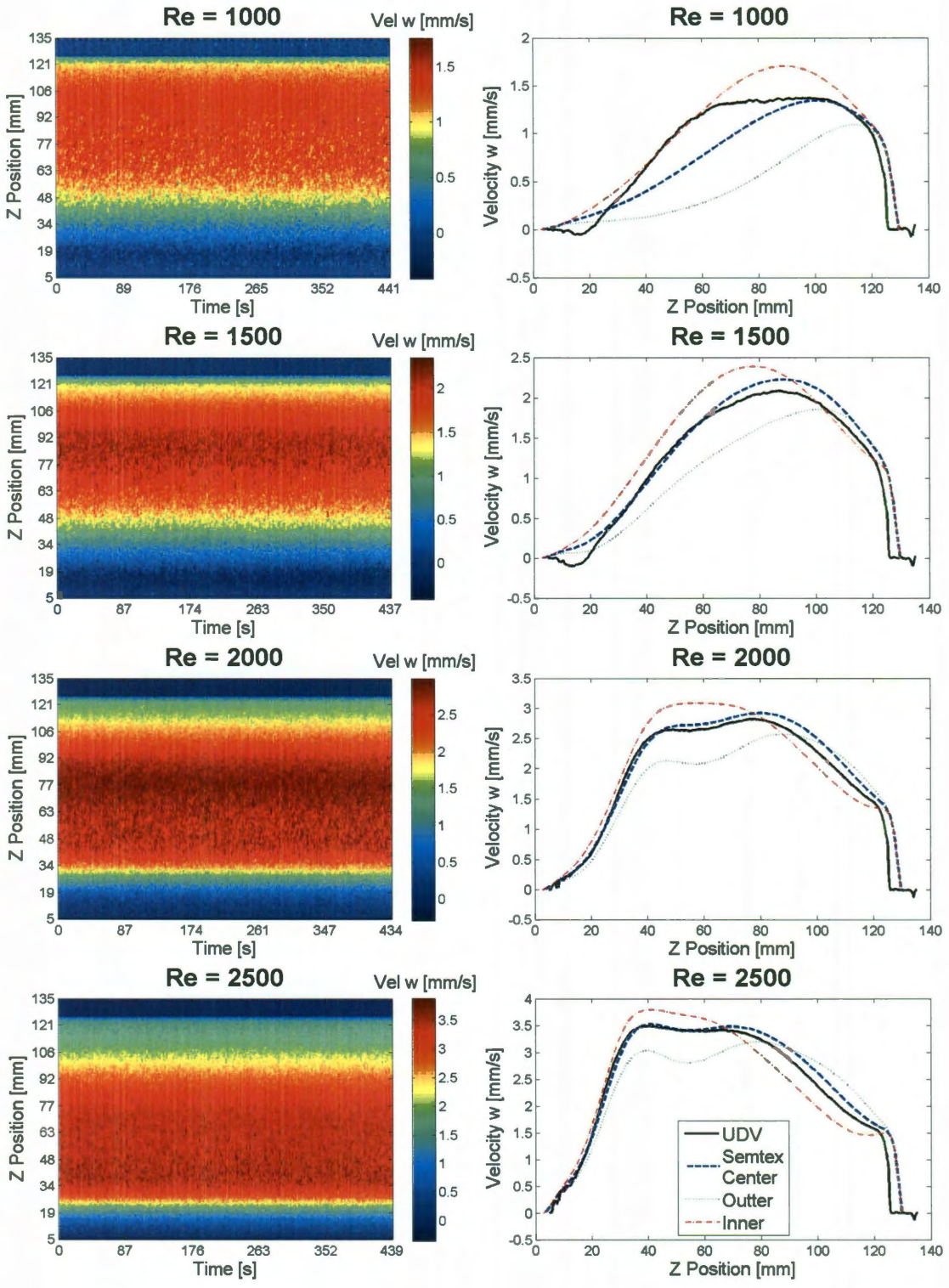

Figure 4.18 – Time-profile and average-profile plots for $r = 0.5$ offset 20% glycerin-water by volume

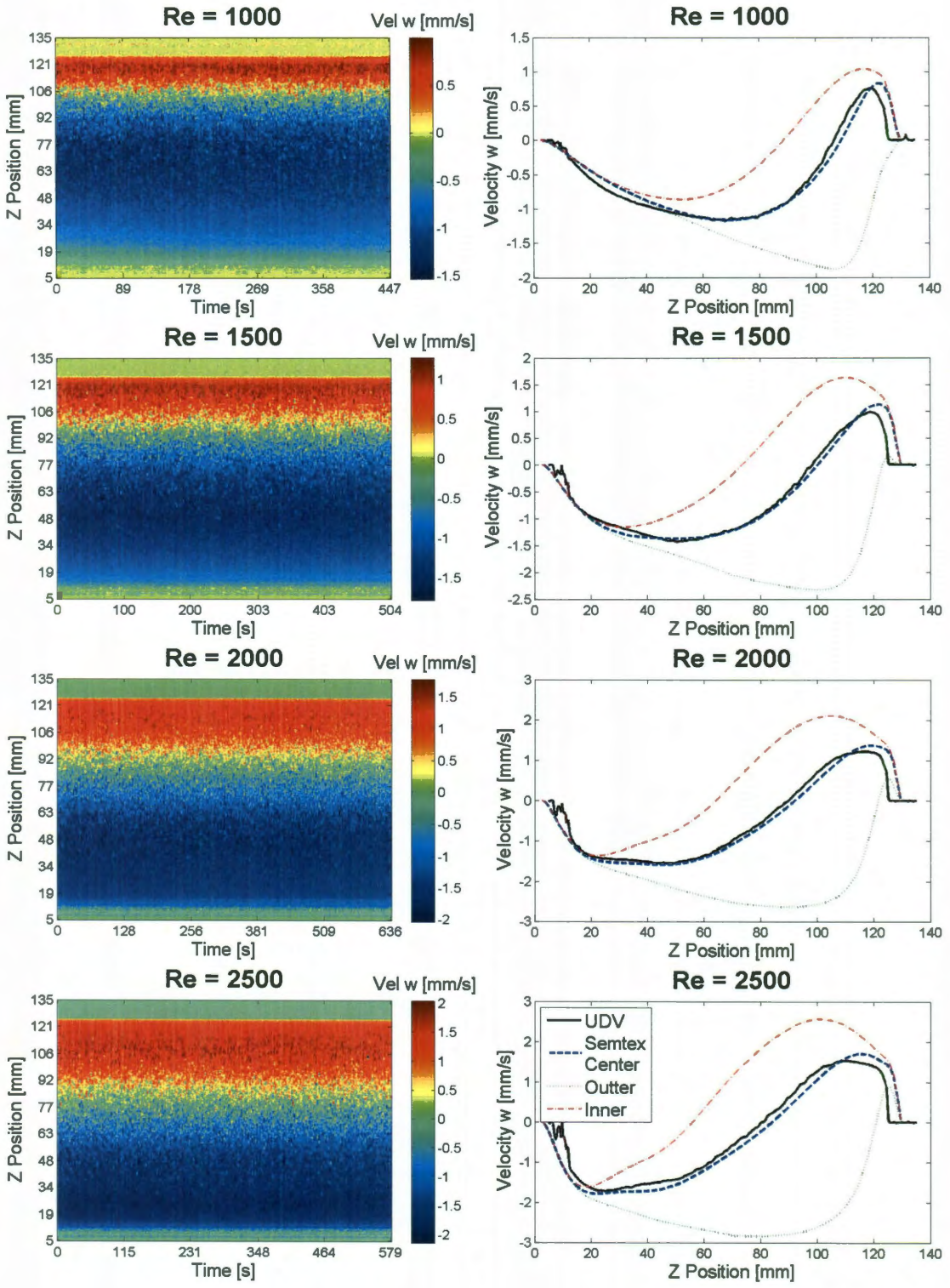

Figure 4.19 – Time-profile and average-profile plots for $r = 0.75$ offset 20% glycerin-water by volume

The experimental measurements with the UDV for the 20% glycerin-water solution match up extremely well with velocity profiles extracted from numerical simulations. It is still observed that agreement improves with increased Reynolds number as the few profiles that did not match well all occurred at $Re = 1000$. This suggests that the flow was not given enough time to bypass the initial transients as it was ramped up to $Re = 1000$.

The overall amount of noise in the measured velocity profiles was also greatly reduced compared to the water experiments. This is likely the result of a combination of better bead suspension, longer acquisition times, and higher overall fluid velocity.

There are also a few fluid artifacts in the $Re = 2000$ and $Re = 2500$ cases at $r = 0$. In particular there is a cusp in velocity at 80 mm. It is unclear whether these artifacts are manifestations of the UDV measurement or whether they are physical. The artifacts were reproducible under those specific conditions but were unobserved at any other offset or Reynolds number.

In the average-profile plots, a consistent difference between the length of the fluid domain measured by the UDV and the actual fluid domain that is represented by scaled numerical simulation results is observed. This is likely caused by an error in the acoustic velocity that was provided as an input to the UDV. Although this would also introduce a small velocity bias, the difference is small enough to be neglected.

4.3.2. Experimental Results $Re = 3000$

The critical Reynolds number for the axisymmetric, periodic instability is predicted to be $Re \approx 2700$. Thus the run at $Re = 3000$ is expected to be axisymmetric and time-periodic as observed in the numerical simulations (Section 4.1.4). However, experimental results at $Re = 3000$ with the 20% glycerin-water solution for $\gamma = 2.5$ were generally steady and did not show strong signs of periodicity. Table 4.6 shows a summary of the data presented.

Summary of Data Collected			
Radial Offset	**Reynolds Number**	**UDV Profile Acquisition Time [s]**	**Number of Profiles Collected**
	3000	2.51	199
$r^* = 0.0127\ m$	3000	2.51	200
$r = 0.25$	3000	2.51	252
	3000	1.67	212

Table 4.6 – Summary of data collected above critical Reynolds number

Time-profile and average-profile plots are shown in Figure 4.20. However, since the numerical simulations are periodic, to compare to the experiments which appear steady, the average velocity profile over 5 periods of the instability are averaged and plotted in the average-profile plot. A time-profile plot of the numerical simulation that shows the periodic behavior can be found in Figure 4.9.

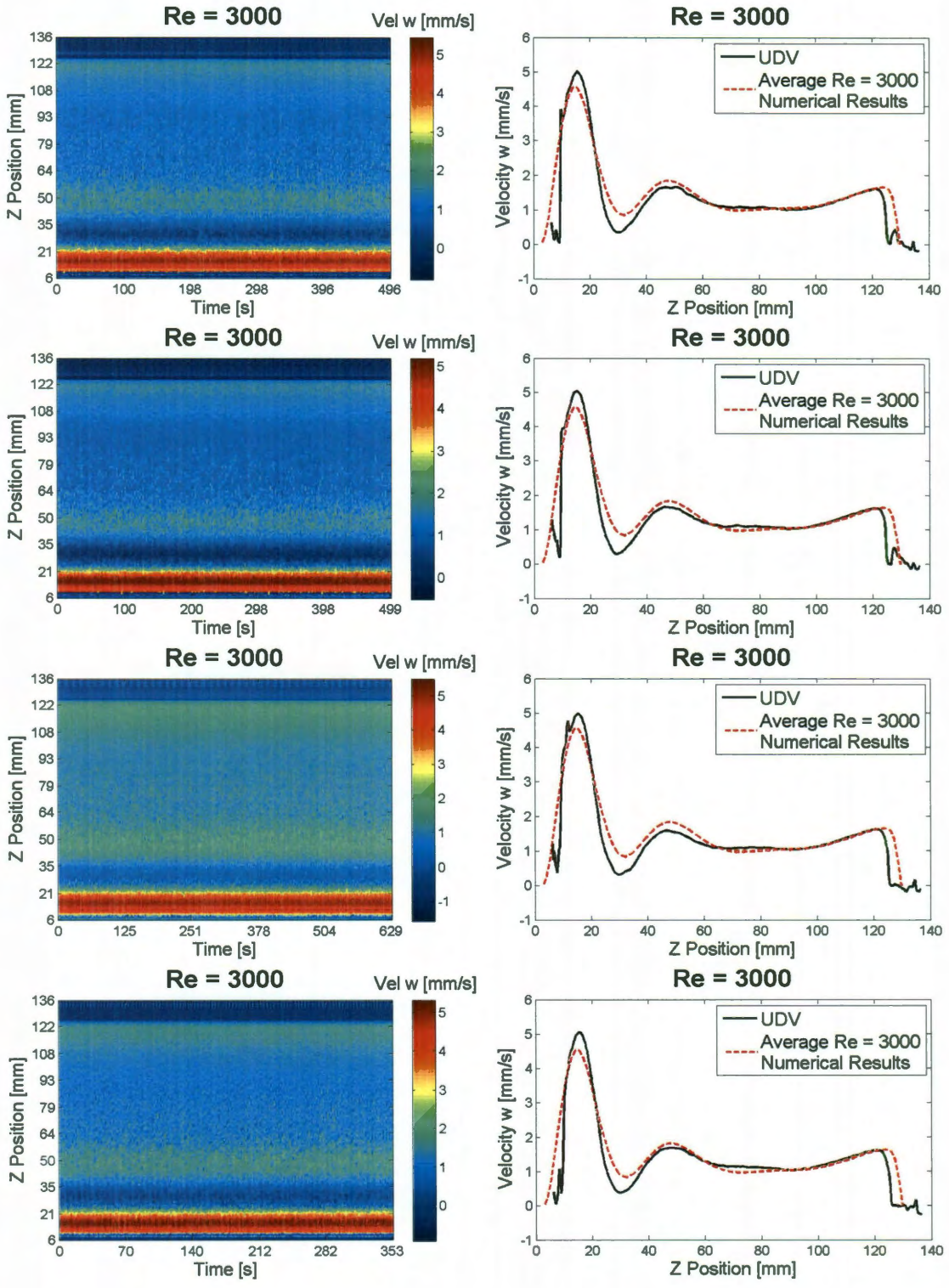

Figure 4.20 – Various $Re = 3000$ runs with $r = 0.25$ offset

The data collected shows that although the flow is not periodic as predicted, the overall shape of the flow field is not significantly different than the average of the periodic flow field predicted by numerical simulations. The four different data sets at $Re = 3000$ collected over multiple days also demonstrate that this steady flow field is very reproducible.

One possible explanation for the observation of a steady flow would be that the periodic behavior was on a short time scale and the UDV was averaging out the periodicity, resulting in an apparent steady velocity profile in time. Sample calculations were performed to determine the expected period of the instability based on the non-dimensional frequency predicted by the numerical simulations and supported by published results.

$$Re = \frac{\Omega R^2}{\nu}$$

$$3000 = \frac{\Omega_{Re=3000}(0.0508^2)}{1.72 \times 10^{-6}}$$

$$\Omega_{Re=3000} = 1.9995 \frac{rad}{s}$$

$$\omega = \frac{2\pi f}{\Omega} = 0.172$$

$$f_{predicted} = \frac{(0.172)(1.9995)}{2\pi} = 0.0547\ Hz$$

$$P = \frac{1}{f_{predicted}} = \frac{1}{0.0547} = 18.27\ s$$

The periodic instability is predicted to have a period of approximately 18 seconds on the experimental setup. Thus with an acquisition time of 2.51 seconds used in most of the runs at $Re = 3000$ (see Table 4.6), there would be approximately 7 velocity profiles within a period of the instability. This demonstrates that either the instability that is predicted to occur is not present or occurring a much higher frequency that exceeds the temporal resolution of the UDV.

Thus to summarize the data that has been presented thus far for the 20% glycerin-water mixture, measurements performed with the UDV below the critical Reynolds number were steady and matched well with results from numerical simulation. However, above the critical Reynolds number, numerical simulations predict a periodic instability but the UDV measurements still show a steady flow field. It might be suggested that the periodic instability predicted by numerical simulations was not being triggered. However, the steady velocity profile measured at $Re = 3000$ was not sensitive to large nonlinear external perturbations and did not show any signs of hysteresis. It also appeared unlikely that the temporal resolution of the UDV was insufficient to resolve the instability since the predicted period of the instability is on the order of 18 seconds, 7 times longer than the sampling rate of the UDV.

4.3.3. Periodic Experimental Results At $Re = 2000$ and $Re = 2500$

Experimental results were generally very reproducible and fairly consistent between tests run, especially for the glycerin-water solution. However, there were a few cases where periodic flow was observed at $Re = 2000$ and $Re = 2500$ for the 20% glycerin-water solution and these were only reproducible under very specific conditions. These periodic results were observed only when a new batch of the 20% glycerin-water solution was first mixed and tested. If the solution was allowed to sit overnight, testing with the solution the following day would be consistent with results seen in Sections 4.3.1 and 4.3.2. Table 4.7 shows a summary of the runs presented. Figure 4.21 shows two time-profile plots for $Re = 2000$ and $Re = 2500$ on the left and right respectively. Below these are average-profile plots comparing the averaged periodic experimental flow to the steady numerical simulations.

Summary of Data Collected, 20% Glycerin-Water Solution $R^* = 0.0508\,m \quad H^* = 0.127\,m \quad \gamma = 2.5$ $\nu = 1.72 \times 10^{-6}$			
Radial Offset	**Reynolds Number**	**UDV Profile Acquisition Time** $[s]$	**Number of Profiles Collected**
	2000	2.51	243
$r^* = 0.0127\,m$	2000	2.51	250
$r = 0.25$	2500	2.51	199
	2500	1.67	200

Table 4.7 – Summary of periodic experimental results at $Re = 2000$ and $Re = 2500$

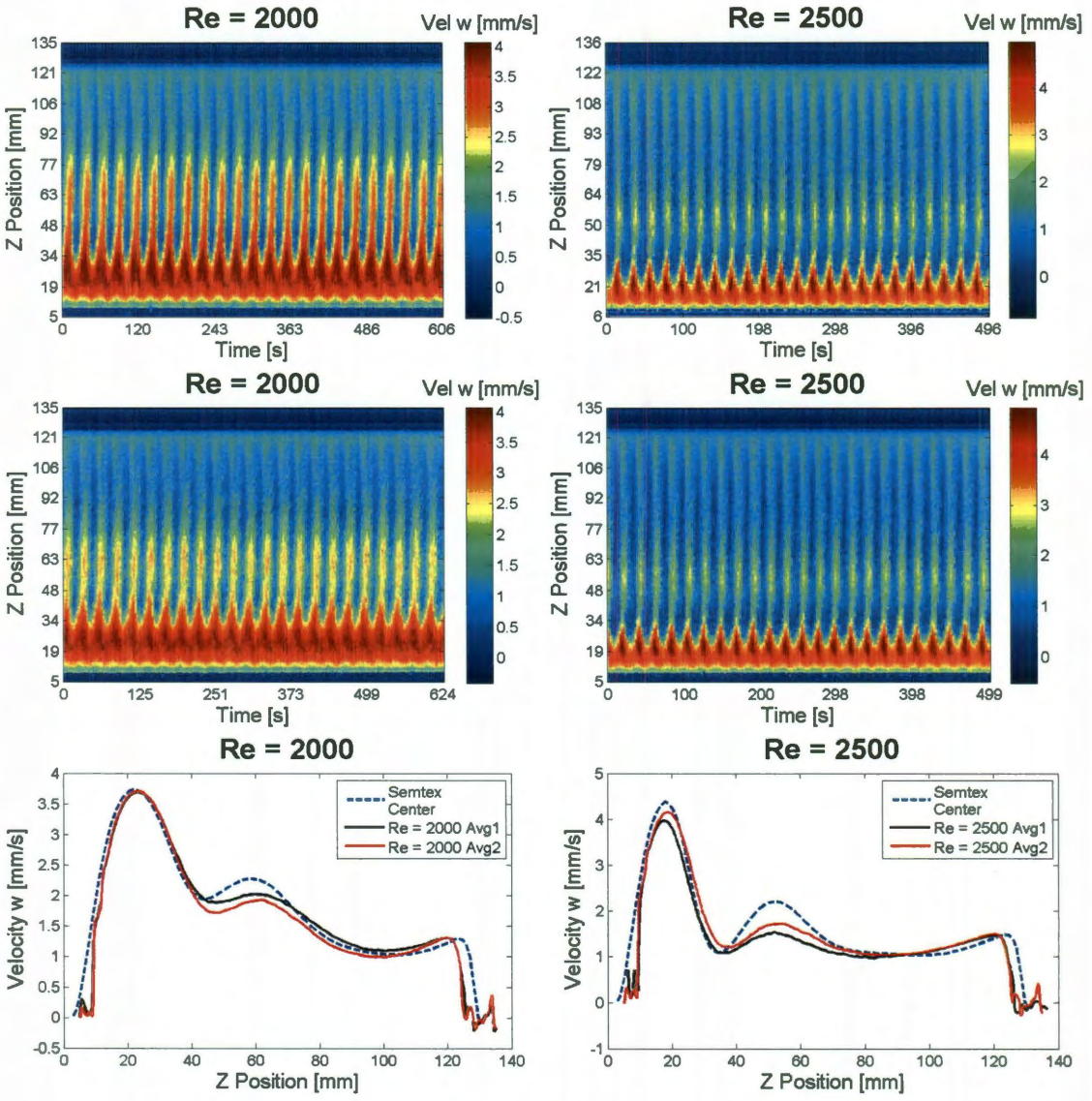

Figure 4.21 – Periodic experimental results for $r = 0.25$ offset at $Re = 2000$ and $Re = 2500$ for glycerin-water solution

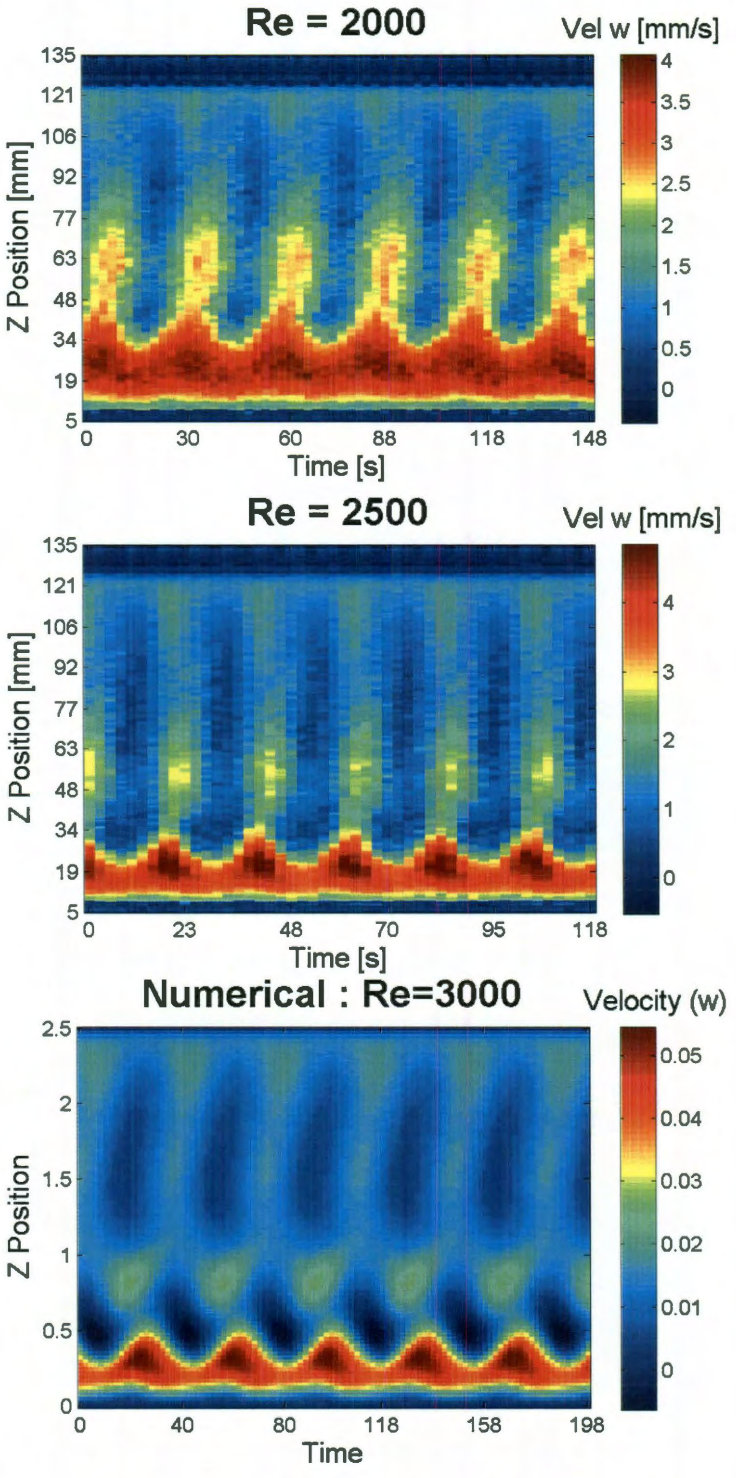

Figure 4.22 – Comparison between periodic $Re = 2000$ and $Re = 2500$ results with numerical $Re = 3000$ results

Figure 4.22 shows time-profile plots of the periodic $Re = 2000$ and $Re = 2500$ experimental results compared to the periodic $Re = 3000$ results from numerical simulations. The data has been cropped so that each plot displays the same amount of non-dimensional time. The non-dimensional frequency of the periodicity observed experimentally is computed using an FFT, as described in Section 4.1.4 and is summarized in Table 4.8.

Reynolds Number	Dimensional Frequency $[Hz]$	$\Omega \left[\frac{rad}{s}\right]$	Non-dimensional Frequency
$Re = 2000$	0.0374	1.333	0.1763
$Re = 2500$	0.0468	1.666	0.1765
Numerical $Re = 3000$	0.0273	1.0	0.1715

Table 4.8 – Frequency of experimentally observed periodicity

The observed non-dimensional frequency is very similar to that of the instability that is predicted at $Re_{cr} = 2700$ and the time-profile plots also look qualitatively similar, especially the experimental measurements at $Re = 2500$ and the numerical results at $Re = 3000$. Once the experimental Reynolds number is increased to 3000 the periodicity disappears and a velocity profile similar to the results from Section 4.3.2 is observed. This suggests that the periodicity observed at $Re = 2000$ and $Re = 2500$ for these special cases is caused by the predicted instability at $Re = 2700$.

It should be noted that the periodic behavior at $Re = 2000$ to $Re = 2500$ is only observed during the first day of testing when a new batch of the glycerin-water solution is prepared. The results are not reproducible the next day with the same solution but are reproducible if a new batch of glycerin-water solution is prepared each day. The reason for this inconsistency is unknown. It was initially thought that non-uniform mixing of the solution may be the cause. However, batches mixed with a magnetic stirrer for 20 minutes, manual mixing with a stirring rod, and automated stirring all led to periodic behavior on the first day (as observed in this section) and steady behavior on subsequent days (as observed in Sections 4.3.1 and 4.3.2).

4.3.4. Experimental Results Side Mounted UDV Probes

Experimental data was also collected from UDV probes mounted to the side of the fluid container. The UDV probe is mounted perpendicularly to the flat bevel that is offset at 1.25 inches from the center of the cylinder (see Part 1 in Appendix A). A description of how the probe is mounted can be found in Section 3.1.2. Two different heights were chosen and a summary of the data presented is shown in Table 4.9.

Bevel Offset	Height	Reynolds Number	UDV Acquisition Time [s]	Number of Profiles
1.25 *inches*	$h^* = 1.5$ *inches* $h = 0.75$	1000	1.17	212
		1500	1.17	277
		2000	1.17	240
		2500	1.17	436
1.25 *inches*	$h^* = 4$ *inches* $h = 2$	1000	2.51	219
		1500	2.51	210
		2000	2.00	210
		2500	2.00	223

Table 4.9 – Summary of data presented for side mounted UDV probe

Determining the actual velocity component being measured by the side mounted UDV probe, so that it can be extracted from numerical simulations for comparison, is more complicated than for the bottom mounted probe. In the bottom-mounted probe configuration, the velocity measured by the UDV is the axial velocity, *w*. In the side-mounted probe configuration, the velocity measured is the component parallel to a chord of the cylinder. Figure 4.23 shows the path of the UDV beam. Since the ultrasonic pulse is a wave, it is subject to refraction as it crosses interfaces. The UDV probe is mounted perpendicular to the flat bevel machined into the cylinder and travels through the acrylic along the path A-B. If the acoustic speed in the acrylic container and the working fluid were the same, the ultrasonic pulse would continue along path B-C. However, since the acoustic speed is different, the beam will refract and travel along some other path, for example B-D.

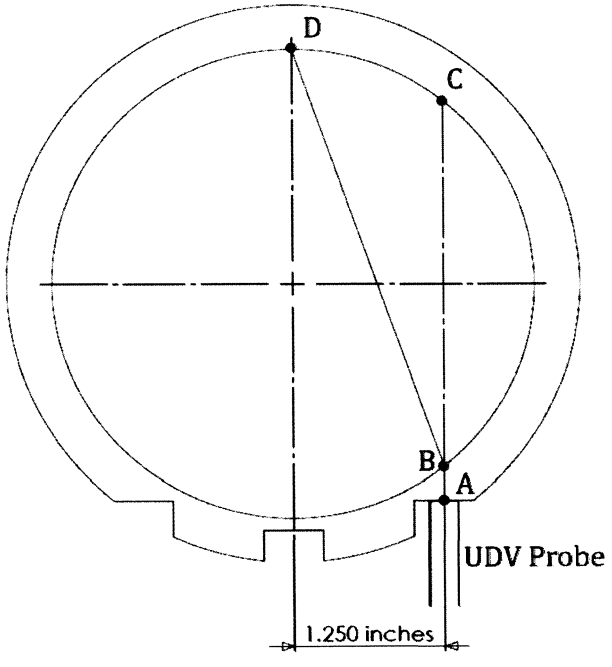

Figure 4.23 – Path of UDV beam in side mounted configuration

With no refraction, the radial offset of the chord B-C is easily determined to be equal to the radial offset of the probe (1.25 inches). However, since it is very unlikely that the acoustic speed in the fluid container will match the acoustic speed in the working fluid, a method for experimentally determining the radial offset of path B-D was developed.

A UDV beam finder (Part 39 in Appendix A) was fabricated. The UDV beam finder attaches to the output shaft of the motor like the rotating lid, but allows a vertical stainless steel rod to be swept around the inner circle of the cylindrical fluid container (See drawing 2/2 for part 39). As the metal rod crosses the path of the ultrasonic beam, a sharp spike can be observed in the echo profile of the UDV. Since the UDV beam finder is attached to the motor assembly, its angular position can be precisely determined through encoder readings. Thus the following strategy can be used to determine the precise location of the UDV beam even after it refracts as it crosses the acrylic/fluid interface.

Figure 4.24 shows a top-down view of the fluid container and demonstrates how the UDV beam finder is used to determine the location of the UDV beam. R^* denotes the inner radius of the cylinder, R_{sweep} is the sweep radius of the vertical rod on the UDV beam finder (1.75 *inches*), and O marks the center of the fluid container. The outer diameter of the cylinder is not pictured. The thick black line extending from the UDV probe marks the path of the UDV beam as it travels through the acrylic, refracts across the acrylic/fluid interface, and continues on to the other acrylic surface. The dotted circular line marks the path that the rod on the UDV

beam finder will travel as it is rotated. The encoder readings are initialized to zero at some reference location marked, in this case, by the short dotted line extending from *O* downward. The shaft of the motor is then rotated manually until the metal rod of the UDV beam finder comes in contact with the UDV beam at A. A large spike is observed on the echo profile indicating to the user that this has occurred. An encoder reading is taken at this point and the angle θ_1 can be computed. The shaft of the motor is rotated again until the rod contacts the UDV beam at B, again indicated by a spike in the echo profile this time at a different location. An encoder reading is made and angle θ_2 can be computed.

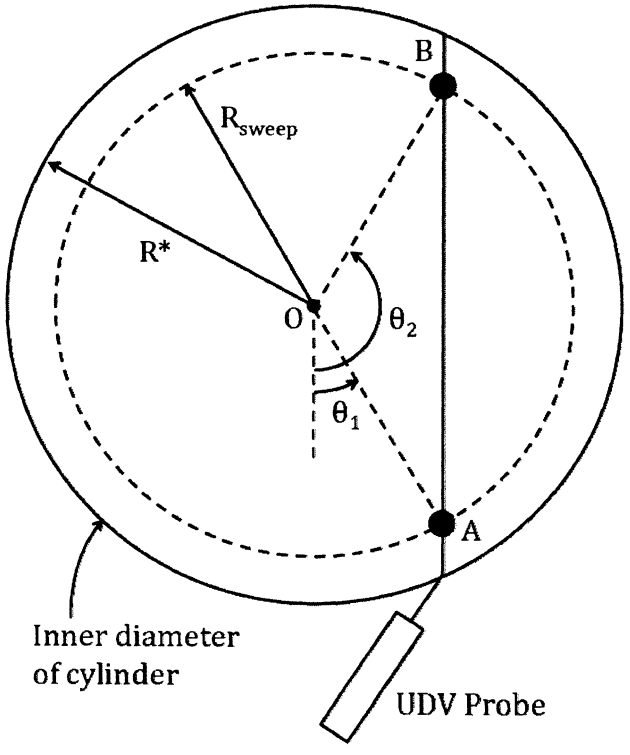

Figure 4.24 – Determining UDV beam location using UDV beam finder

The offset of the chord followed by the UDV beam can now be computed through geometry as shown in Figure 4.25. The difference between the two angle measurements can be computed and with knowledge of the sweep radius, R_{sweep}, the radial offset (length O-C) of the chord followed by the UDV beam (A-B) can be computed as:

$$OC = R_{sweep} \times \cos\left(\frac{\Delta\theta}{2}\right)$$

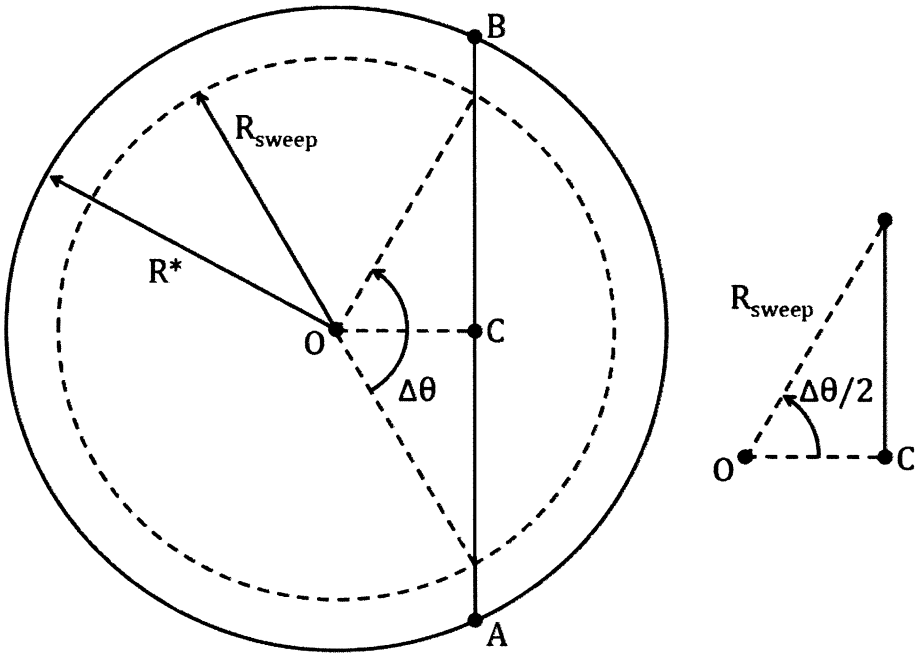

Figure 4.25 – Computing the offset of chord followed by UDV beam

For the 1.25 inch offset bevel, the distance O-C was computed to be 0.74 inches or 0.37 in non-dimensional terms. This was used to extract data from numerical simulations for comparison with experimental results at two different axial heights, and the results are shown in Figure 4.26 and Figure 4.27.

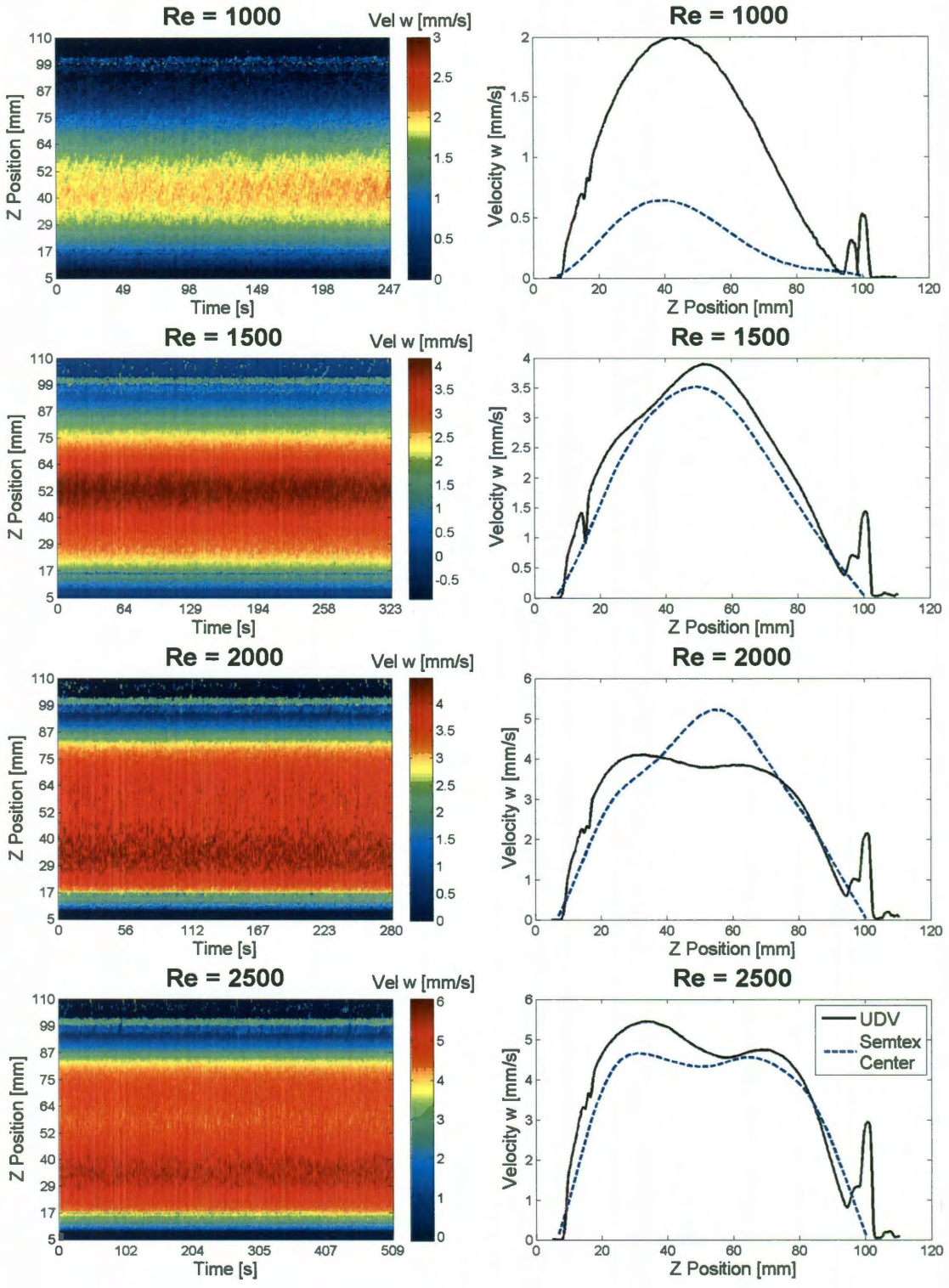

Figure 4.26 – Plots for 1.25 inch offset side bevel at $h^* = 1.5\ inch$, $h = 0.75$

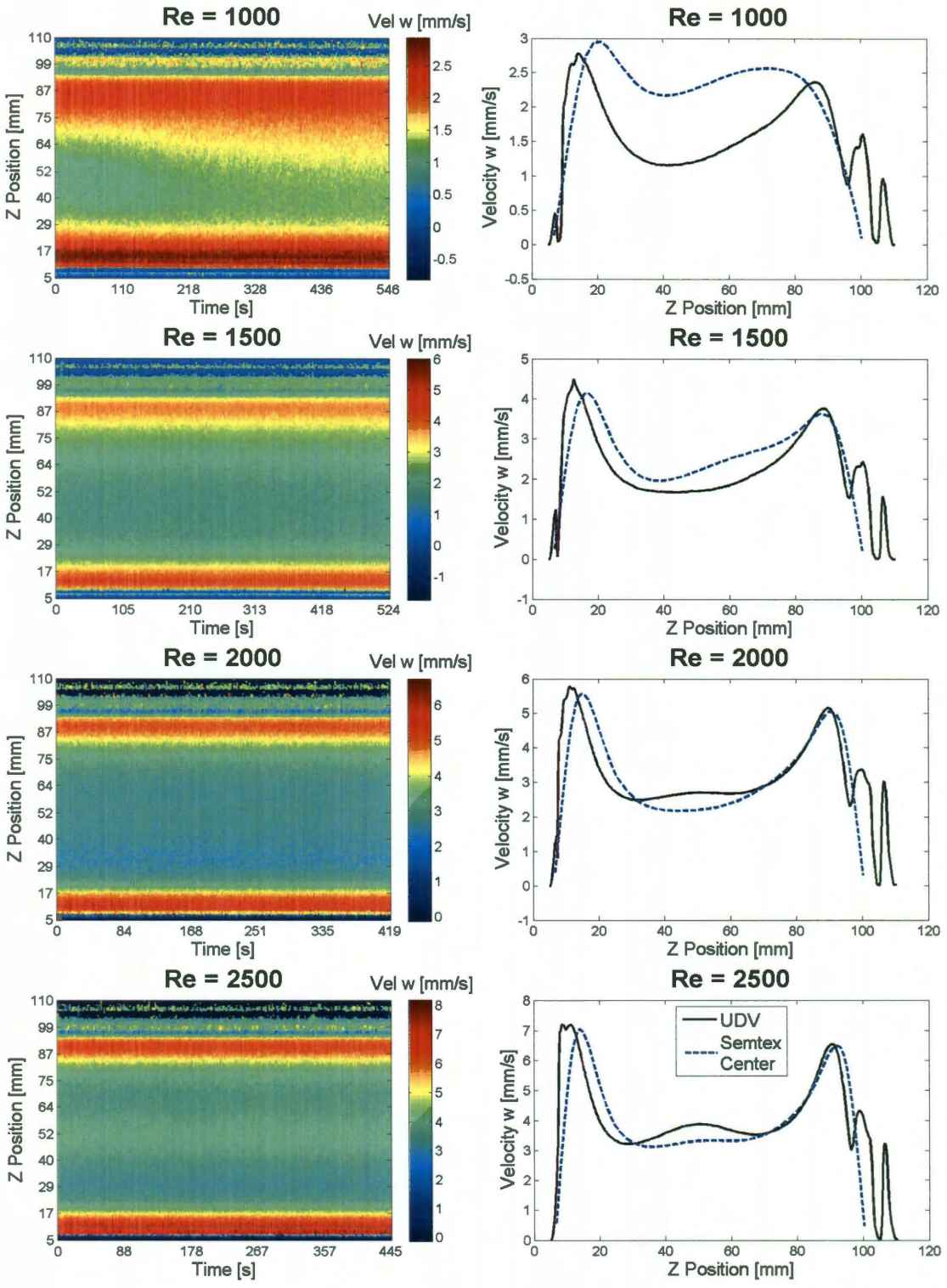

Figure 4.27 – Plots for 1.25 inch offset side bevel at $h^* = 4\ inch, h = 2$

4.3.5. Calculation of Stokes Number

To help explain some of the observations in the experimental measurements, the particle Reynolds number and the Stokes number for the particle are computed. The particle Reynolds number (Re_p) is given by:

$$Re_p = \frac{V d_p}{\nu}, \tag{4.1}$$

where V is the mean velocity of the flow, d_p is the diameter of the particle, and ν is the kinematic viscosity. Assuming a mean velocity of $10\frac{mm}{s}$ and using the larger particle diameter (80 μm) in the range, the particle Reynolds number in the 20% glycerin-water solution is computed to be:

$$Re_p = \frac{\left(0.01\frac{m}{s}\right)(80 \times 10^{-6}\, m)}{1.72 \times 10^{-6}\frac{m^2}{s}} = 0.465\,.$$

Stokes drag law can be applied to particles when the particle Reynolds number is less than unity. Using this result, the particle response, τ_p, time can be computed as:

$$\tau_p = \frac{d_p^2 \rho_p}{18\mu}, \tag{4.2}$$

where ρ_p is the density of the particle and μ is the dynamic viscosity of the fluid. Computing the particle response time for the particles gives:

$$\tau_p = \frac{(80 \times 10^{-6} m)^2 \left(1000\frac{kg}{m^3}\right)}{18\left(0.0018276\frac{Ns}{m^2}\right)} = 0.0001945\ s$$

The Stokes number can be taken as the ratio between the response time of the particle and the Kolmogorov time scale for turbulent flow. The Kolmogorov time scale, τ_k, is computed as:

$$\tau_k = \left(\frac{\nu}{\epsilon}\right)^{\frac{1}{2}},$$

where ϵ is the average rate of energy dissipation per unit mass. Estimating approximately 1.029 liters of the 20% glycerin-water solution, and a dissipated energy of 1 watt, the Kolmogorov time scale is computed as:

$$\tau_k = \left(\frac{1.72 \times 10^{-6}\frac{m^2}{s}}{1\frac{kgm^2}{s^3}} \times 1.060\frac{kg}{L} \times 1.029\,L\right)^{\frac{1}{2}} = 0.00137\ s.$$

This results in a Stokes number, St, of:

$$St = \frac{\tau_p}{\tau_k} = \frac{0.0001945}{0.00137} = 0.142\,.$$

The smaller the Stokes number, the more the particles behave like ideal tracers of the flow. The above calculations show that the particles used for the experiments are able to track the flow, even if it becomes turbulent. However, since the Kolmogorov time scale is so small, there is insufficient temporal resolution in the UDV to resolve the turbulent flow. If the UDV is used to measure the turbulent flow, only a Reynolds averaged flow field will be computed. It is believed that localized turbulence accounts for the inability to observe periodic flow with the UDV at Re = 3000.

Chapter 5

Conclusions and Future Work

5.1. Conclusions

An experimental setup for a rotating lid-driven cylinder configuration is designed and constructed as a benchtop-scale experimental model of the traveling heater crystal growth method. Associated techniques for accomplishing fluid flow measurements using Ultrasonic Doppler Velocimetry are also developed and documented. Experiments with water and a 20% glycerin-water solution by volume are carried out to test the viability of using Ultrasonic Doppler Velocimetry as a non-invasive form of flow visualization. The long-term goal is to use UDV for flow visualization in optically opaque fluids such as liquid metals and molten semiconductors.

Experimental measurements and numerical simulations of the flow field in a rotating lid-driven cylinder with aspect ratio $\gamma = 2.5$ are presented for low to

moderate Reynolds numbers ($Re = 1000$ to $Re = 3000$). Numerical simulations were carried out with an existing open-source spectral-element computational fluid dynamics code and results obtained were in good agreement with published results. The flow is expected to be steady and axisymmetric below the critical Reynolds number of $Re = 2700$ and transitions to an axisymmetric, periodic flow in the range of $Re = 2700$ to $Re = 3300$. Good agreement between experimental measurements and numerical simulations were observed for flows below the critical Reynolds number in the range of $Re = 1000$ to $Re = 2500$.

Above the critical Reynolds number, the instability was not observed experimentally. In special circumstances, a periodic flow very similar to the numerically predicted instability is observed at Reynolds numbers below the critical values. These flows were sometimes observed at $Re = 2000$ and $Re = 2500$.

Based on the experimental observations, it is believed that the inconsistencies between experimental results and numerical simulations are caused by localized turbulence. It is unlikely that the instability at $Re = 2700$ would fail to trigger in the experimental setup since the instability has already been observed experimentally by laser Doppler velocimetry in more viscous fluids (Sørensen *et al.* 2006). Instead, it is speculated that regions of localized turbulence in the flow field prevent the periodic instability from becoming dominant. Analysis of the tracer particles used in experiments suggest that the particles would be able to track the turbulent eddies. However, the averaging effect of the Ultrasonic Doppler Velocimetry technique would make any turbulence unobservable, since the flow

would be changing on a much faster time-scale. Under these conditions, time-averaged localized turbulence would appear steady, as in the Reynolds-Averaged Navier Stokes (RANS) formulation. The results from Section 4.3.2 support this theory and suggest that the UDV is observing a Reynolds averaged turbulent flow field at $Re = 3000$.

The periodic results occurring below the critical Reynolds number are only observable when a new batch of the glycerin-water solution is mixed. It is believed that for these cases, the instability at $Re = 2700$ is being triggered early and is observable between $Re = 2000$ and $Re = 2500$. Above $Re = 3000$, the flow again becomes turbulent and the UDV observes a steady, Reynolds-averaged flow field. It is unclear why different results are observed between test runs with new batches of glycerin-water solutions versus a batch of solution that has been used for a few days. This was observed without correlation to mixing procedures and ramping of the motor speed.

The experiments also revealed some strengths and weaknesses of Ultrasonic Doppler Velocimetry. For the strengths, the experiments demonstrated that the UDV can be used to obtain time accurate flow visualizations in real-time. By adjusting the pulse repetition frequency, the UDV was able to accomplish flow measurements that were accurate on the order of mm/s. It is non-invasive and the measurement probe can be placed external to the flow. The UDV can also be used with optically opaque working fluids provided suitable seed particles, either natural

or artificial, are present or available. Although deviation of the ultrasonic beam was initially a concern, its effects on the overall accuracy of the UDV are minimal.

One major weakness of Ultrasonic Doppler Velocimetry as the sole flow visualization technique is that only the velocity component parallel to a line, along a line can be resolved with a single probe. Without using numerical simulations as a road map, it would be very difficult to deduce the entire flow field from a few isolated UDV measurements. Although multiple probes or tests can be performed in a raster pattern in an effort to generate a complete flow field, this would be very tedious and time-consuming. The other major weakness of the UDV is the need for particles in the flow that are able to reflect the ultrasonic pulses. Control of the suspension, size, and concentration of these particles are crucial to obtaining accurate, noise-free measurements from the UDV. Lastly, although the UDV appears to perform well for laminar flows, its heavy reliance on statistical correlation and averaging makes it suitable only for visualizing time-averaged turbulent flows.

5.2. Future Work

There are many possibilities for future work in this project. In the short term, a higher viscosity glycerin-water solution can be tested to investigate whether the higher viscosity can prevent the transition to turbulent flow and verify the local turbulence explanation of the results observed in this thesis. In the long term, additions to the experimental setup to perform stirring of the working fluid via a rotating magnetic field can be added. Challenges associated with using low melting

point liquid metals and other low viscosity fluids will also need to be overcome as the project moves toward the ultimate goal of a large-scale model to optimize the flow control techniques used in crystal growth experiments.

References

Blackburn, H. M., and S. J. Sherwin. 2004. "Formulation of a Galerkin spectral element-Fourier method for three-dimensional incompressible flows in cylindrical geometries." *Journal of Computational Physics* 197 (2) (July 1): 759-778. doi:16/j.jcp.2004.02.013.

Brito, Daniel, Henri-Claude Nataf, Philippe Cardin, Julien Aubert, and Jean-Paul Masson. 2001. "Ultrasonic Doppler velocimetry in liquid gallium." *Experiments in Fluids* 31 (6) (December): 653-663. doi:10.1007/s003480100312.

Cengel, Yunus, and John Cimbala. 2009. *Fluid Mechanics Fundamentals and Applications*. 2nd ed. McGraw-Hill Science/Engineering/Math, March 16.

Cheng, Nian-Sheng. 2008. "Formula for the Viscosity of a Glycerol–Water Mixture." *Industrial & Engineering Chemistry Research* 47 (9) (May 1): 3285-3288. doi:10.1021/ie071349z.

Chun, Ch.-H., and W. Wuest. 1982. "Suppression of temperature oscillations of thermal Marangoni convection in a floating zone by superimposing of rotating flows." *Acta Astronautica* 9 (4) (April): 225-230. doi:16/0094-5765(82)90025-X.

Davis, Kenneth E. 2011. Three-Dimensional, Time-Dependent SpectralElement Simulations of a Thermocapillary Liquid Bridge with Magnetic Stabilization. Rice University, April.

Dold, P. 2004. "Analysis of microsegregation in RF-heated float zone growth of silicon--comparison to the radiation-heated process." *Journal of Crystal Growth* 261 (1) (January 15): 1-10. doi:16/j.jcrysgro.2003.08.073.

Eckert, S., and G. Gerbeth. 2002. "Velocity measurements in liquid sodium by means of ultrasound Doppler velocimetry." *Experiments in Fluids* 32 (5) (May): 542-546. doi:10.1007/s00348-001-0380-9.

Eckert, S., G. Gerbeth, and V. I. Melnikov. 2003. "Velocity measurements at high temperatures by ultrasound Doppler velocimetry using an acoustic wave guide." *Experiments in Fluids* 35 (5) (November): 381-388. doi:10.1007/s00348-003-0606-0.

Escudier, M. P. 1984. "Observations of the flow produced in a cylindrical container by a rotating endwall." *Experiments in Fluids* 2 (4): 189-196. doi:10.1007/BF00571864.

Gelfgat, A. Yu., P. Z. Bar-Yoseph, and A. Solan. 1996. "Stability of Confined Swirling Flow with and Without Vortex Breakdown." *Journal of Fluid Mechanics* 311: 1-36. doi:10.1017/S0022112096002492.

GELFGAT, A. Yu., P. Z. BAR-YOSEPH, and A. SOLAN. 2001. "Three-Dimensional Instability of Axisymmetric Flow in a Rotating Lid–cylinder Enclosure." *Journal of Fluid Mechanics* 438: 363-377. doi:10.1017/S0022112001004566.

GRANTS, I., C. ZHANG, S. ECKERT, and G. GERBETH. 2008. "Experimental Observation of Swirl Accumulation in a Magnetically Driven Flow." *Journal of Fluid Mechanics* 616: 135-152. doi:10.1017/S0022112008003650.

Houchens, Brent C., Piotr Becla, Stephanie E. Tritchler, Andres J. Goza, and David F. Bliss. 2010. "Crystal growth of bulk ternary semiconductors: Comparison of GaInSb growth by horizontal Bridgman and horizontal traveling heater method." *Journal of Crystal Growth* 312 (8) (April 1): 1090-1094. doi:16/j.jcrysgro.2009.12.051.

Kármán, Th. V. 1921. "Über laminare und turbulente Reibung." *ZAMM - Journal of Applied Mathematics and Mechanics / Zeitschrift für Angewandte Mathematik und Mechanik* 1 (4) (January 1): 233-252. doi:10.1002/zamm.19210010401.

Lopez, J. M., and A. D. Perry. 1992. "Axisymmetric Vortex Breakdown. Part 3 Onset of Periodic Flow and Chaotic Advection." *Journal of Fluid Mechanics* 234: 449-471. doi:10.1017/S0022112092000867.

Messer, Matthias. Pulsed ultrasonic doppler velocimetry for measurement of velocity profiles in small channels and capplilaries. Thesis. http://smartech.gatech.edu/handle/1853/7644.

Roesner, K.G. 1990. Recirculation zones in a cylinder with rotating lid. In *Topological Fluid Mechanics*, 699-708. Cambridge University Press.

Ronnenberg, Burkhard. 1977. *Ein selbstjustierendes 3-Komponenten-Laserdoppleranemometer nach dem Vergleichsstrahlverfahren, angewandt für Untersuchungen in einer stationären zylindersymmetrischen Drehströmung mit einem.* Göttingen: Max-Planck-Inst. für Strömungsforschung.

Sørensen, Jens Nørkær, Igor Naumov, and Robert Mikkelsen. 2006. "Experimental investigation of three-dimensional flow instabilities in a rotating lid-driven

cavity." *Experiments in Fluids* 41 (3) (June): 425-440. doi:10.1007/s00348-006-0170-5.

SOTIROPOULOS, FOTIS, DONALD R. WEBSTER, and TAHIRIH C. LACKEY. 2002. "Experiments on Lagrangian Transport in Steady Vortex-Breakdown Bubbles in a Confined Swirling Flow." *Journal of Fluid Mechanics* 466: 215-248. doi:10.1017/S0022112002001271.

SPOHN, A., M. MORY, and E. J. HOPFINGER. 1998. "Experiments on Vortex Breakdown in a Confined Flow Generated by a Rotating Disc." *Journal of Fluid Mechanics* 370: 73-99. doi:null.

STEVENS, J. L., J. M. LOPEZ, and B. J. CANTWELL. 1999. "Oscillatory Flow States in an Enclosed Cylinder with a Rotating Endwall." *Journal of Fluid Mechanics* 389: 101-118. doi:null.

Takeda. 1999. "Ultrasonic Doppler method for velocity profile measurement in fluid dynamics and fluid engineering." *Experiments in Fluids* 26 (3) (February): 177-178. doi:10.1007/s003480050277.

Takeda, Y. 1991. "Development of an ultrasound velocity profile monitor." *Nuclear Engineering and Design* 126 (2) (April 2): 277-284. doi:16/0029-5493(91)90117-Z.

Vogel, Horst. 1968. *Experimentelle Ergebnisse über die laminare Strömung in einem zylindrischen Gehäuse mit darin rotierender Scheibe*. Göttingen: MPIStrömungsforschung.

Willemetz, Jean-Claude. *DOP3000 series, User's manual.* 1st ed. Software 3.02. Switzerland: SIGNAL PROCESSING S.A.

Appendix A

Parts and Assemblies List		
Part Number	**Description**	**Drawing**
1	Fluid Container	Yes
2	Fluid Container Top Plate	Yes
3	Motor Support Plate	Yes
4	Rotating Disk	Yes
5	Rotating Disk Shaft	Yes
6	Assembled Rotating Disk with Shaft (Parts 4 + 5)	Yes
7	Motor Assembly: Motor – Maxon A-max32 (236655) Gearbox – Maxon GP32A (166161) Encoder – Maxon ENC HEDS 5540 (110513)	Yes
8	Bottom Probe Holder	Yes
9	Side Probe – Support Plate	Yes
10	Side Probe – Base	Yes
11	Side Probe – Vertical Plate	Yes
12	Side Probe – Clamp Base	Yes
13	Side Probe – Clamp	Yes
14	Side Probe – Probe Spacer (8 mm)	Yes
15	Embedded Screw	Yes
16	Base with Embedded Screw (Parts 10 + 15)	Yes
17	Clamp Base with Embedded Screw (Parts 12 + 15)	Yes
18	UDV Probe (5 mm transducer, 4 MHz) – 8 mm OD	Yes
19	Side Probe Holder Assembly (Parts 9 – 18 and hardware)	Yes
20	Ball bearing – McMaster 57155K304 1/4" Shaft Diameter 1/2" x 1/8"	No

21	Shaft Coupler	Yes
22	Rubber O-Ring – ID 4.25" – OD 4.375" – MSC 75748202	No
23	5/16-18 threaded rod 9.5" long	No
24	5/16-18 threaded rod 12.25" long	No
25	Aluminum standoff 2.3125" long	Yes
26	Aluminum standoff 2" long	Yes
27	1/4" washer	No
28	1/4" wing nut	No
29	5/16" washer	No
30	5/16" wing nut	No
31	5/16" hex nut	No
32	M3 x 3mm flat head screw	No
33	#6-32 Allen head screw (various lengths)	No
34	#6-32 Allen head set screw	No
35	Motor/Lid Assembly	Yes
36	Fluid Container Assembly With Stilts	Yes
37	Full Assembly	Yes
38	Probe Alignment Block	Yes
39	UDV Beam Finder	Yes

General Construction Note

Although the nominal dimension on the thickness of the acrylic sheet stock is 0.5 inches, the actual measured thickness was 0.447 inches. In most cases any discrepancies in the thickness of the sheet stock is not significant. However, all dimensions marked as 0.447 inches in the drawings correspond to the thickness dimension of the stock acrylic sheets. This will aid in identifying which dimension of the piece aligned to the thickness of the acrylic sheet.

Part 1 - Fluid Container (1/2)		
Scale - 1:5	Material - Acrylic	Units - Inches

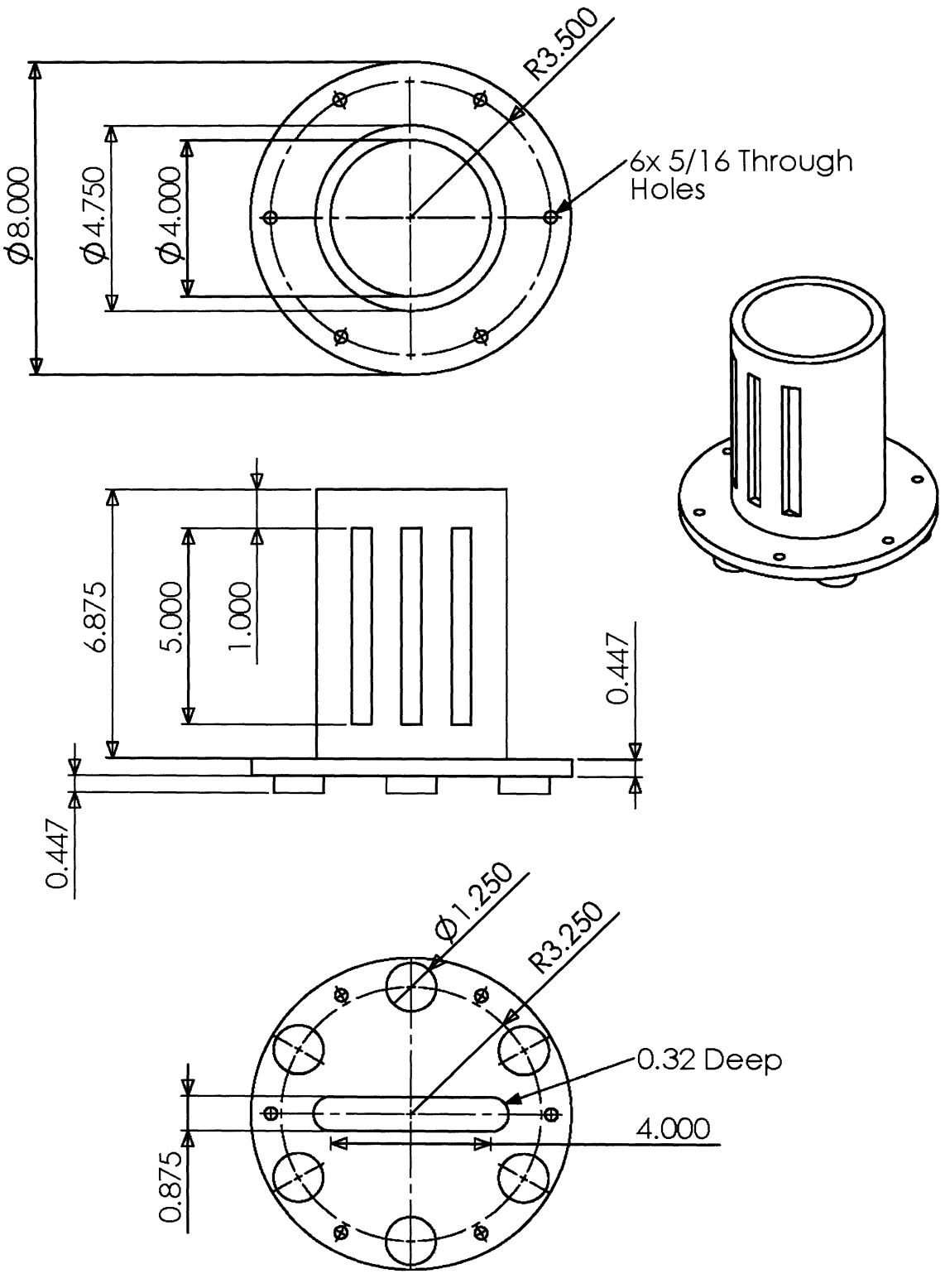

Part 1 - Fluid Container (2/2) - Section View of Cylinder		
Scale - 1:1	Material - Acrylic	Units - Inches

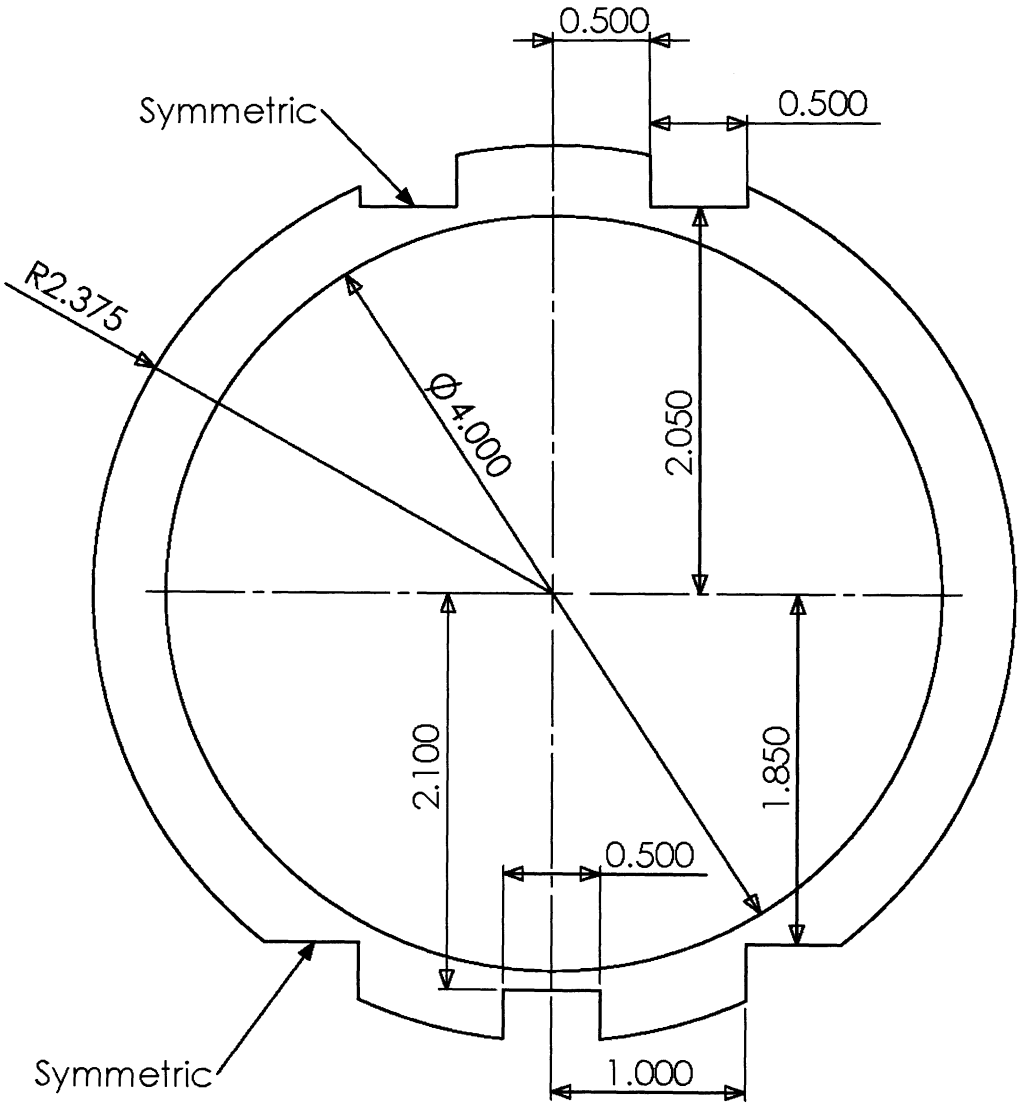

Part 2 - Fluid Container Top Plate		
Scale - 1:3	Material - Acrylic	Units - Inches

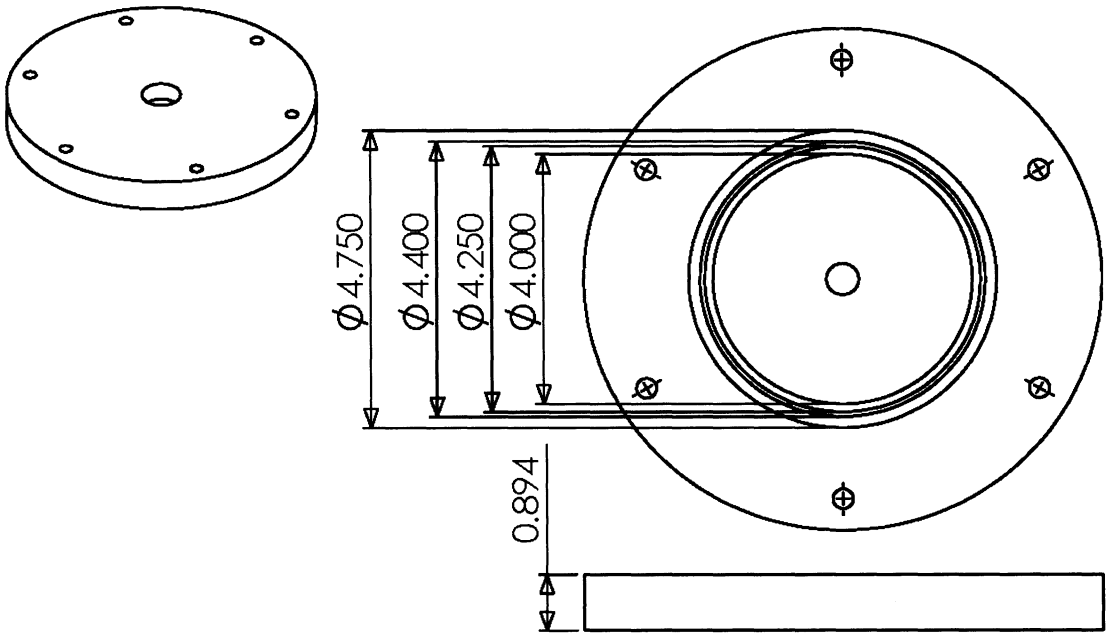

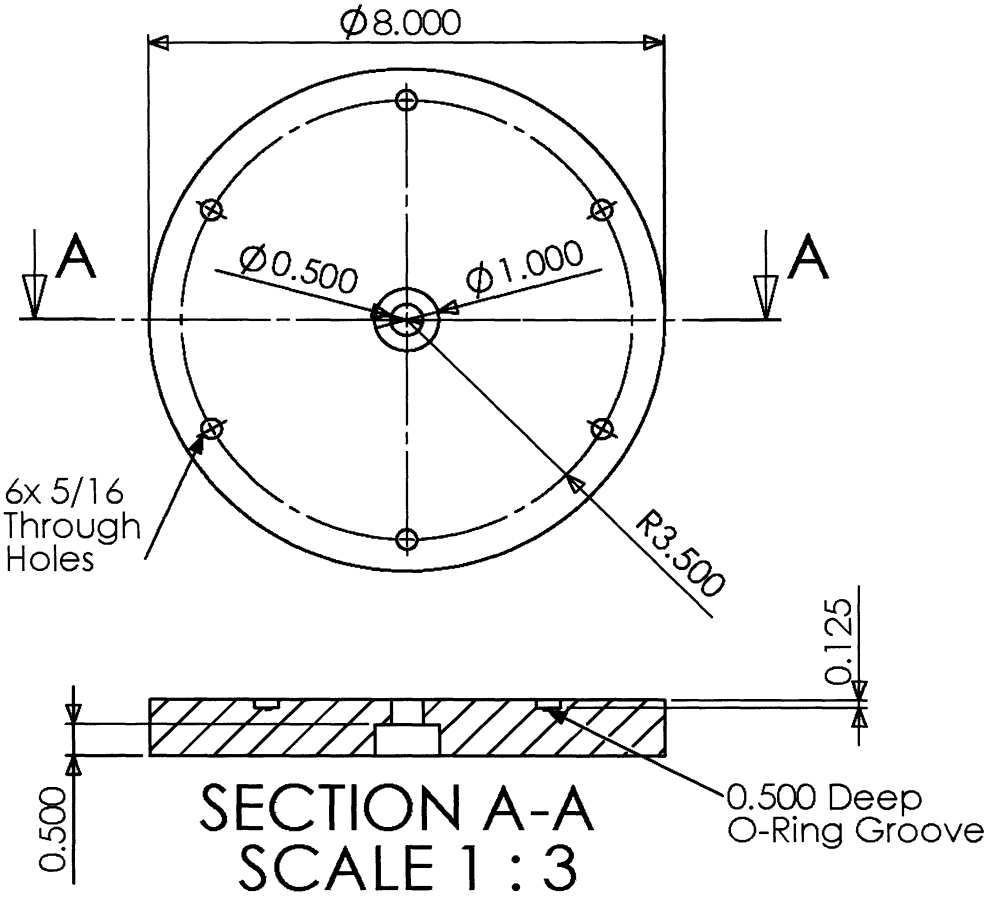

Part 3 - Motor Support Plate		
Scale - 1:2	Material - Aluminum	Units - Inches

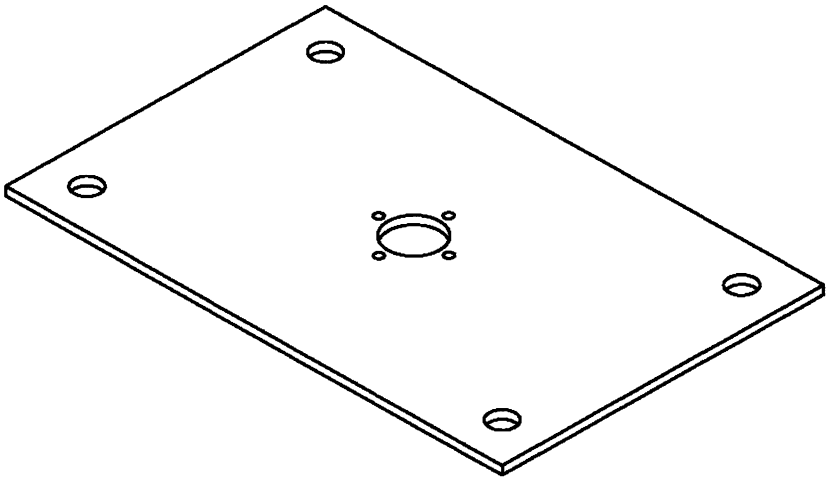

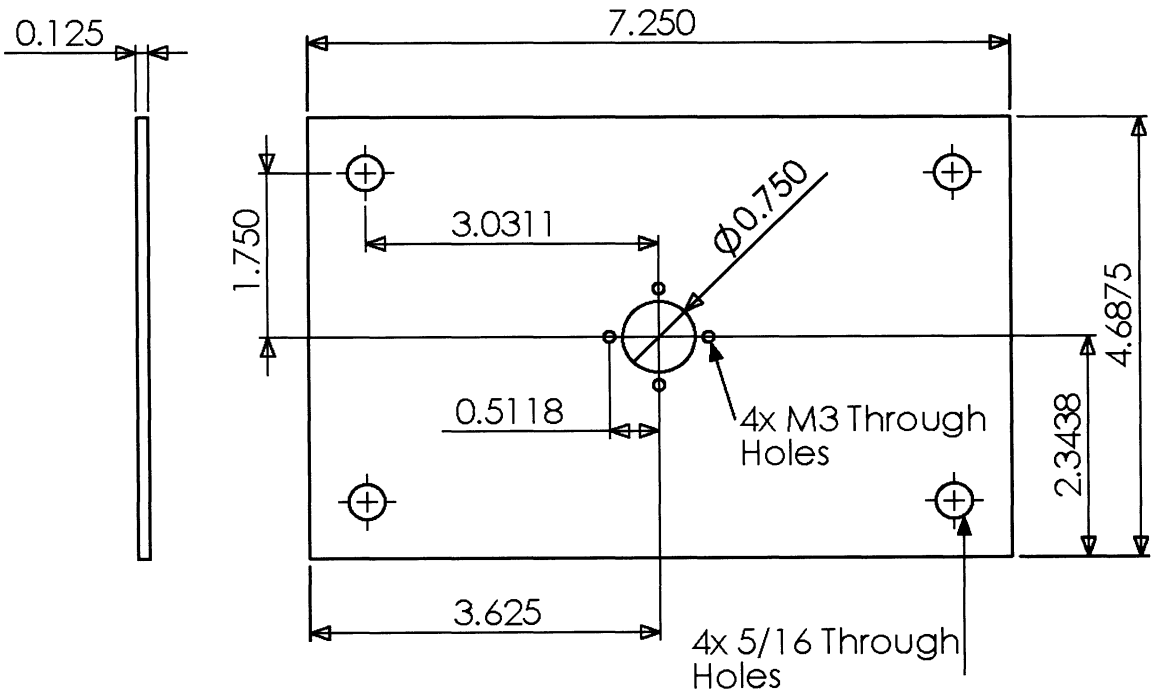

Part 4 - Rotating Disk		
Scale - 1:1	Material - Acrylic	Units - Inches

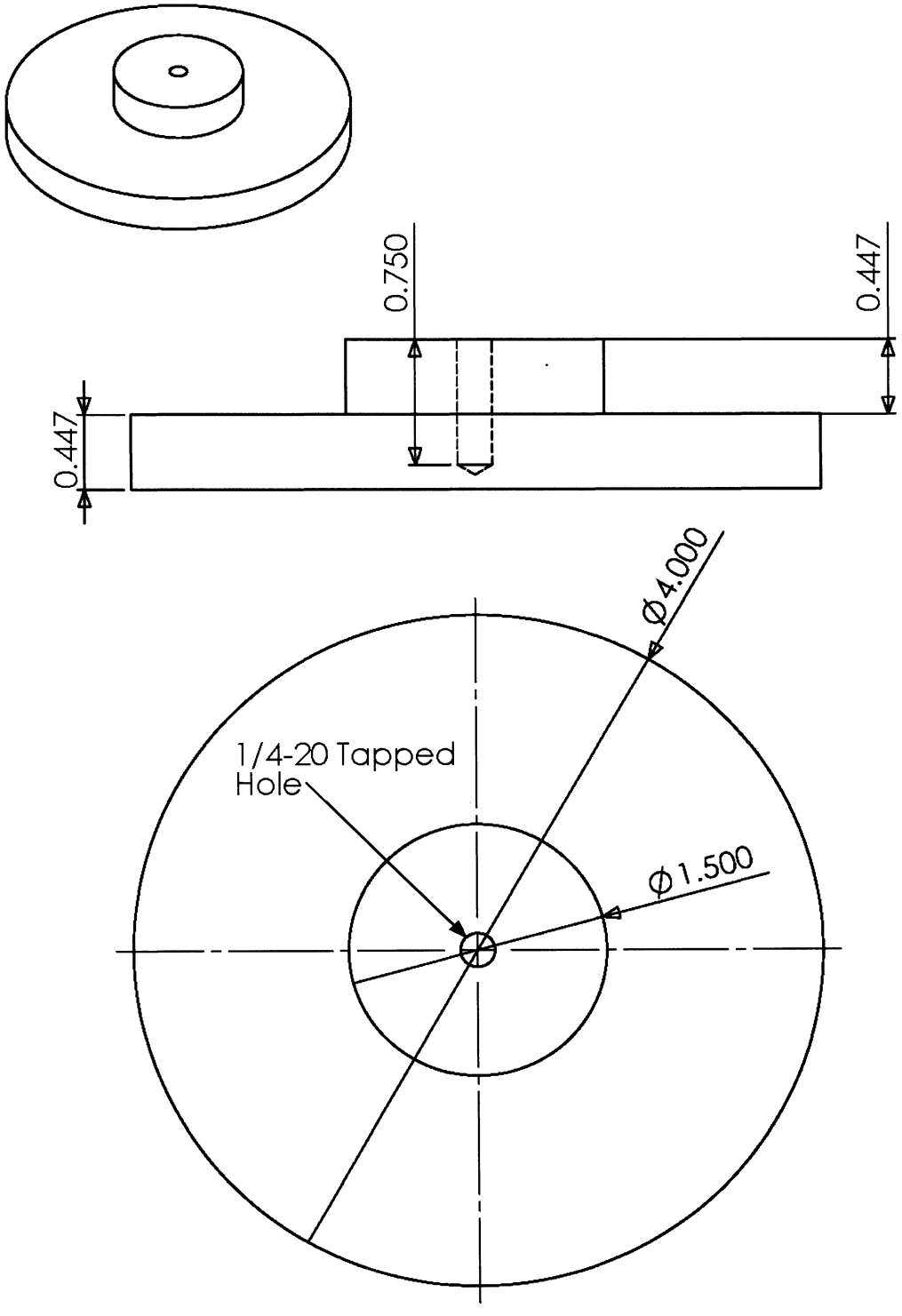

Part 5 - Rotating Disk Shaft		
Scale - 1:1	Material - Stainless Steel	Units - Inches

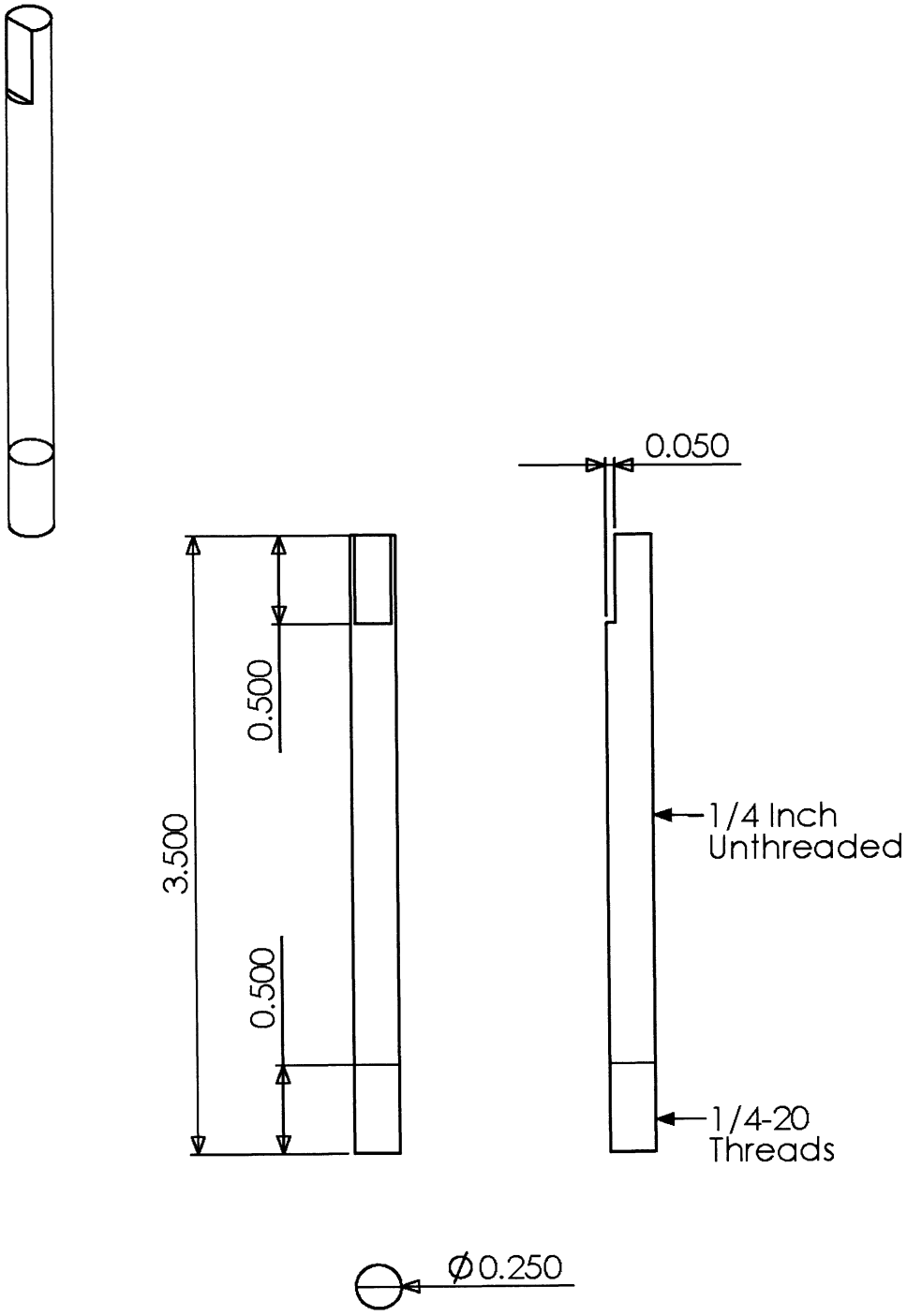

Part 6 - Assembled Rotating Disk with Shaft		
Scale - 1:2	Material - Acrylic/S.S.	Units - Inches

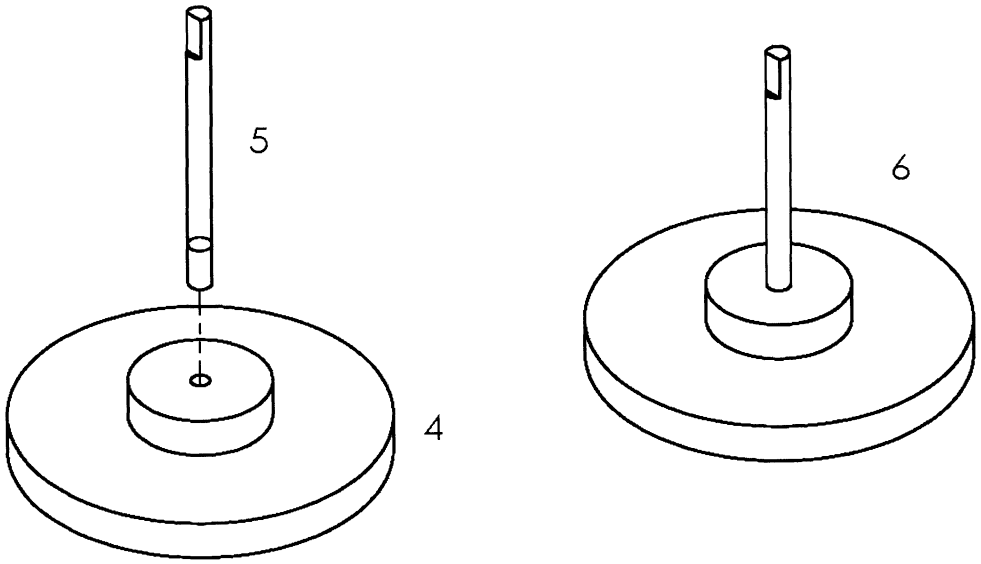

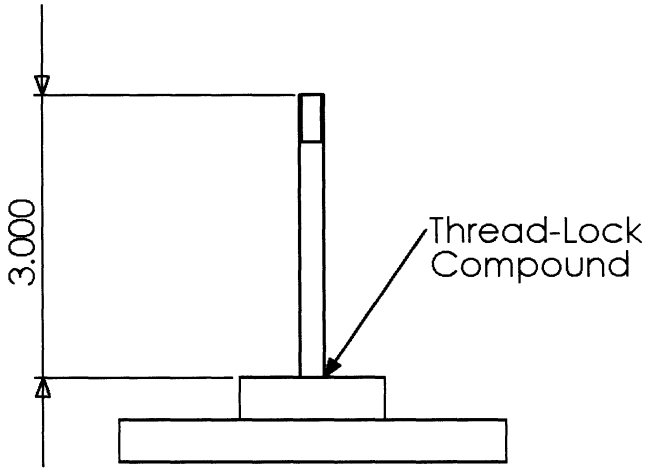

Part 7 - Motor Assembly		
Scale - 1:2	Material - N/A	Units - Inches

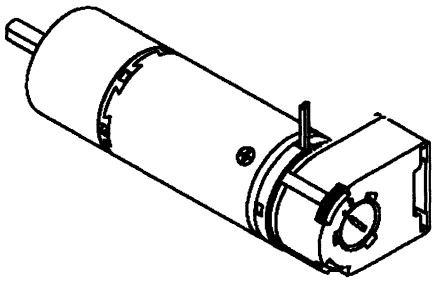

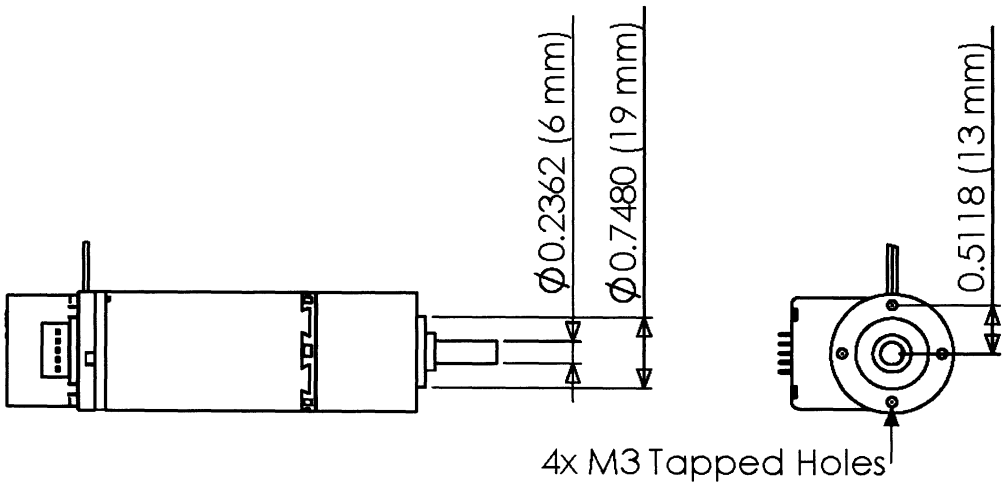

Only a few significant dimensions are shown.
3D Model From: www.maxonmotorusa.com

Part 8 - Bottom Probe Holder		
Scale - 1:2	Material - Acrylic	Units - Inches

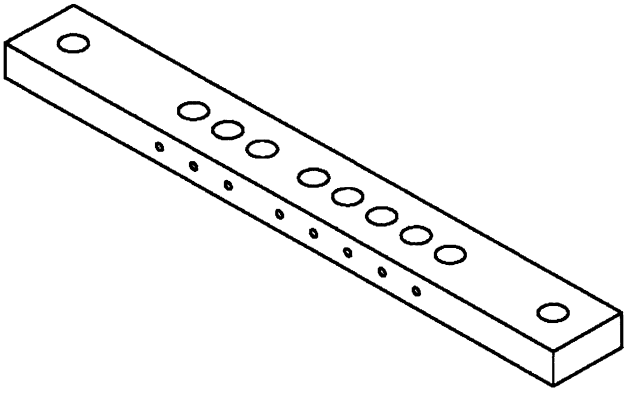

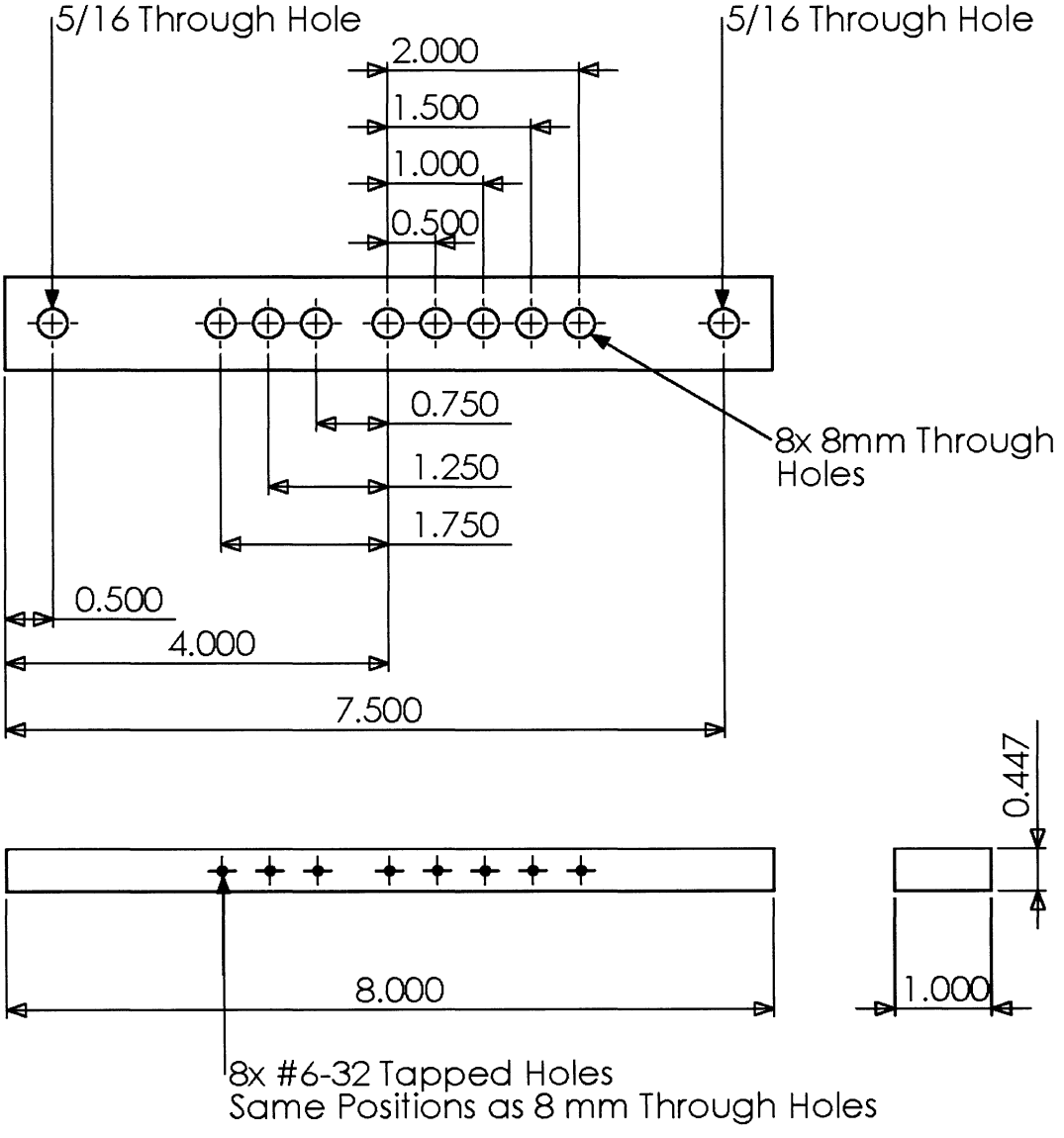

Part 9 - Side Probe - Support Plate		
Scale - 1:2	Material - Acrylic	Units - Inches

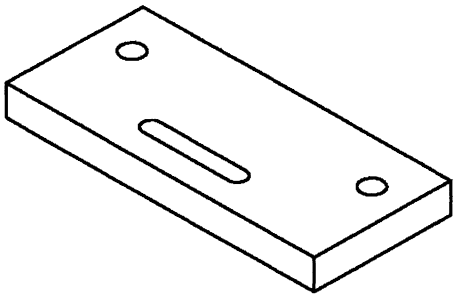

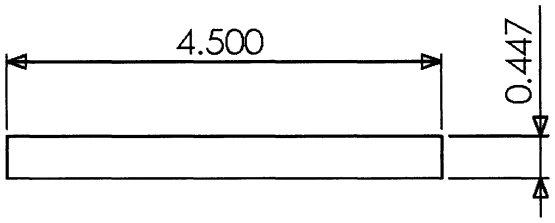

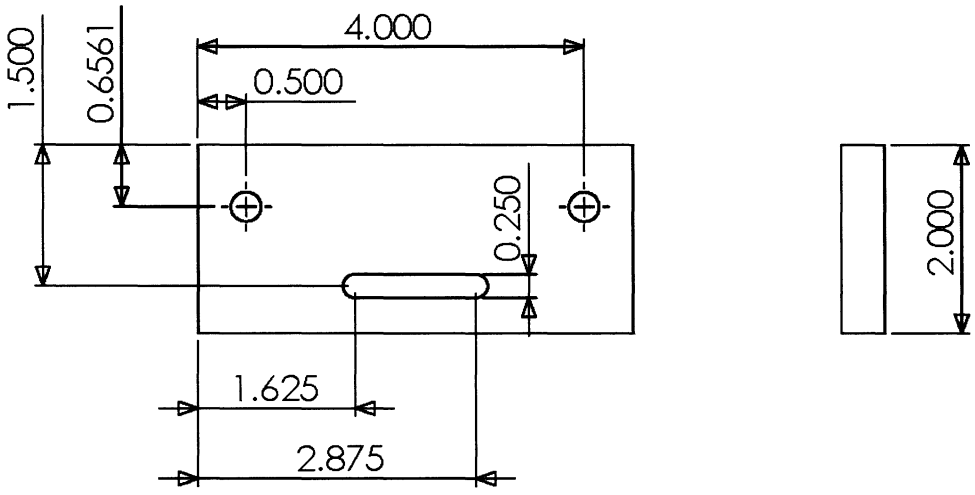

Part 10 - Side Probe - Base		
Scale - 1:1	Material - Acrylic	Units - Inches

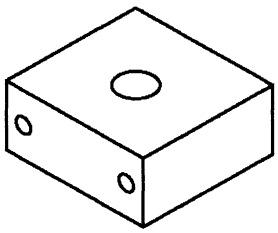

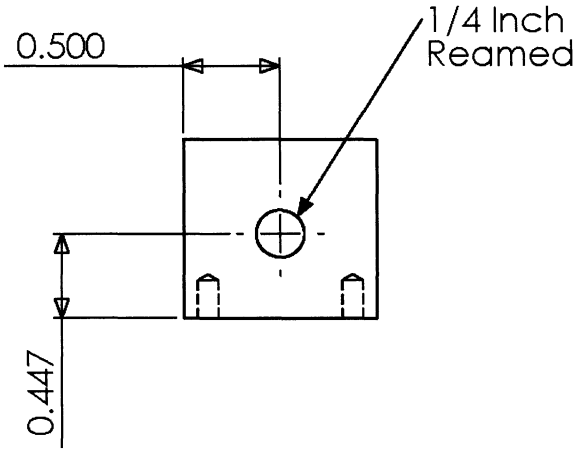

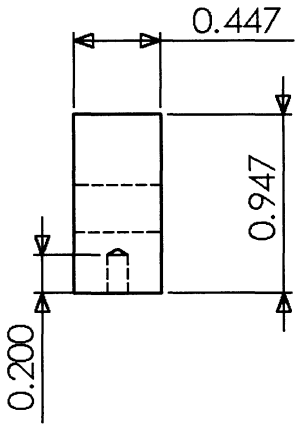

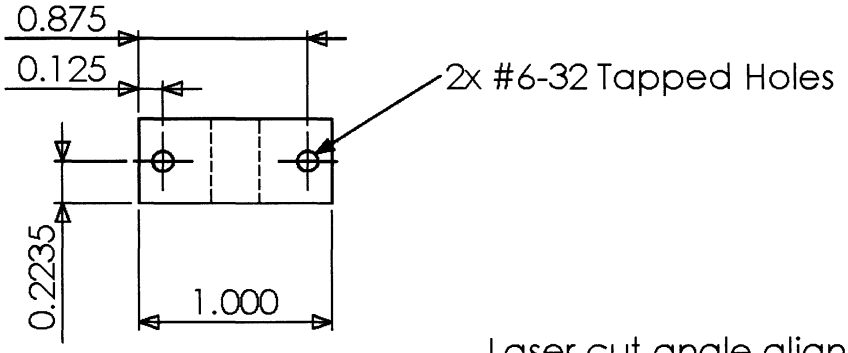

Laser cut angle alignment marks not shown.

Part 11 - Side Probe - Vertical Plate		
Scale - 1:1	Material - Acrylic	Units - Inches

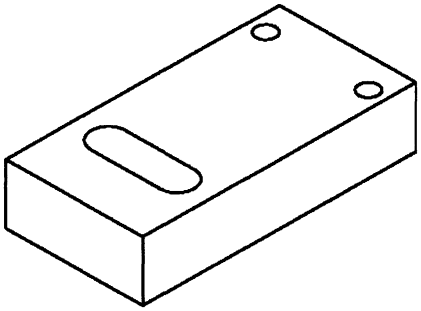

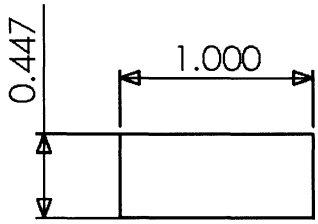

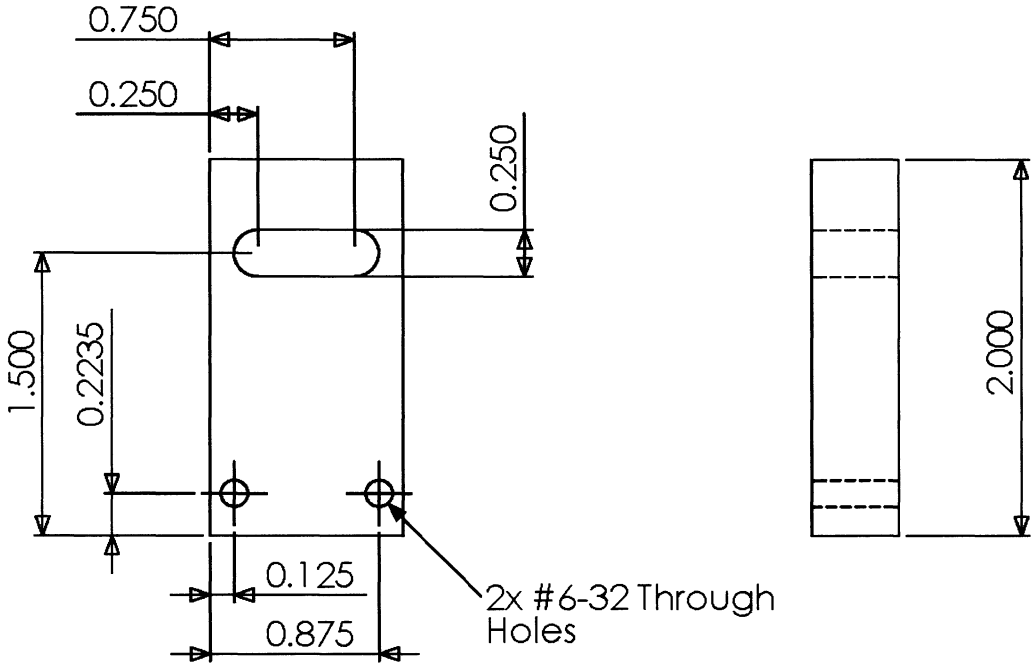

Part 12 - Side Probe - Clamp Base		
Scale - 1:1	Material - Acrylic	Units - Inches

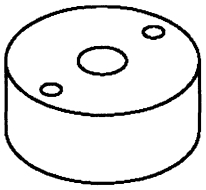

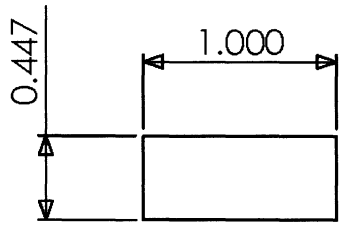

Laser cut angle alignment marks not shown.

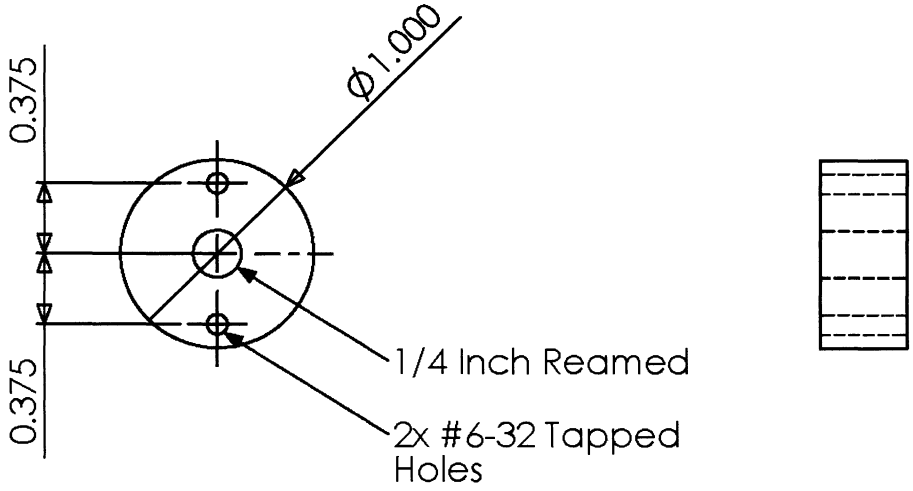

Part 13 - Side Probe - Clamp		
Scale - 1:1	Material - Acrylic	Units - Inches

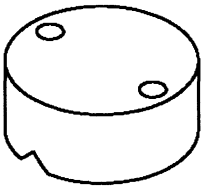

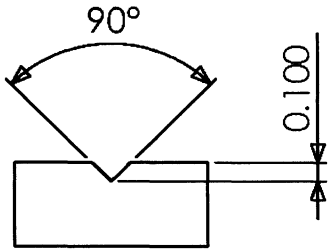

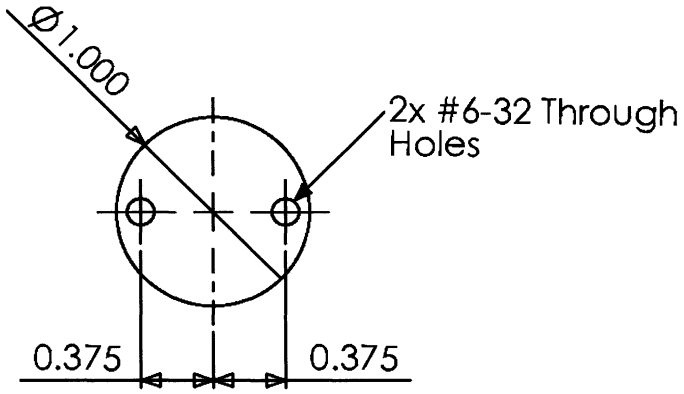

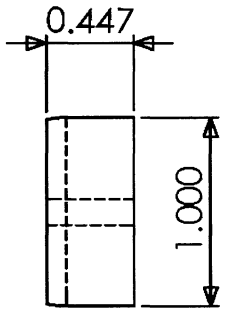

Probe 14 - Side Probe - Probe Spacer (8 mm)		
Scale - 2:1	Material - Acrylic	Units - Inches

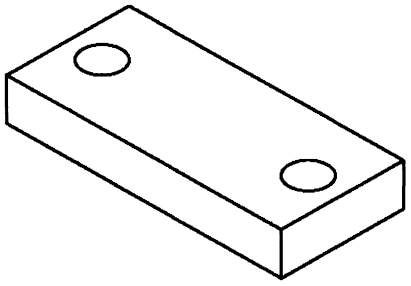

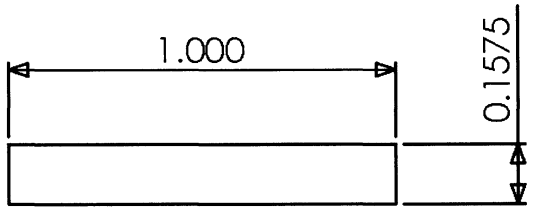

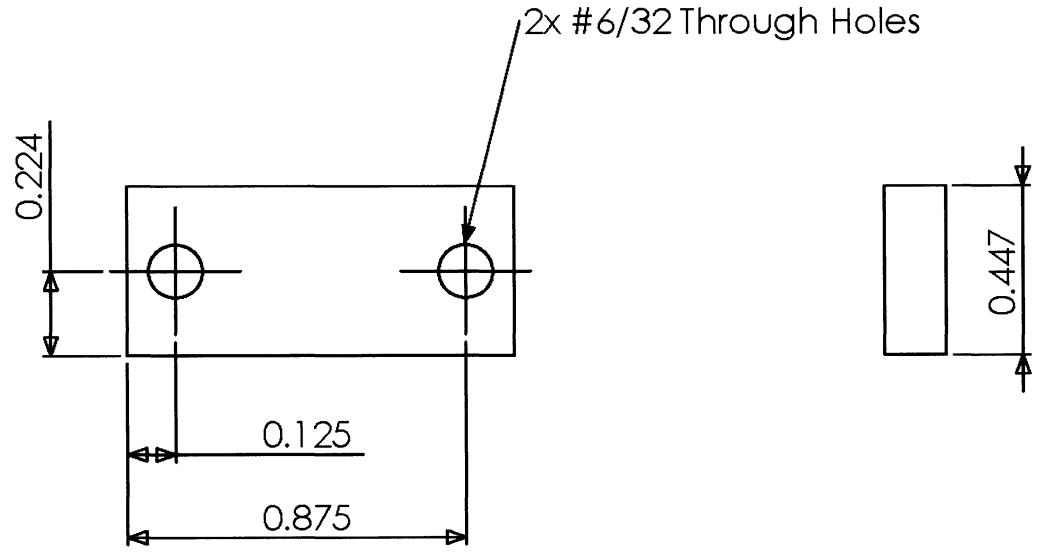

Part 15 - Embedded Screw		
Scale - 2:1	Material - Steel	Units - Inches

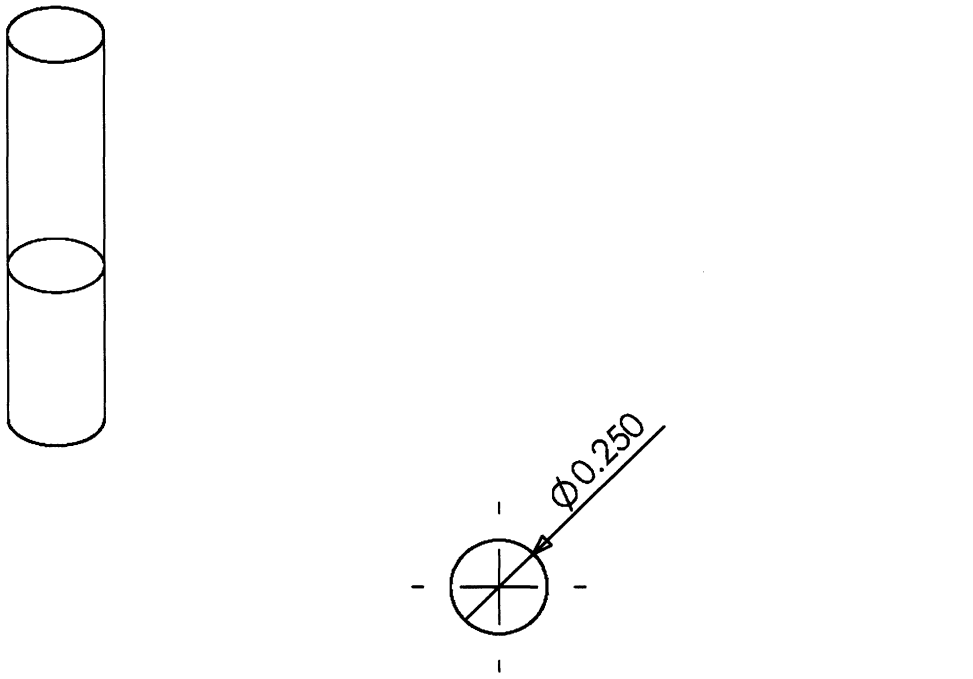

Part 16 - Base with Embedded Screw (Parts 10 + 15)		
Scale - 1:1	Material - Acrylic/Steel	Units - Inches

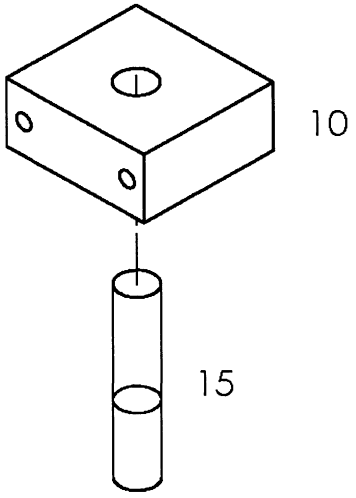

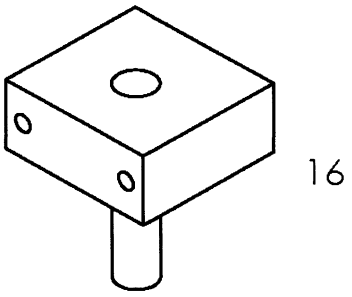

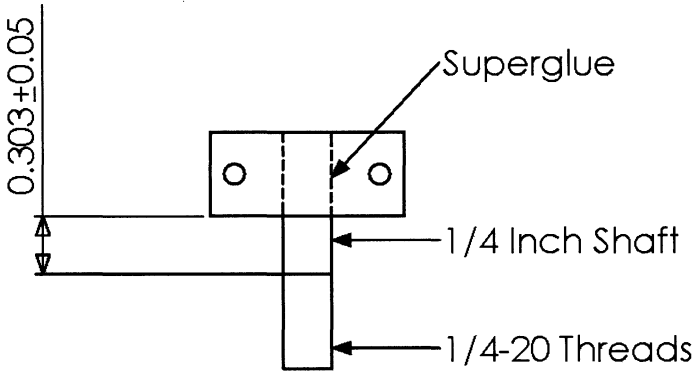

Part 17 - Clamp With Embedded Screwn (Parts 12 + 15)		
Scale - 1:1	Material - Acrylic/Steel	Units - Inches

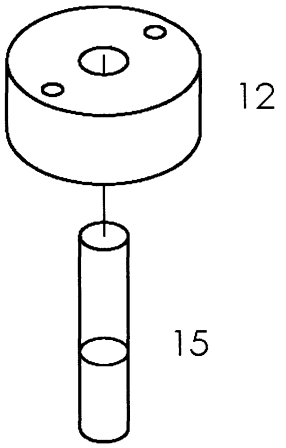

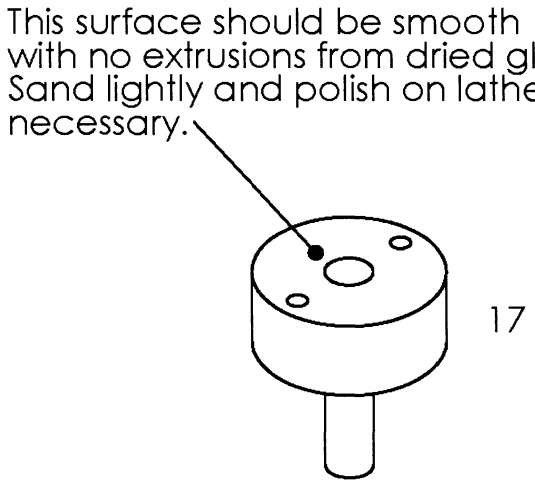

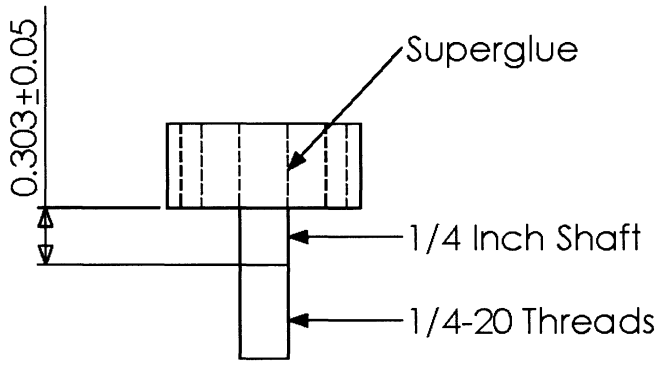

Part 18 - UDV Probe (5 mm Transducer, 4 MHz) - 8 mm OD		
Scale - 1:1	Material - N/A	Units - Inches

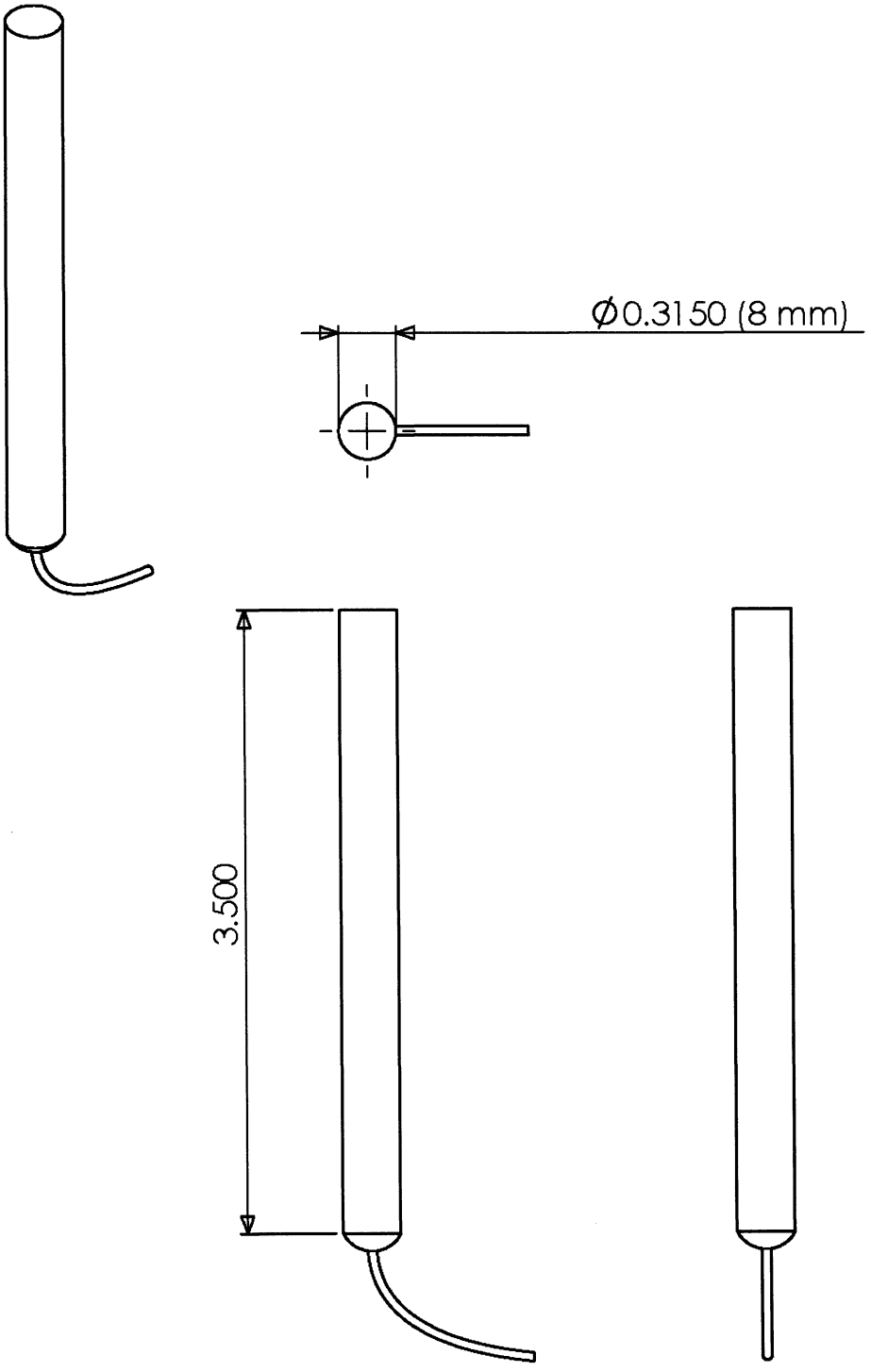

Part 19 - Side Probe Holder Assembly (Parts 9 - 18 + Various Hardware)		
Scale - 1:1.5	Material - N/A	Units - Inches

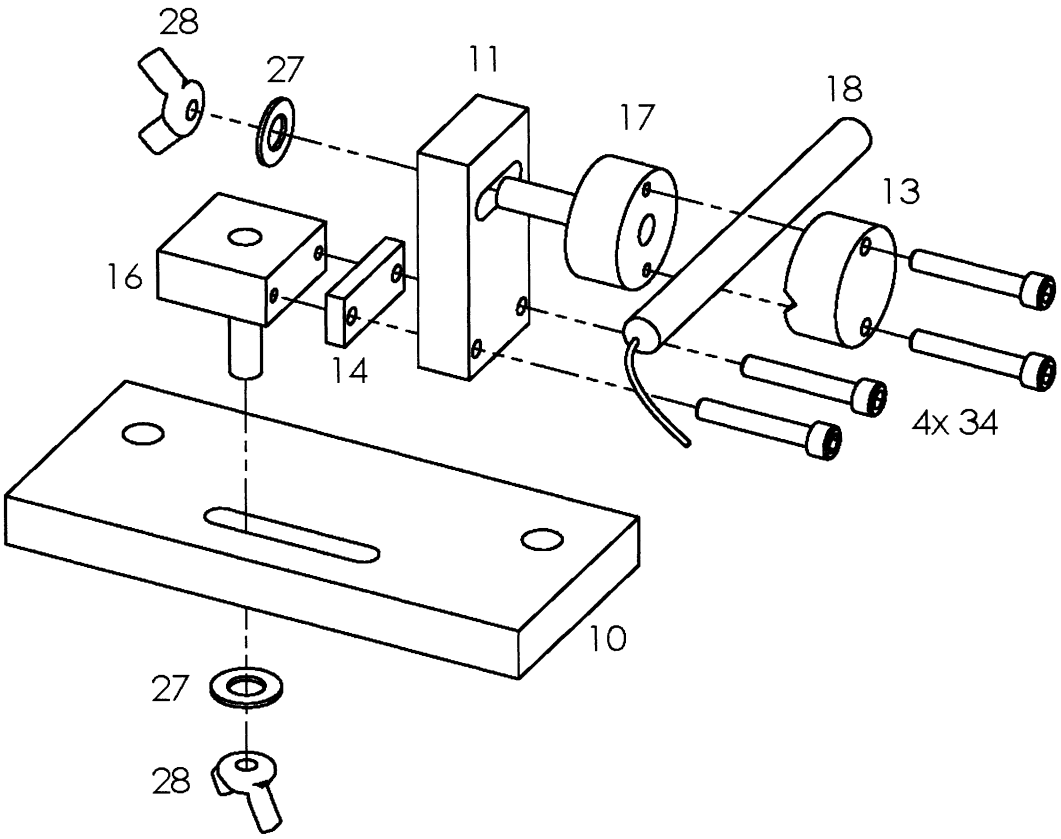

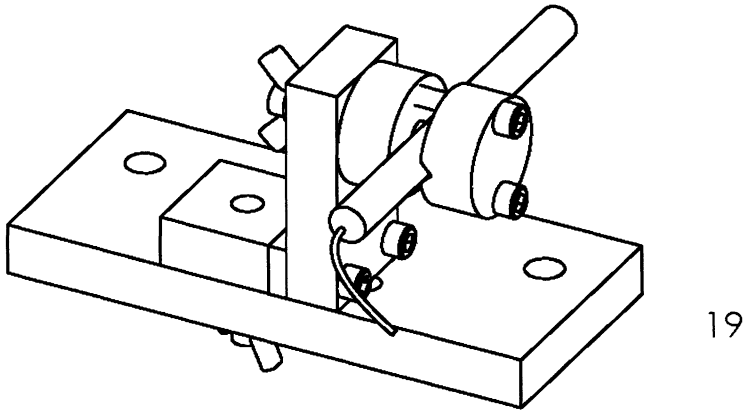

Part 21 - Shaft Coupler		
Scale - 1:1	Material - Aluminum	Units - Inches

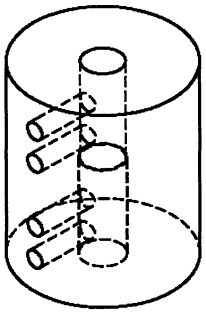

To make the series of holes in the center of the coupler, drill a through hole with a 6 mm drill bit or reamer. Then drill half way with the larger 1/4 inch drill bit or reamer. This should be done on the lathe to ensure eccentricity is minimized.

To remove burrs the center holes after tapping the 6-32 set screw holes, put a 6 mm reamer or 1/4 inch reamer in a vise and hand turn the piece onto the reamer until all burrs are removed.

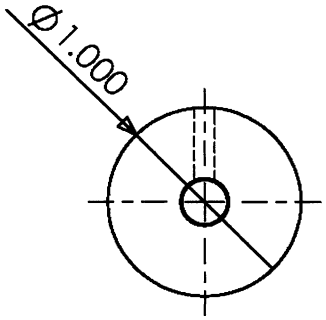

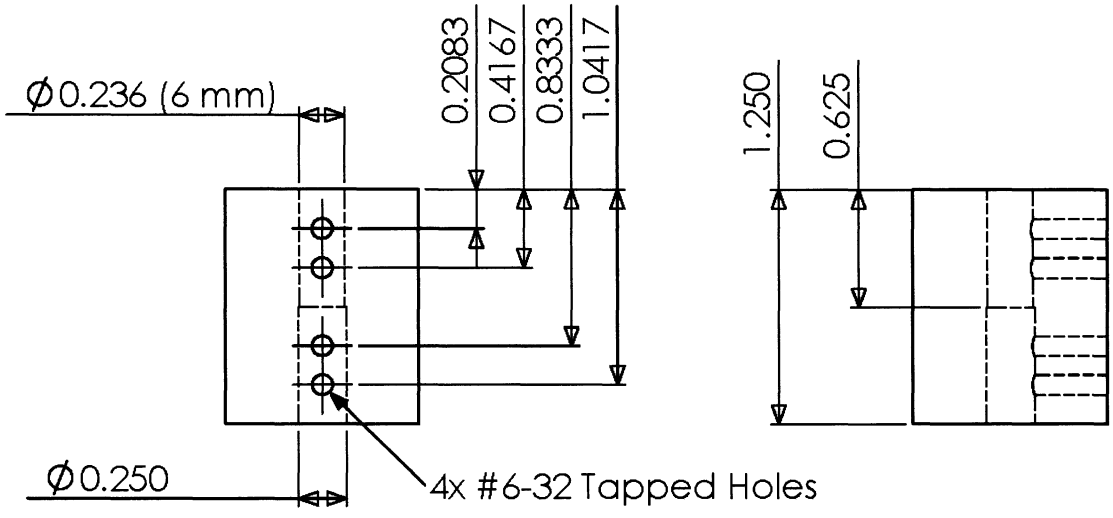

Part 25 and Part 26 - Aluminum Standoffs For 5/16 Inch Threaded Rods		
Scale - 1:1	Material - Aluminum	Units - Inches

25

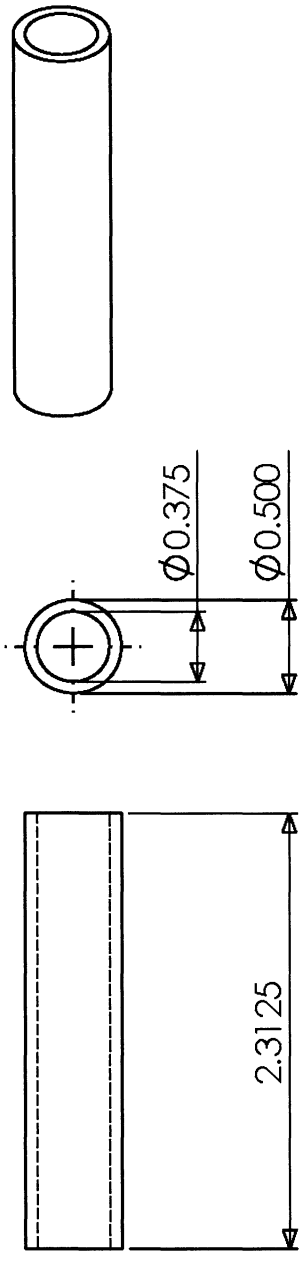

26

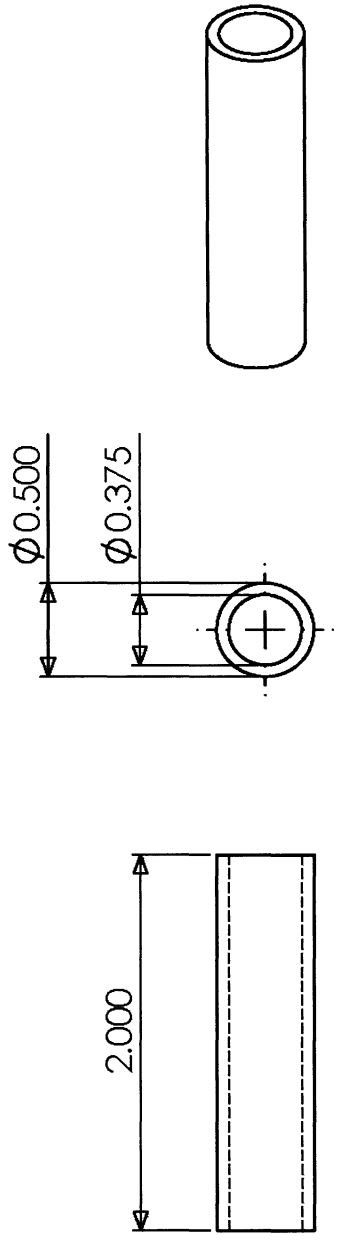

Part 35 - Motor/Lid Assembly Exploded View (1/2)		
Scale - 1:2.5	Material - N/A	Units - Inches

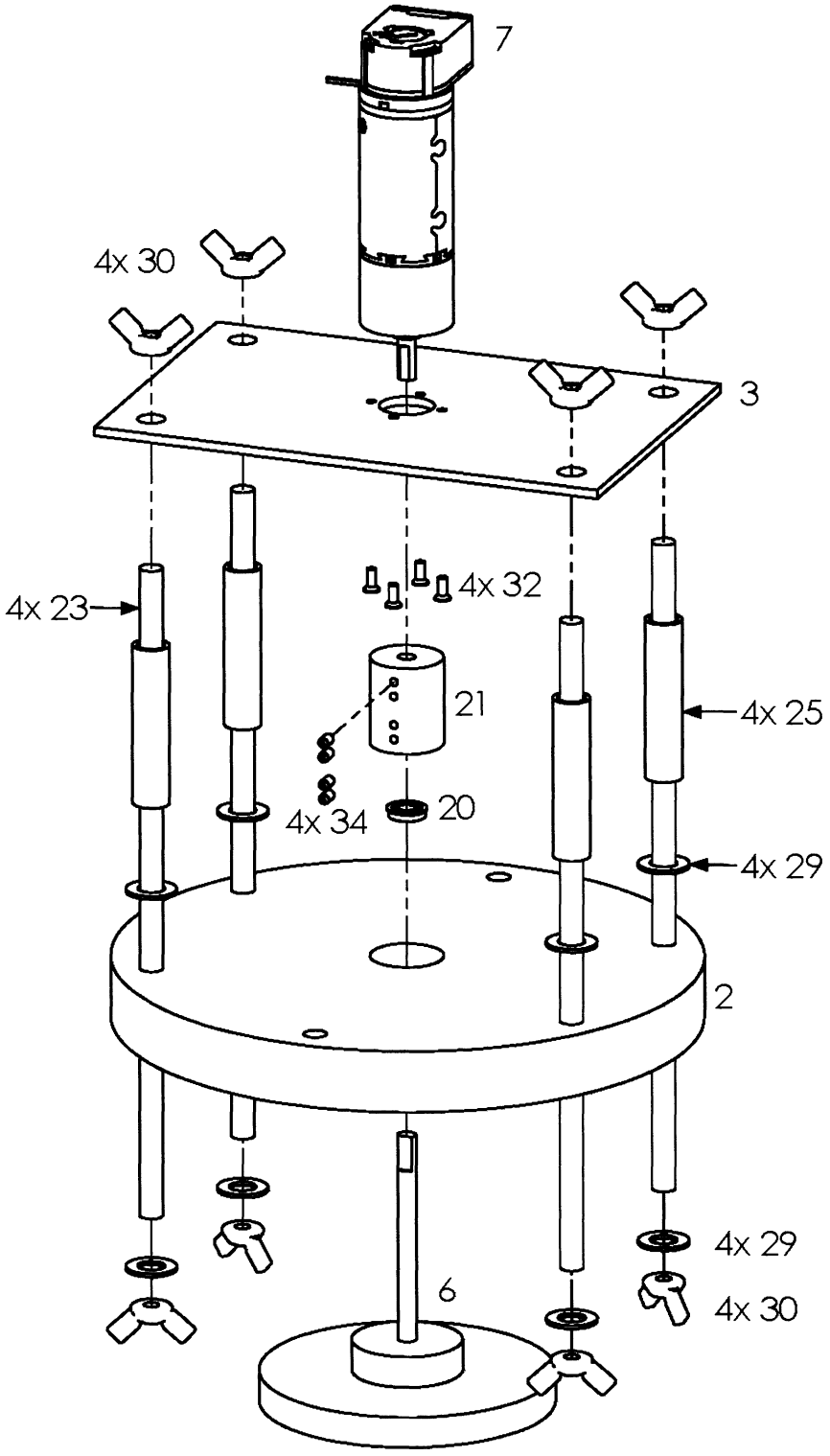

Part 35 - Motor/Lid Assembly (2/2)		
Scale - 1:2	Material - N/A	Units - Inches

35

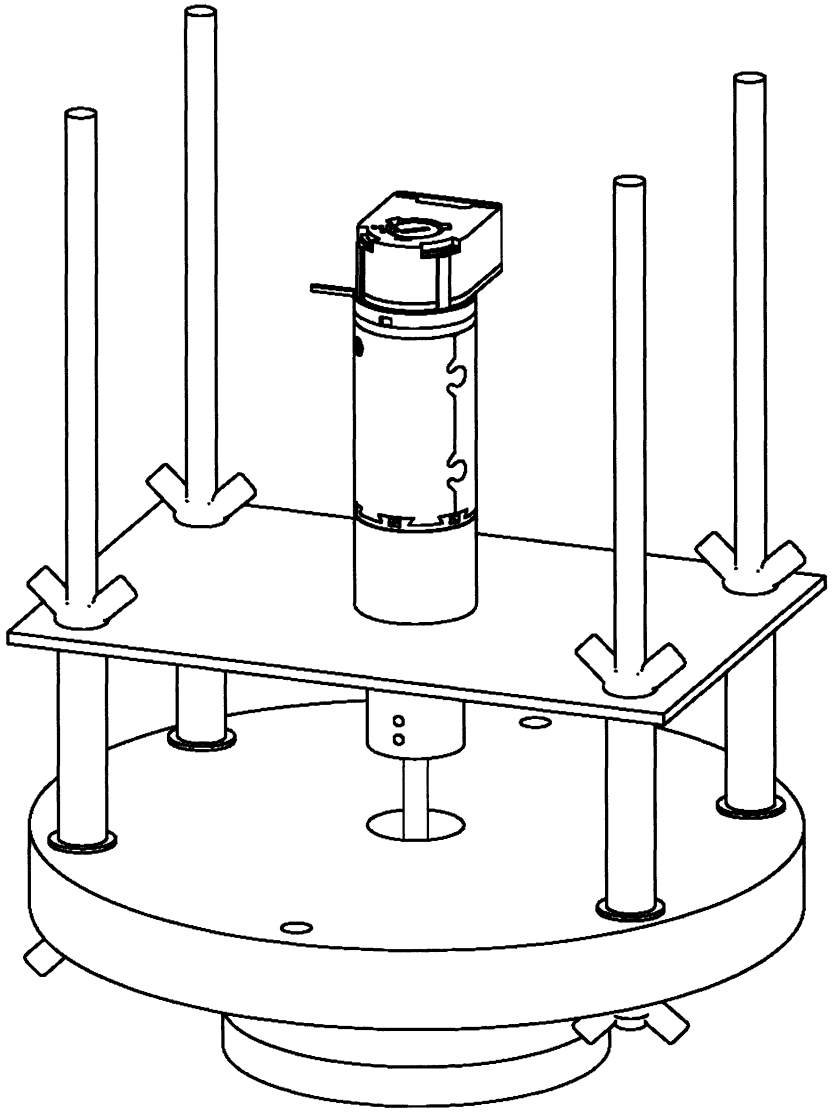

Part 36 - Fluid Container With Stilts Exploded View (1/2)		
Scale - 1:2.5	Material - N/A	Units - Inches

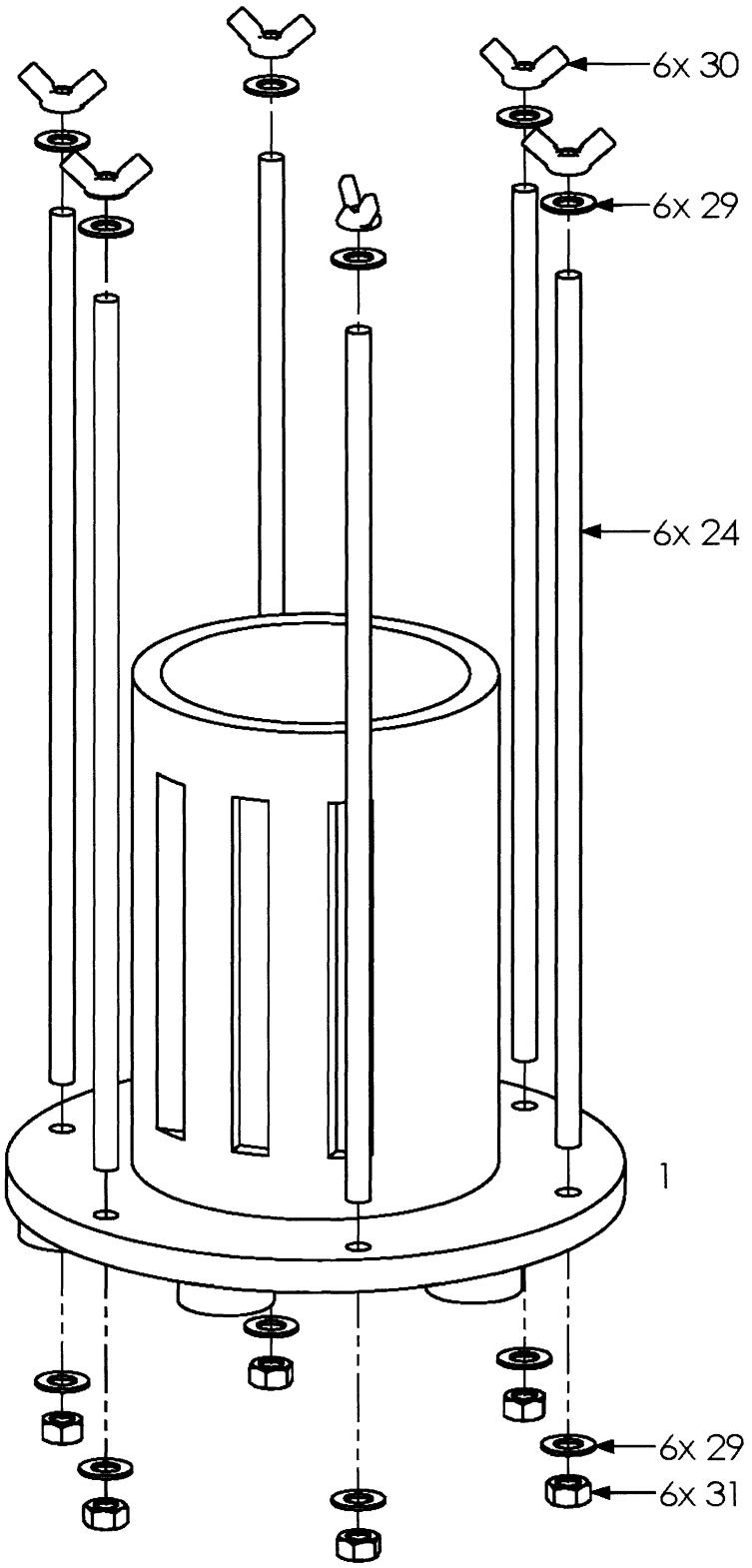

Part 36 - Fluid Container With Stilts (2/2)		
Scale - 1:2	Material - N/A	Units - Inches

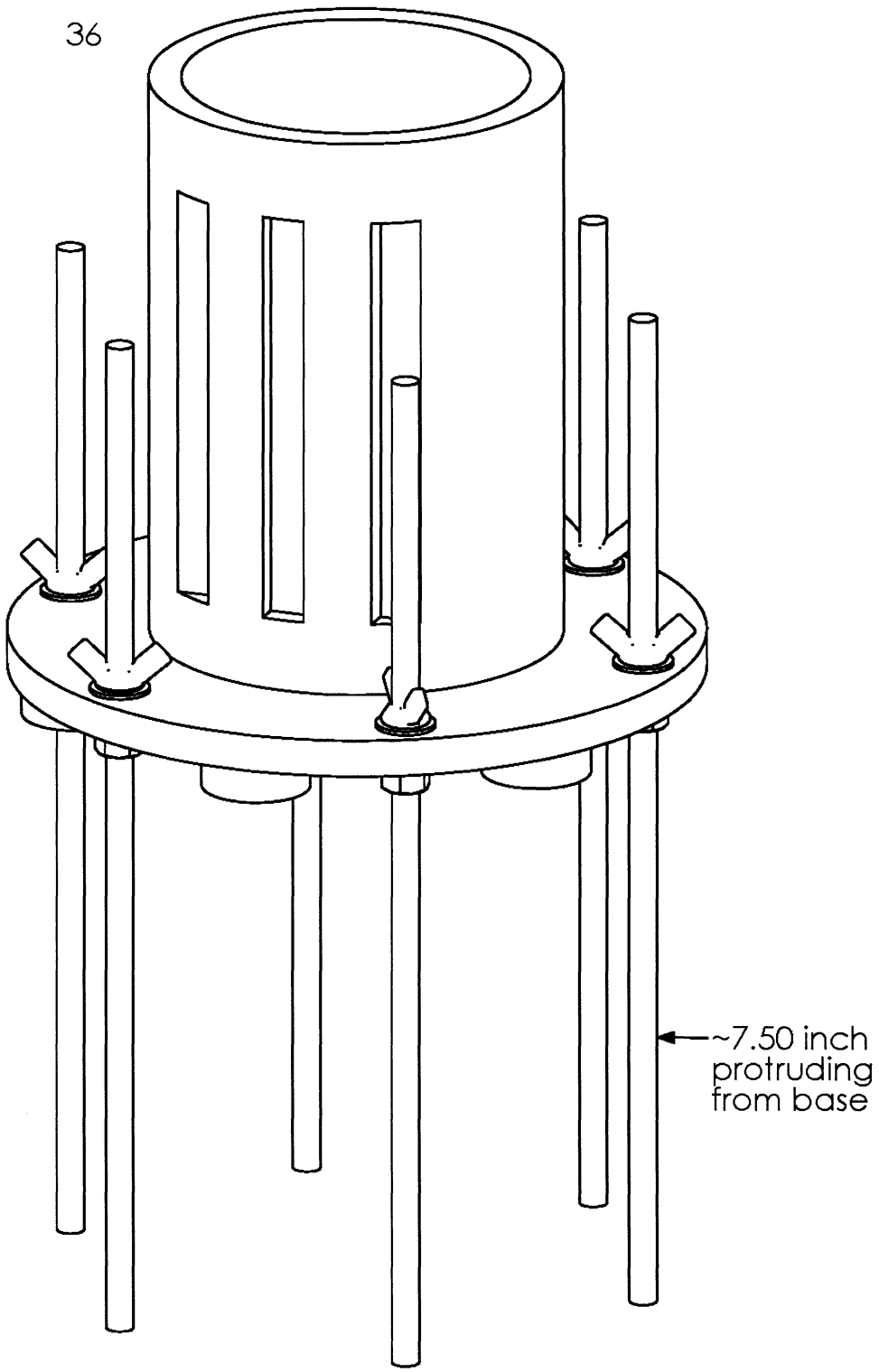

Part 37 - Full Assembly Exploded (1/2)		
Scale - 1:4	Material - N/A	Units - Inches

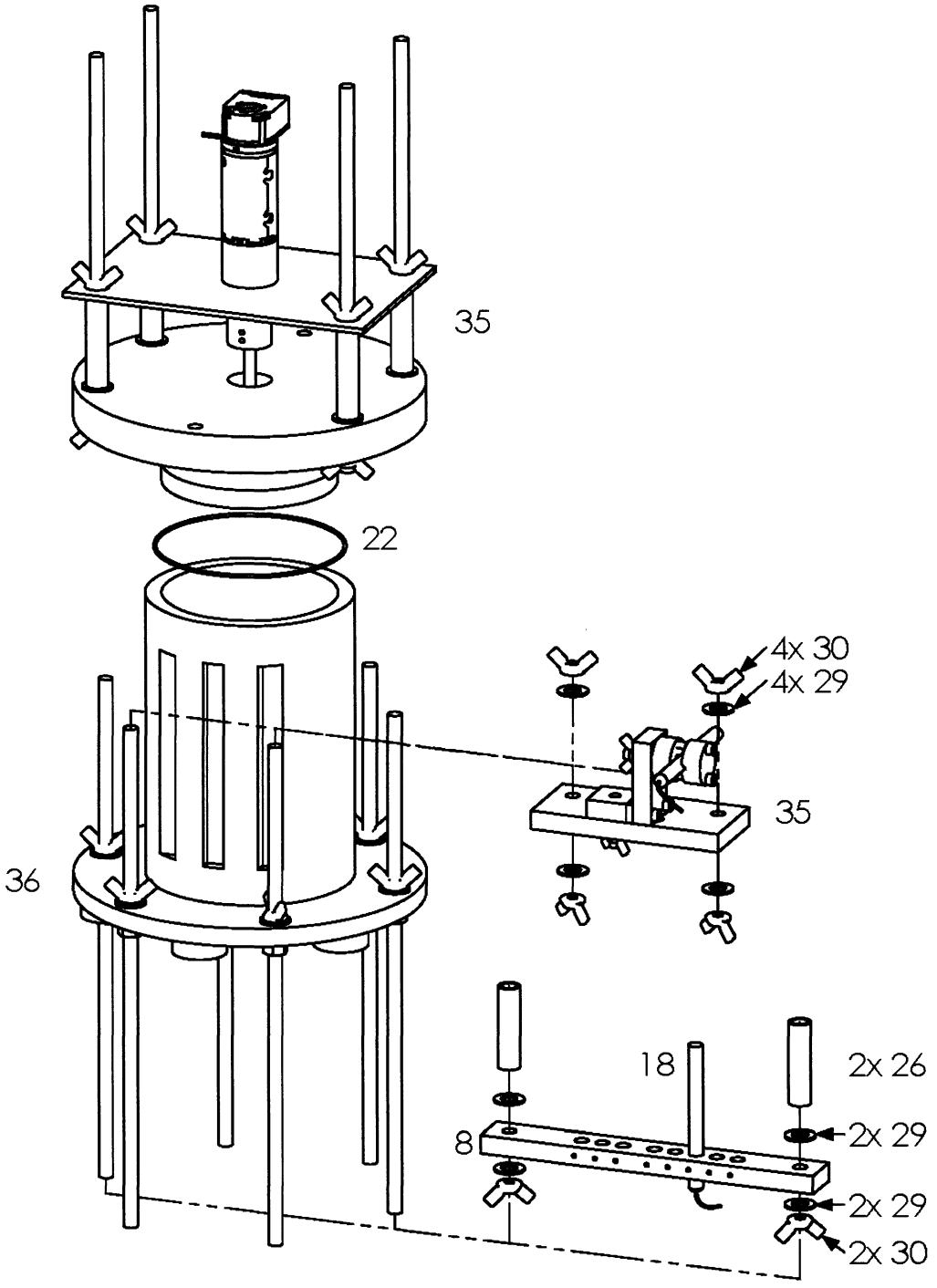

Part 37 - Full Assembly (2/2)		
Scale - 1:3	Material - N/A	Units - Inches

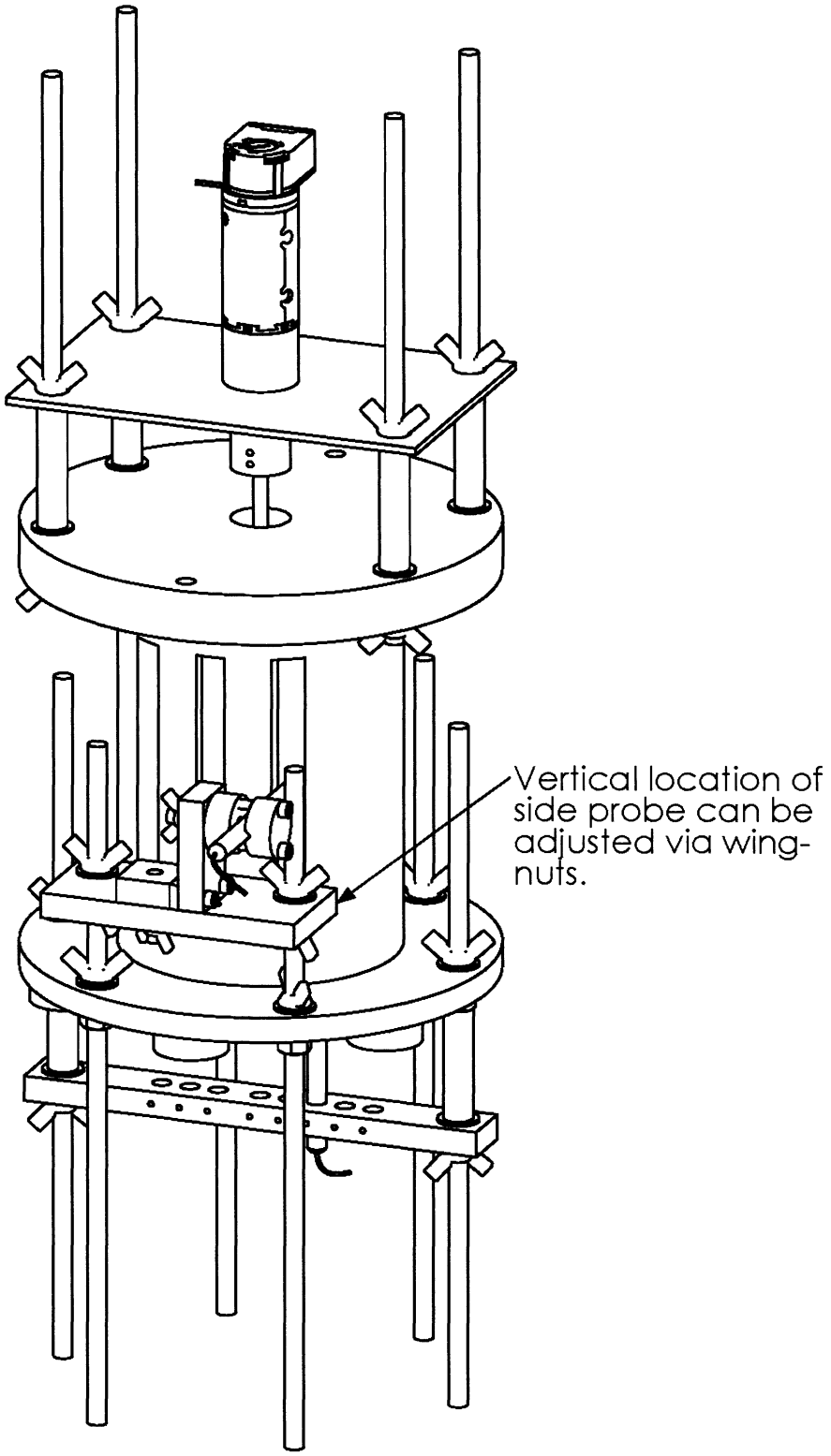

Part 38 - Probe Alignment Block		
Scale - 1:1	Material - Acrylic	Units - Inches

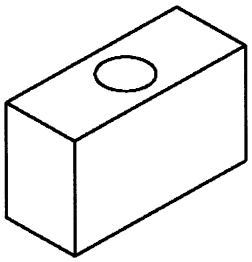

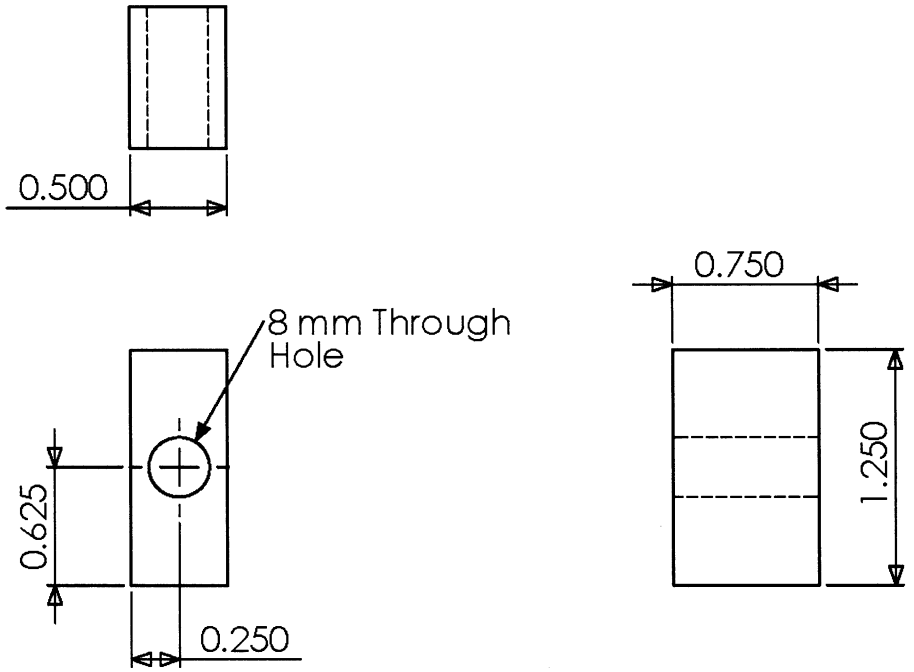

Part 39 - UDV Beam Finder (1/2)		
Scale - 1:2	Material - Acrylic and S.S.	Units - Inches

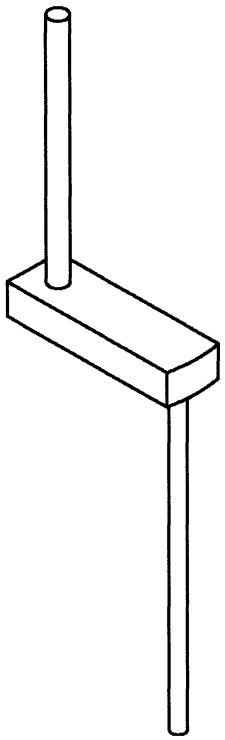

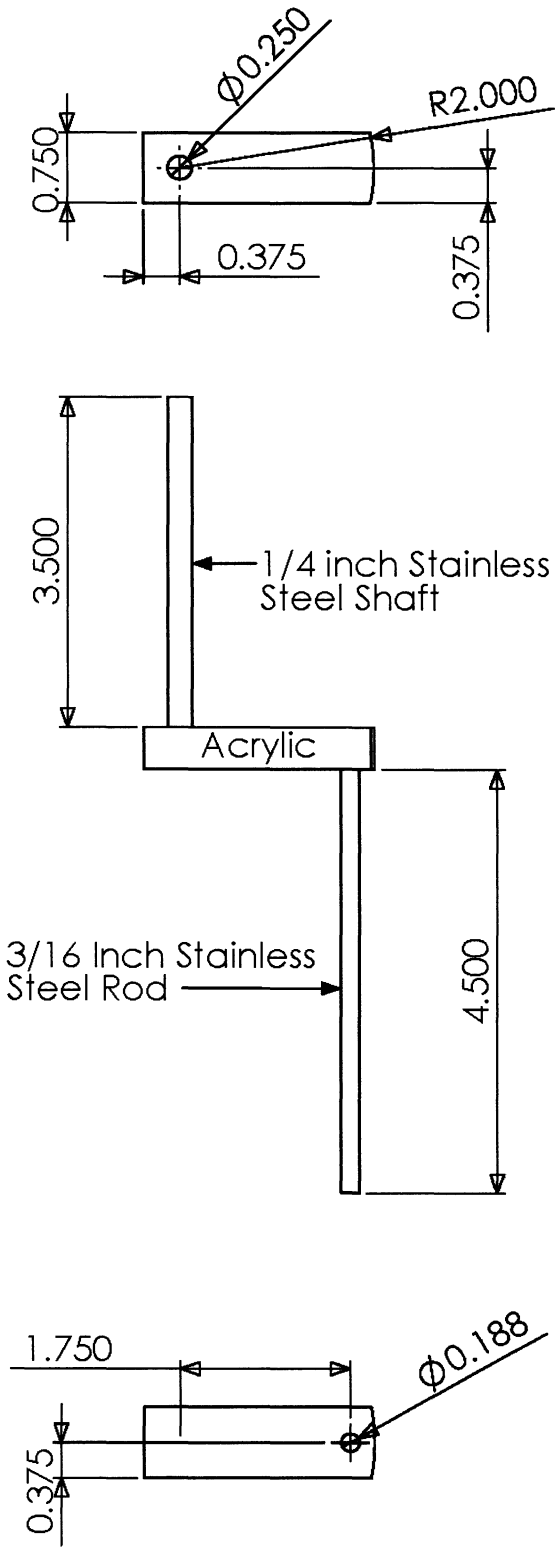

Part 39 - UDV Beam Finder Assembly (2/2)		
Scale - 1:2	Material - N/A	Units - Inches

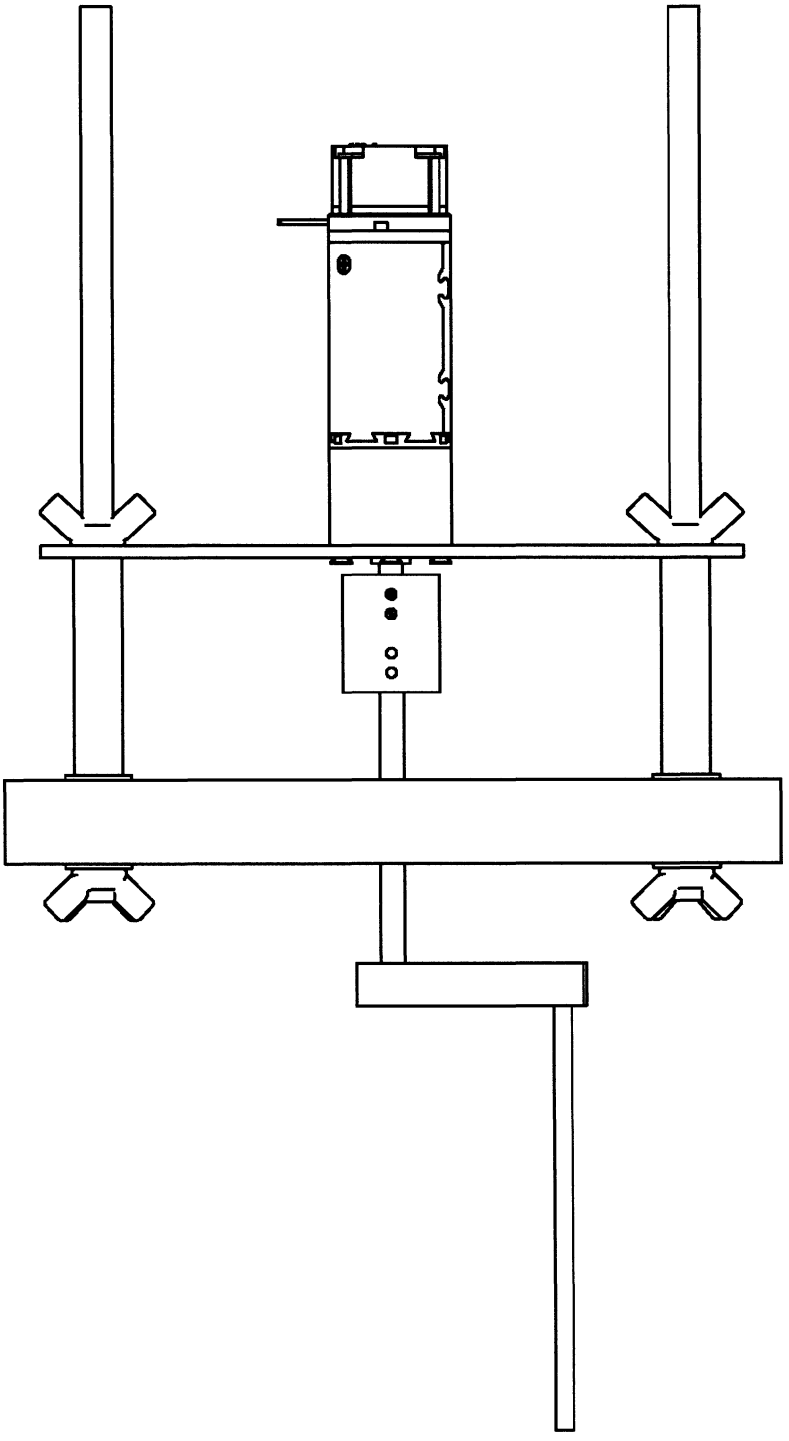

Appendix B

UDV Experiment Setup Procedure

Add UDV Beads to Fluid

1. Fill the fluid container with fluid (tap water or 20% glycerin/water mixture) until 0.25 inch above the blue mark as shown below (5.25 in. from bottom).

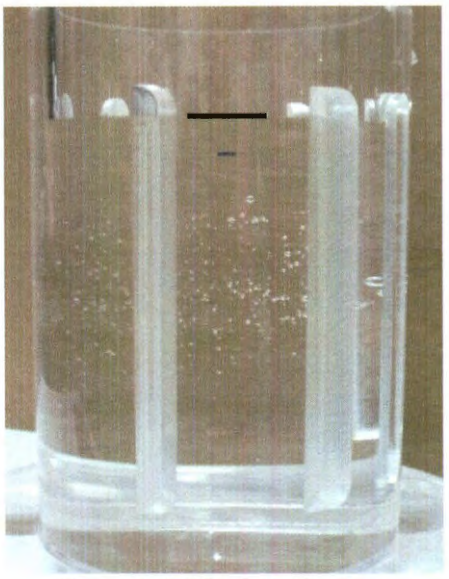

Step 1: Filled Cylinder

2. Take the 10 mL syringe and pull out the plunger.
3. Using a scale, weigh out 0.1 g of white UDV beads on weighing paper. (Be sure to zero the scale after putting the weighing paper on the scale.)
4. Pour the 0.1 g of white UDV beads into the 10 mL syringe and dispose of the weighing paper.
5. Add approximately 10 mL of water to the syringe on top of the beads until the water completely fills the syringe.
6. While stopping the small opening of the syringe with your thumb, gently reinsert the plunger just enough to seal the large opening.
7. Mix the UDV bead/water mixture by shaking vigorously (shaking horizontally will help minimize the amount of bubbles that form).
8. After the mixture is well mixed, place the opening towards the bottom of the fluid container. Then syringe the UDV bead/water mixture into cylinder.
9. Once the contents are fully expelled, re-syringe some fluid/bead mixture several times or until the 10 mL syringe is mostly clean of UDV beads.
10. Remove the 10 mL syringe from the fluid and draw up as much air as possible. Now with the top of the syringe pointed down, slowly expel the

contents of the syringe into the fluid container without submerging the stem. This step removes any of the fluid/UDV bead mixture that was still left in the syringe.

11. Remove the plunger of the 10 mL syringe. Then wash, dry, and store the 10 mL syringe.

Assembling the Motor and Rotating Lid

1. Attach the motor to the motor support plate using 4 M3 flat head screws.
2. Attach the 6 mm end of the shaft coupler to the output shaft of the motor using two #6-32 set screws (ensure that the set screws contact the shaft on the flat machined face).
3. Carefully press fit a 0.25" x 0.5" bearing into the hole in the middle of the top plate (if this has not already been done).
4. Place 4, long, 5/16-18, threaded rods in a rectangular pattern through the holes on the top plate.
5. Screw on 4 x 5/16-18 wing-nuts onto the ends of the long threaded rods on the bottom side of the top plate (ensure that the properly grooved side of the top plate is on the bottom).
6. Place 4 x 5-16 washers onto threaded rods on the top side of the top plate (ensure that the smooth sides of the washers are in contact with the top plate to prevent scaring the acrylic).
7. Place 4 stand-offs on the threaded rods.
8. Slide on the motor support plate with the attached motor onto the four threaded rods (output shaft of the motor should be pointed down).
9. Loosely Screw on 4 more 5/16 wing-nuts onto the top side of the threaded rods, do not fully tighten as there is no way to tell if the output shaft of the motor is concentric with the bearing.
10. Insert the shaft of the rotating lid from the bottom of the top plate, through the bearing, and into the shaft coupler. Adjust the alignment of the motor plate as necessary (take care not to damage the bearing as you are inserting the shaft of the rotating lid).
11. Carefully adjust the alignment of the motor support plate so that the output shaft of the motor is concentric with the bearing and rotating lid (if the rotating lid can freely spin on the bearing while inside the shaft coupler, this indicates that the shafts are concentric as there is about 0.001" gap between the shaft of the rotating lid and the shaft coupler).
12. Once everything is concentric, carefully tighten the 5/16 wing-nuts to lock everything into place. Spin the rotating lid or the motor to check that everything is still concentric. Once properly adjusted, do not carelessly loosen this assembly as the alignment process is very tedious and time consuming.
13. Attach the rotating lid to the shaft coupler using one or two 6-32 set screws, making sure that the set screws contact the shaft of the rotating lid on the flat machined face (the vertical position of the rotating lid can be adjusted slightly changing its vertical position in the shaft coupler).

Installing the Motor and Rotating Lid

1. Clean and dry the rubber o-ring seal and make sure it is properly seated in the grove on the Motor/Lid assembly.
2. Slowly lower the lid into the fluid container.
3. As the lid approaches the surface of the fluid, tilt the top of the assembly away from you. Also push away from you so that the lid contacts the inside of the fluid container on the edge opposite of you.

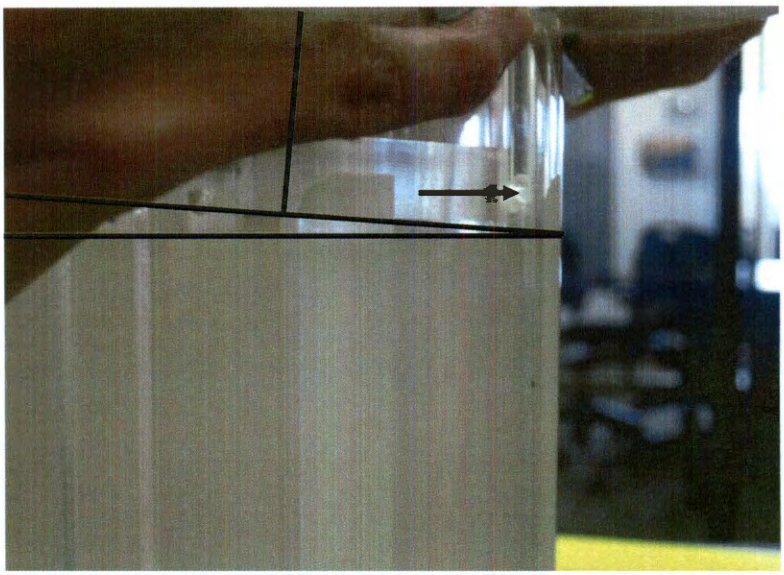

Step 3: Desired Orientation of Lid when Assembling Enclosure

4. Slowly lower the Motor/Lid assembly into the fluid while maintaining the orientation described in step 3.
5. As the Motor/Lid assembly begins to contact the top of the fluid container, slowly return the Motor/Lid assembly to an upright orientation while simultaneously continuing to lower the Motor/Lid assembly into the fluid.
6. If done properly, capillary action should suck the Motor/Lid assembly into place, the lid should be completely submerged in fluid and no bubbles should form under the lid. If bubbles form under the lid, completely remove the Motor/Lid assembly, clean the bottom of the lid and repeat steps 2-5. If there is insufficient fluid to completely submerge the lid, remove the Motor/Lid assembly, add fluid and repeat steps 2-5.
7. The bottom edge of the lid should be 5 in. from the bottom of the fluid container (at the blue line). If needed, the lid height can be adjusted by loosening the set screw on the coupling between the motor shaft and the support shaft for the lid.
8. Seat the Motor/Lid assembly onto the top of the fluid container. Ensure that the assembly is resting vertically and that the o-ring is properly seated.
9. Using the velocity control VI, ensure that the rotating lid is not rubbing against the cylinder by looking for cyclical patterns in the velocity profile.

Mounting the Probe on the Bottom Face of the Cylinder

1. Locate the bottom probe mount beneath the fluid cylinder.
2. Insert the probe into the hole based on the desired offset.
3. Add a drop of Ultrasonic Transmission Gel to the tip of the probe. Make sure the black surface on the tip of the probe is completely covered with gel.
4. Push the probe upwards until the tip of the probe contacts the bottom surface of the fluid cylinder.
5. Insert and tighten the nylon set screw so that the probe stays in place.

Mounting the Probe on the Side of the Cylinder

1. Adjust the height of the probe support plate on the side of the fluid container by raising or lowering the two 5-16 hex nuts under the support plate.
2. Secure the support plate in place by tightening the two 5/16-18 wing nuts on top of the support plate. Then, check that the support plate is level.
3. Slightly loosen the 1/4-20 wing nut that keeps the sliding block in place so that it can barely slide along the support plate and completely loosen the 1/4-20 wing nut that aligns the probe to the appropriate angle.
4. Move the sliding piece near the appropriate side bevel so that the probe can be mounted.
5. Loosen the two black #6-32 screws on the side of the probe mount and slide the probe along the groove between the two circular blocks.
6. Take the alignment block and slide it over the tip of the probe.
7. Push the alignment block against the fluid cylinder so it is square with the two edges of the desired bevel and retighten the two black #6-32 screws.
8. Confirm that the alignment block is square with the two edges of desired bevel and tighten the two 1/4-20 wing nuts to keep the mount from sliding or changing angle.
9. Loosen the bottom black #6-32 screws and completely unscrew the top black #6-32 screw on the circular block and remove the probe from the mounting device while taking the alignment block from the tip of the probe.
10. Add a drop of Ultrasonic Transmission Gel to the tip of the probe. Make sure the black surface on the tip of the probe is completely covered with gel.
11. Place the probe into the groove on the side circular block and screw in the two black #6-32 screws so that the probe can barely slide in and out.
12. Push the probe forward until the tip of the probe contacts the surface of the fluid container and fully tighten the two black #6-32 screws to keep the probe in place. If done correctly, the probe should be perpendicular to the face of the bevel.

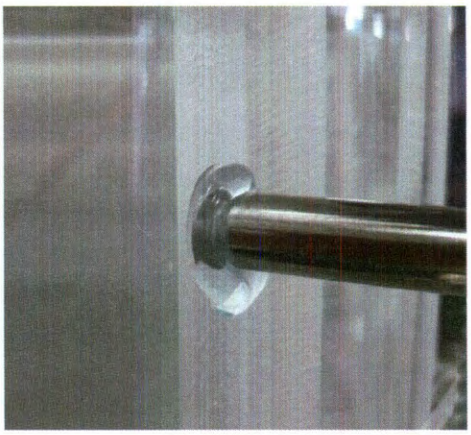

Example of a Correctly Mounted Probe on the Side Bevel

Agitating Beads – Working Fluid Previously Prepared

1. Remove Motor/Lid assembly from the fluid container by lifting vertically.
2. Submerge the stem of the 50 mL syringe in the mixture in the fluid container and draw up the maximum amount of fluid. Try to avoid syringing settled UDV bead material. That is, don't drawn fluid directly from the bottom of the cylinder. Keep the stem submerged for the remainder of the steps.
3. Point the top of the syringe up and expel the fluid back into the container. By pointing the syringe up, you also remove any air that was in the syringe.

Step 3: Proper Agitation Technique

4. Point the syringe down and rapidly draw up as much fluid as possible. By pulling out the syringe rapidly, you lower the pressure in the syringe and

force some of the dissolved air out of the fluid (It is desirable to remove dissolved air from the fluid in the container since this prevents the formation of bubbles on the walls of the fluid container).

5. Place the stem 50 mL syringe toward the bottom of the container and rapidly expel the fluid in the syringe with the end pointed up (again this removes any air that formed in the system from step 4). This will agitate the settled UDV beads at the bottom of the fluid container.
6. Repeat steps 4-5 several times or until the UDV beads look like they have been fully re-suspended in the fluid/UDV bead mixture.
7. Remove the 50 mL syringe from the fluid and draw up as much air as possible. Now with the top of the syringe pointed down, expel the contents of the syringe into the fluid container without submerging the stem. This step removes any of the fluid/UDV bead mixture that was still left in the syringe after step 4-5.
8. Repeat step 7 a few times or until most of the fluid has been removed.
9. If the fluid used is the 20% glycerin/water mixture, take a small beaker and fill it with water. Then draw up the maximum amount of water and expel the water into the sink. Repeat this step 2-3 times so that the syringe gets cleaned. (Do not clean the 50 mL the same way the 10 mL syringe is cleaned. Removing the plunger from the 50 mL syringe will slowly destroy the syringe overtime.)
10. Swing the stem of the syringe in a whipping motion to further remove any fluid that may remain in the stem of the syringe.
11. Dry the outside of the syringe and store.

Motor/Motor Controller Setup

1. Open LabView (also open any network licensed programs that you will need)
2. Connect power from cRIO to motor
3. Connect encoder from cRIO to motor (ensure the arrows are matched)
4. Plug in both power cords from cRIO
5. Disconnect network cable from computer
6. Wait 30 seconds until computer registers the cable disconnect
7. Connect network cable from cRIO to computer
8. Wait 60 seconds until computer registers "limited or no connectivity"
9. Navigate to C:\Houchens Research\Velocity Control with Ramping\Velocity Control (closed loop) – NI 9505.lvproj
10. Open the project file.
11. In the NI Project Explorer interface, expand cRIO1 and open Velocity Control (closed loop) – NI 9505 (RT).vi
12. In the VI set gains to following:

Velocity Loop Parameters		
Proportional Gain: 5.000	Integral Gain: 0.01	Derivative Gain: 1.000
Velocity Loop Rate: 600		Encoder Cycles/ Revolution: 500

Current Loop Parameters		
Proportional Gain: 1.000	Integral Gain: 0.010	Derivative Gain: N/A
Current Loop Rate: 60		Current Limit: 1

Other Parameters		
Drive Direction: Clockwise	Ramping Rate: 2000	Ramping Step: 1

13. Run VI using the play button at the top left corner of the VI window.
14. To change desired velocity edit "Velocity Setpoint". The actual velocity set-point of the system is shown in the bottom right above the stop button. This system has a ramping feature that prevents sudden impulsive changes to the set-point. Whenever the desired set-point differs from the actual set-point, the system will adjust the actual set-point by a size of "Ramp Step" located at bottom center. This adjustment will occur at intervals determined by the "Ramping Rate".

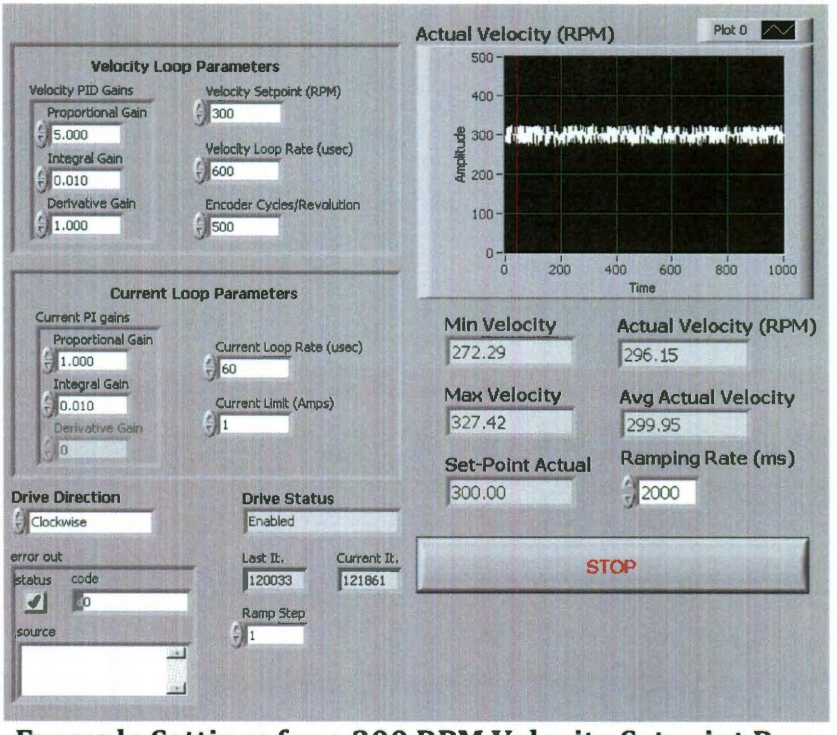

Example Settings for a 300 RPM Velocity Setpoint Run

15. Stop the VI using "Stop" button located at bottom right of the VI.

UDV Setup

1. Connect UDV power cable.
2. Connect UDV USB cable to computer.
3. Connect probe to port 1 (or desired port).
4. Switch the main power switch to the on position.
5. Execute C:\Houchens Research\UDV\Udop.exe
6. Check that "Assisted Mode" is disabled: Preferences → Assisted Mode
7. Go to Parameter → Operating parameters
8. Set the operating parameters as specified in Table 3.1 in body of thesis.
9. Position probe to the desired location.
10. The screen should now show real-time data from UDV.

Appendix C

Converting between Cartesian and Cylindrical velocities in (r, z) plane. All velocities are a function of (x, y).

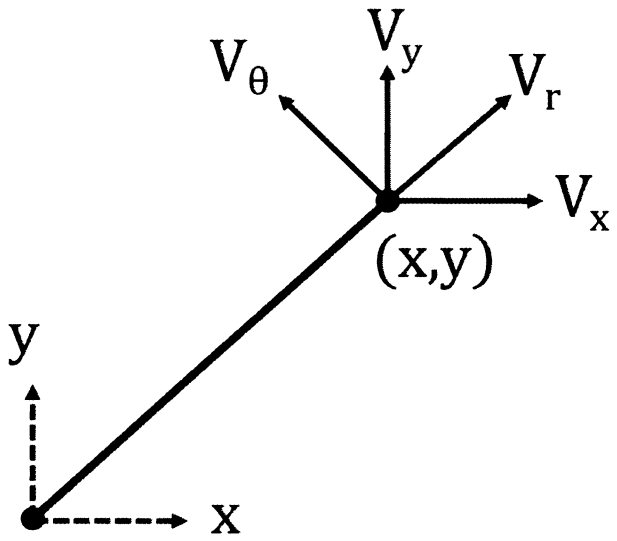

Velocities in Cylindrical to Velocities in Cartesian:

$$V_x = \frac{x}{\sqrt{x^2 + y^2}} V_r - \frac{y}{\sqrt{x^2 + y^2}} V_\theta$$

$$V_y = \frac{y}{\sqrt{x^2 + y^2}} V_r + \frac{x}{\sqrt{x^2 + y^2}} V_\theta$$

Velocities in Cartesian to Velocities in Cylindrical

$$V_r = \frac{x}{\sqrt{x^2 + y^2}} V_x + \frac{y}{\sqrt{x^2 + y^2}} V_y$$

$$V_\theta = \frac{x}{\sqrt{x^2 + y^2}} V_y - \frac{y}{\sqrt{x^2 + y^2}} V_x$$

Appendix D

Table D.1 summarizes the converged runs on the SEMG code. All simulations were run with parameters outlined in Section 3.2.2 for the $\gamma = 2.5$ configuration. The target Reynolds number was $Re = 2500$ for the steady-state runs. However, for most meshes, the code would fail to converge with the steady-state solver at a lower Reynolds number.

In steady-state cases when the SEMG code would fail to converge, the system residual would usually drop a few orders of magnitude in 3-10 Newton Raphson iterations usually using a reasonable number of GMRES iterations. The system residual would then begin to slowly creep back up with each successive Newton Raphson iteration and each of these Newton Raphson iterations would max out on GMRES (the maximum GMRES iterations was set to 1000). Based on this behavior, it was believed that the convergence issue was caused by insufficient mesh resolution. However, increasing the mesh resolution did not seem to solve the problem. When the system residual was visualized, the maximum value usually occurred at the edge between the rotating lid and the wall of the cylinder as expected. However, there were also cases where the maximum system residual occurred at core of the cylinder ($r = 0$) suggesting that there may be in issue with how the singularity at $r = 0$ is handled by the SEMG code.

Mesh	Reynolds Number	System Tolerance
$12 \times 20 \times 12$	1500	10^{-7}
	2000	10^{-7}
	2500	10^{-7}
$15 \times 20 \times 15$	1000	10^{-8}
	1500	10^{-8}
	2000	10^{-8}
$8 \times 12 \times 20$	1000	10^{-8}
	1500	10^{-8}
	2000	10^{-8}
$12 \times 10 \times 30$	1000	10^{-8}
	1500	10^{-8}
	2000	10^{-8}
$10 \times 10 \times 25$	1000	10^{-8}
	1500	10^{-8}
	2000	10^{-8}
$12 \times 10 \times 25$	500	10^{-8}

Table D.1 – Summary of converged runs for SEMG spectral element CFD code

Figure D.1 to Figure D.4 compare the numerical results from the SEMG runs to SEMTEX results. The axial velocity along the diameter of the cylinder at $h = 1.25$ is plotted at different Reynolds numbers. The plots show that the converged results from SEMG are quantitatively similar to SEMTEX results. The results at $Re = 1000$ are almost identical but there is some divergence at higher Reynolds numbers.

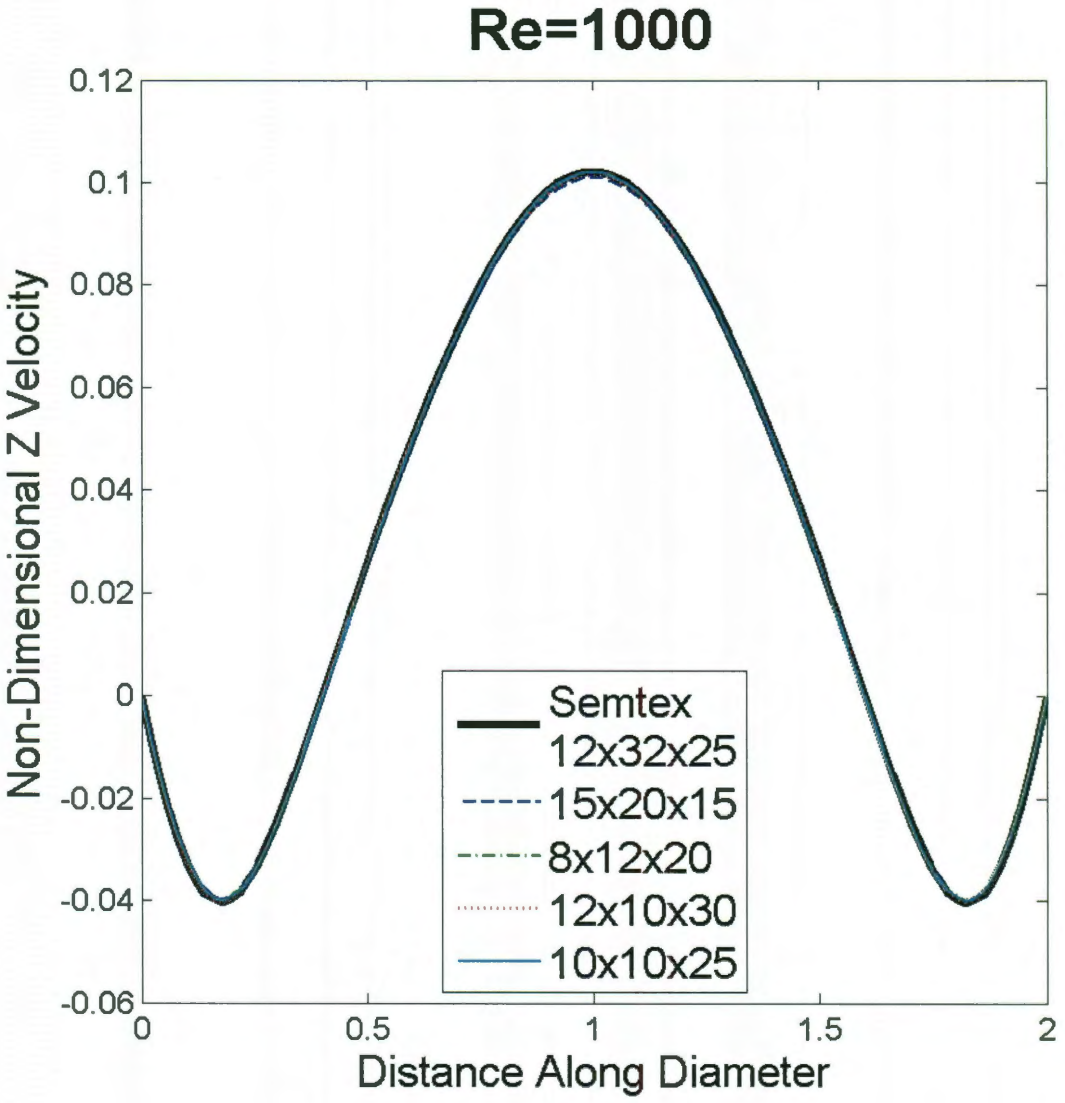

Figure D.1 – Comparision between SEMG and SEMTEX results $Re = 1000$

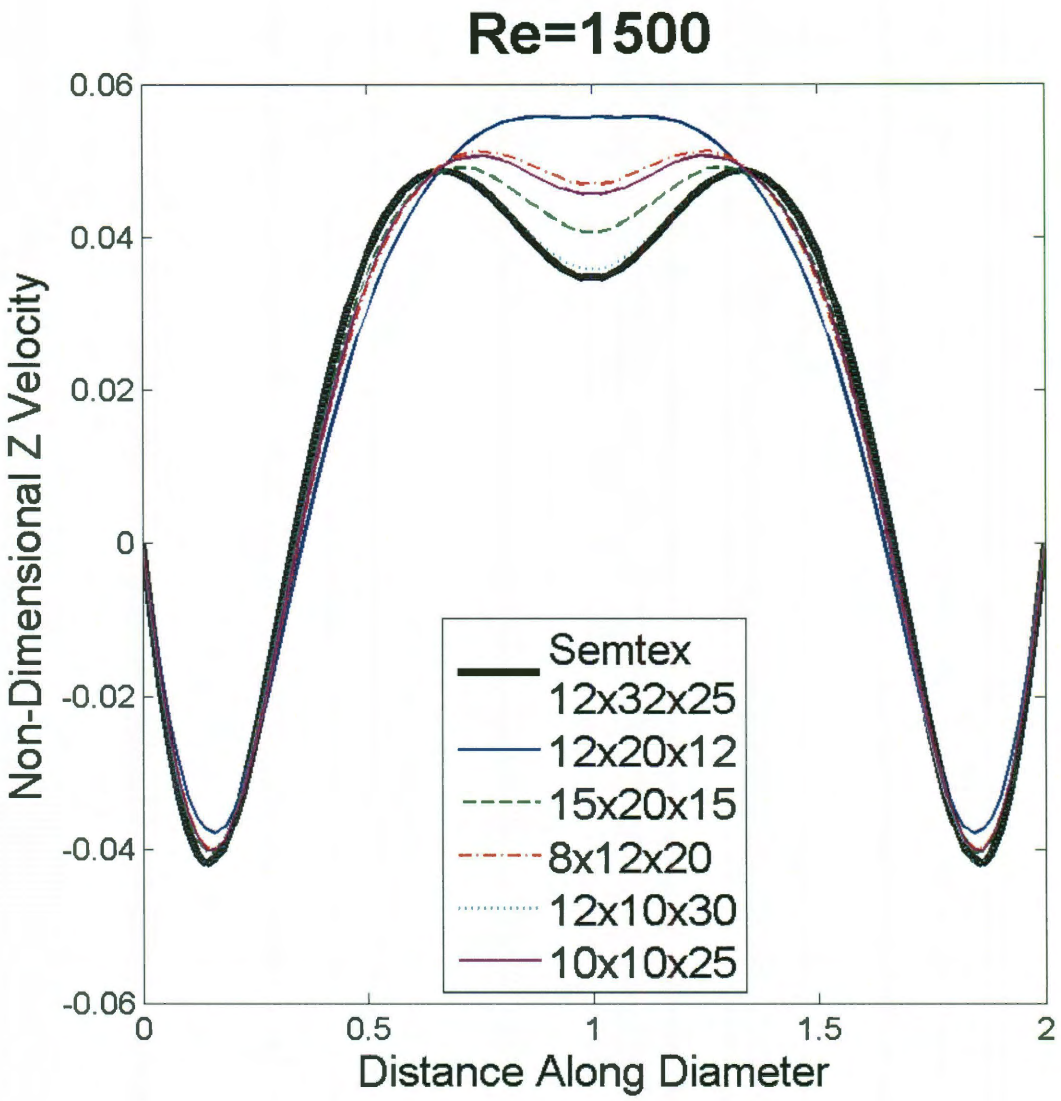

Figure D.2 – Comparision between SEMG and SEMTEX results $Re = 1500$

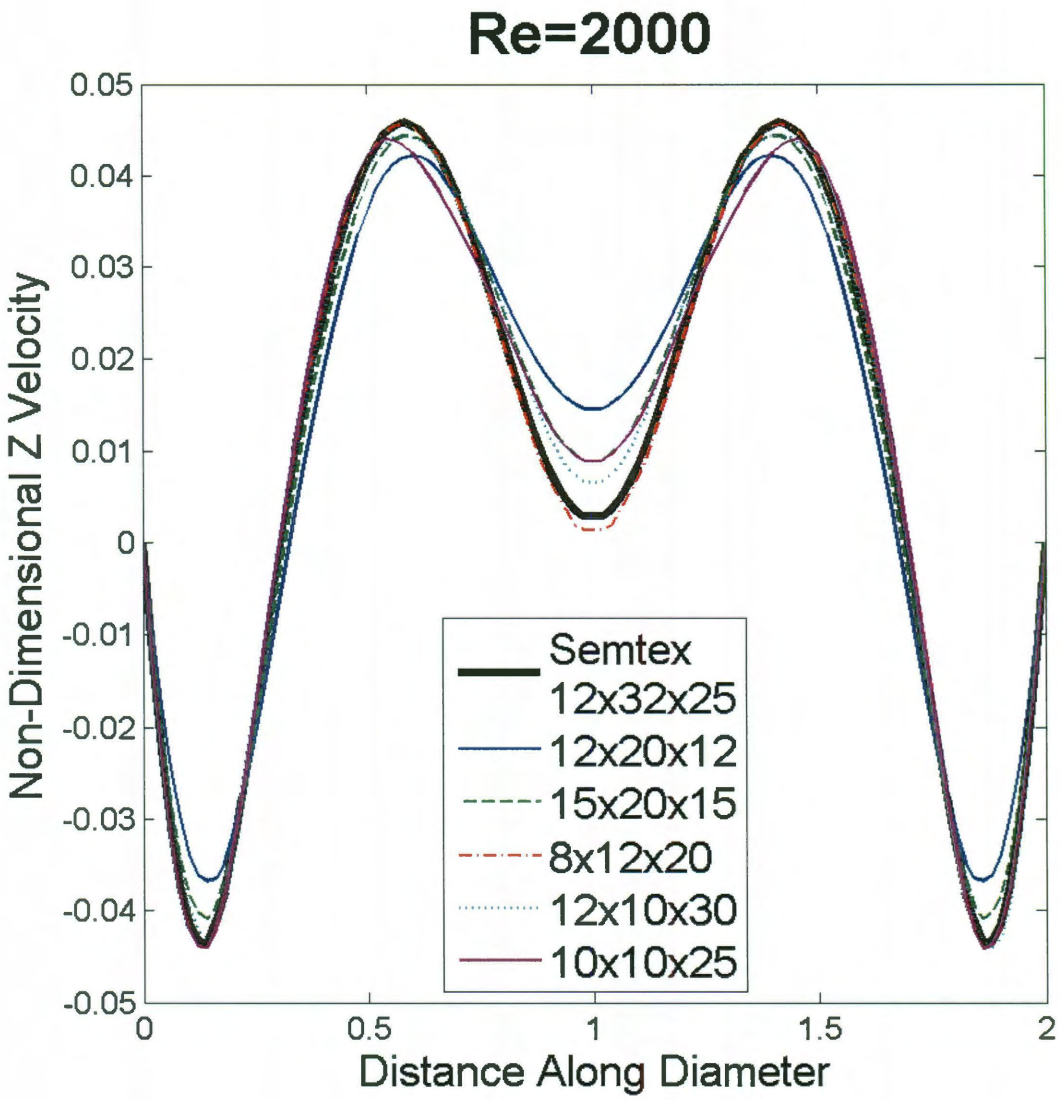

Figure D.3 – Comparision between SEMG and SEMTEX results $Re = 2000$

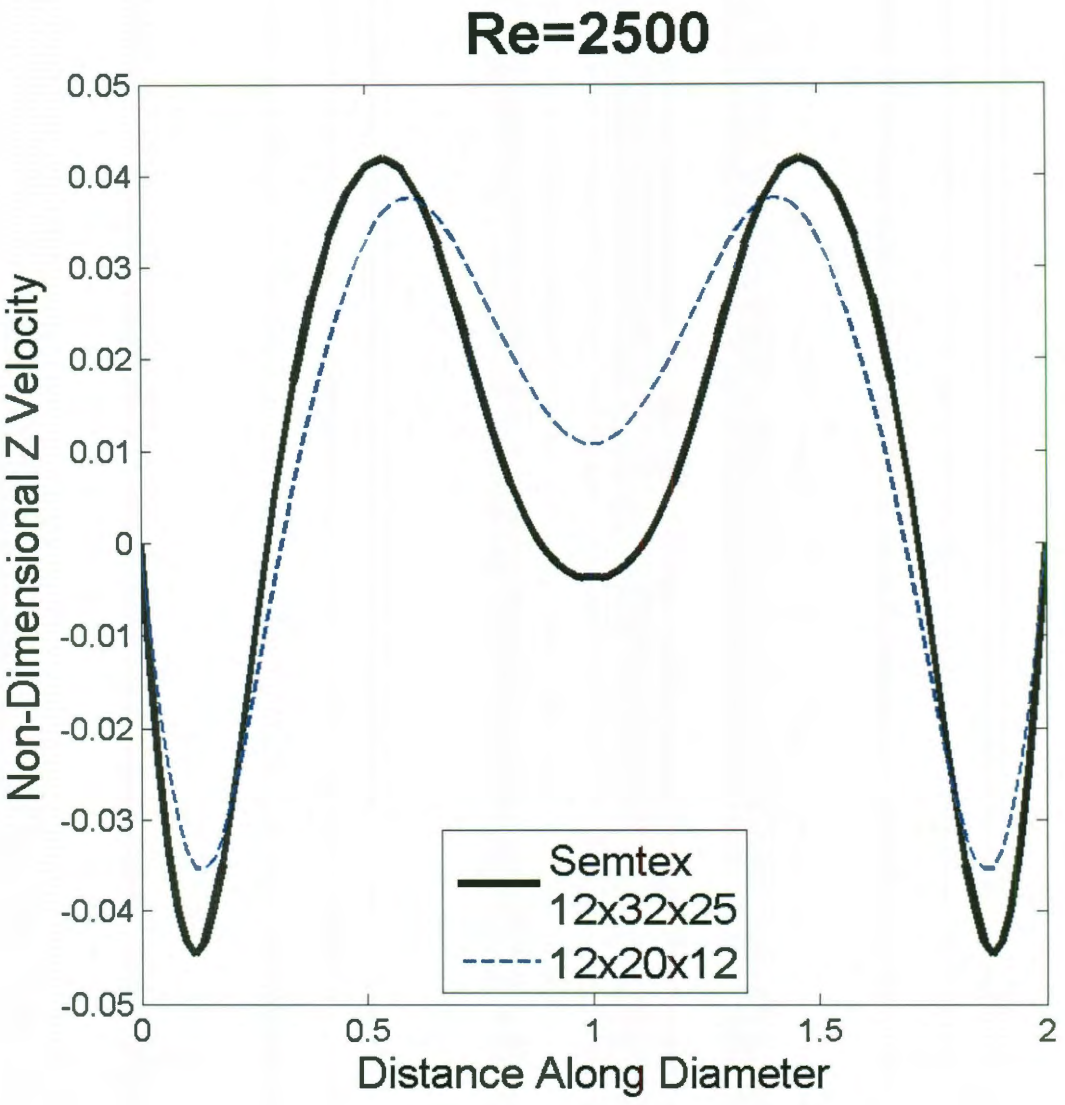

Figure D.4 – Comparision between SEMG and SEMTEX results $Re = 2500$